NORWEGIAN UNIVERSITY OF SCIENCE AND TECHNOLOGY

Direct Numerical Simulation of the Flow Past a Curved Circular Cylinder

by

José P. Gallardo Canabes

A thesis submitted in partial fulfillment for the
degree of Master of Science in Marine Technology

in the

Faculty of Engineering Science and Technology
Department of Marine Technology

August 2010

Preface

This document titled 'Direct Numerical Simulation of the Flow Past a Curved Circular Cylinder' and the work presented in it are the Master thesis of José P. Gallardo Canabes, prepared in the Fall of 2010, as the final part of his Master of Science in Marine Technology degree from the Norwegian University of Science and Technology. In this work, the results obtained from the numerical simulations of the flow past a curved cylinder are presented and discussed. The motivation to carry out these simulations was the understanding of the dynamics of the flow past marine structures with catenary shape. The first set of simulations was intended to be used for comparison with previous published studies. The second set of simulations was conducted in order to investigate the influence of shear flow in the dynamics of the flow past the curved cylinder.

According to the objectives exposed above, the present Master thesis is developed in the following chapters:

Chapter 1. Introduction. Presents some relevant topics from previous studies, giving thus a theoretical basis for the development of this work.

Chapter 2. Numerical Solution of the Navier-Stokes Equations. Contains a summary of the relevant issues associated to the numerical solution of the Navier-Stokes equations.

Chapter 3. Flow Configuration and Simulation Tests. The boundary conditions and computational domain are discussed here.

Chapter 4. Results and Discussion: Uniform Flow. Presentation and discussion of the results obtained with uniform flow.

Chapter 5. Results and Discussion: Shear Flow. Presentation and discussion of the results obtained with shear flow.

Chapter 6. Conclusions. A summary and discussion of the main findings.

NORWEGIAN UNIVERSITY OF SCIENCE AND TECHNOLOGY

Abstract

Faculty of Engineering Science and Technology
Department of Marine Technology

Master of Science degree in Marine Technology

by José P. Gallardo Canabes

Offshore marine applications often include configurations of cylindrical structures that produce complex three-dimensional flow features. Catenary risers, for instance, can create complex flow patterns when subjected to hydrodynamic loads. In recent published studies, the shape of a catenary riser has been approximated by a quarter segment of a ring followed by a horizontal extension, obtaining a *curved circular cylinder*. In the present Master thesis, Direct Numerical Simulations at $Re = 100$ and 500 have been conducted in order to study the flow past such geometry. The main flow direction was parallel to the plane of curvature of the cylinder and directed towards the convex face of the quarter-of-ring. Additionally, a sheared incoming flow has been considered in the analysis by imposing a linearly varying velocity profile at the inlet.

The shedding mechanism observed in uniform flow was similar to that reported in previous published studies. One single shedding frequency prevailed along the entire span of the cylinder at $Re = 100$ and 500. Moreover, the vortex cores at $Re = 100$ were normal to the flow direction and exhibited slight distortions as they were convected downstream, whereas at $Re = 500$ the wake topology was characterized by three-dimensional structures of smaller scale. A sheared inflow, on the other hand, gave rise to an oblique and cellular vortex shedding pattern with two cells of different shedding frequencies. The strong slanting of the vortices, as well as the cellular pattern, was clearly induced by the variation of the local Reynolds number along the front stagnation point.

The basic knowledge gained from this thesis appear as very promising in the context of marine structures, it is therefore expected that this work will constitute a basis for further investigations considering this type of geometry.

Acknowledgements

In the first place I would like to express my gratitude to my supervisor, Professor Bjørnar Pettersen, who gave me encouragement, guidance and support from the moment I started to work in this exciting topic. I am very thankful to Professor Helge I. Andersson for his inspiring comments and support during the development of this thesis, and for his excellent lectures in turbulence. Special thanks also to PhD candidate George K. El Khoury, for having introduced me to the code MGLET, and for helping me out during the different stages of this work.

The simulations presented in this work would not have been possible without parallel computing. I am therefore very grateful to the Norwegian HPC project NOTUR, that granted access to its computer facilities.

Last but not the least, I would like to express my deepest gratitude to Karin, for accompanying me and having understood the meaning of the Reynolds number, and to my family in Chile, for their constant love and support despite being 13 000 kilometers from Trondheim.

Contents

Preface i

Abstract ii

Acknowledgements iii

List of Figures vi

List of Tables viii

Abbreviations ix

Symbols x

1 Introduction 1
- 1.1 Flow past circular cylinders . . . 2
- 1.2 Flow past yawed circular cylinders . . . 5
- 1.3 Flow past curved circular cylinders . . . 9
- 1.4 Effects of uniform shear as an inflow boundary condition . . . 11
- 1.5 Motivation . . . 14

2 Numerical Solution of the Navier-Stokes Equations 16
- 2.1 Governing equations of flow . . . 16
- 2.2 The Navier-Stokes solver MGLET . . . 17
  - 2.2.1 Finite volume discretization . . . 17
  - 2.2.2 Temporal discretization and solution of the Poisson equation . . . 18
  - 2.2.3 Parallelization . . . 19
- 2.3 The Immersed Boundary Method . . . 20

3 Flow Configuration and Simulation Tests 22
- 3.1 Problem definition . . . 22
- 3.2 Simulation parameters and implementation . . . 23
- 3.3 Influence of the domain size . . . 26

4 Results and Discussion: Uniform Flow 30
- 4.1 $Re = 100$ . . . 31
  - 4.1.1 Stagnation pressures and recirculation region at $Re = 100$ . . . 31

4.1.2 Frequency analysis at $Re = 100$ . . . 34
4.1.3 Wake topology at $Re = 100$ . . . 36
4.2 $Re = 500$ . . . 39
4.2.1 Near wake flow at $Re = 500$ . . . 40
4.2.2 Frequency analysis at $Re = 500$ . . . 43
4.2.3 Wake topology at $Re = 500$ . . . 44
4.3 Effects of a larger radius of curvature at $Re = 100$ . . . 47

5 Results and Discussion: Shear Flow **50**
5.1 Effects of the shear flow in the near wake . . . 51
5.2 Cellular vortex shedding . . . 55
5.3 Influence of the shear rate on the wake topology . . . 58

6 Conclusions **63**

A Paper Presented at the ETMM8 Conference **66**

B Paper Presented at the ECCOMAS CFD 2010 Conference **73**

C Visualizations **90**

Bibliography **92**

List of Figures

1.1 Wake pattern in the steady regime. . . . 3
1.2 Wake pattern in the unsteady regime. . . . 3
1.3 Schematic view of the flow past a yawed cylinder. . . . 6

2.1 Control volumes in the staggered grid. . . . 18
2.2 One-dimensional stencil for the interpolation using the IBM method . . . 20

3.1 Computational domain size, geometry and flow configuration. . . . 23
3.2 Detail of the $400 \times 150 \times 258$ Cartesian mesh around the curved cylinder 24
3.3 View of the blocking of cells in the Cartesian mesh by the IBM method. . 26
3.4 Perspective view of the vortex cores at $Re = 100$ to analyze the effect of adding a vertical extension. . . . 29

4.1 Location of the middle (x, z)-plane for the analysis of results. . . . 31
4.2 Mean pressure coefficients C_p along the span of the curved cylinder at $Re = 100$. . . . 32
4.3 Mean pressure coefficients normalized by U_n at $Re = 100$. . . . 33
4.4 Streamlines of the mean flow taken at the middle (x, z)-plane at $Re = 100$. 33
4.5 Recirculation length L_s along the span of the curved cylinder at $Re = 100$. 34
4.6 Time evolution and time trace of v–velocity at $Re = 100$. . . . 35
4.7 Power spectra of the v-velocity signal at $Re = 100$. . . . 36
4.8 Vortex cores depicted as instantaneous iso–surfaces of λ_2 at $Re = 100$. . . 37
4.9 Isosurfaces of instantaneous vorticity ω_x and ω_z at $Re = 100$. . . . 38
4.10 Isocontours of instantaneous streamwise and vertical vorticity at $Re = 100$. 39
4.11 Mean pressure coefficients C_p along the span of the curved cylinder at $Re = 500$. . . . 41
4.12 Streamlines of the mean flow taken at the middle (x, z)–plane at $Re = 500$. 41
4.13 Instantaneous streamlines at $Re = 500$ close to the recirculation region. . 42
4.14 Recirculation length L_s along the span of the curved cylinder at $Re = 500$. 42
4.15 Time evolution and time trace of v–velocity at $Re = 500$ . . . 43
4.16 Power spectra of the v-velocity signal at $Re = 500$. . . . 44
4.17 Vortex cores depicted as instantaneous iso–surfaces of λ_2 at $Re = 500$. . . 45
4.18 Isosurfaces of instantaneous vorticity ω_x and ω_z at $Re = 500$. . . . 46
4.19 Isocontours of instantaneous streamwise and vertical vorticity at $Re = 500$. 46
4.20 Computational domain size, geometry and flow configuration at $R/D = 25$. 47
4.21 Power spectra of the v-velocity signal at $Re = 100$ and $R/D = 25$. . . . 49
4.22 Vortex cores depicted as instantaneous iso–surfaces of λ_2 at $R = 100$ and $R/D = 25$. . . . 49

5.1 Flow configuration considering shear flow at the inlet. 51
5.2 Mean pressure coefficients C_p along the span of the curved cylinder at $Re = 100$ and 500 in uniform shear. 52
5.3 Streamlines of the mean flow taken at the middle (x, z)-plane at $Re = 100$ and 500 in uniform shear. 53
5.4 Instantaneous streamlines at $Re = 100$ and 500, and $K = 0.1$; close view of the recirculation region. 54
5.5 Recirculation length L_s along the span of the curved cylinder at $Re = 100$ and 500 in uniform shear. 55
5.6 Time evolution and time traces of v–velocity at $Re = 100$ and 500 in uniform shear. 57
5.7 Power spectra of the v-velocity signals at $Re = 100$ and 500 in uniform shear. 58
5.8 Strouhal frequencies versus local Reynolds numbers, uniform shear at $Re = 100$ and 500. 59
5.9 Vortex cores depicted as instantaneous iso–surfaces of λ_2 at $Re = 100$ and 500 in uniform shear. 60
5.10 Isocontours of instantaneous streamwise and vertical vorticity at $Re = 100$ in uniform shear. 61
5.11 Isocontours of instantaneous streamwise and vertical vorticity at $Re = 500$ in uniform shear. 62

List of Tables

3.1 Parameters of the different computational domains. 27

Abbreviations

DNS	**D**irect **N**umerical **S**imulation
FFT	**F**ast **F**ourier **T**ransform
HPC	**H**igh **P**erformace **C**omputing
IBM	**I**mmersed **B**oundary **M**ethod
IP	**I**ndependence **P**rinciple
MPI	**M**essage **P**assing **I**nterface
rms	**r**oot **m**ean **s**quare
SIP	**S**trongly **I**mplicit **P**rocedure
SOR	**S**uccessive **O**ver **R**elaxation
VIV	**V**ortex **I**nduced **V**ibration

Symbols

C_p	Pressure coefficient	-
C_pn	Pressure coefficient normalized by U_n	-
D	cylinder diameter	m
f	frequency of vortex shedding	Hz (s^{-1})
K	non-dimensional shear rate	-
L_s	local separation length	m
L_x, L_y, L_z	domain size in the x-, y- and z-directions	-
n_{px}, n_{py}	number of processors in the x-, y-directions	-
N_x, N_y, N_z	grid points in the x-, y- and z-directions	-
$\tilde{p}$	pressure	Pa
p	non-dimensional pressure	-
p_∞	non-dimensional pressure at the inlet	-
R	radius of curvature	m
Re	Reynolds number	-
Re_l	local normal Reynolds based on $U_\infty(z)$	-
Re_n	local normal Reynolds based on U_n	-
Ro	Roshko number	-
Ro_n	local Roshko number based on U_n	-
s	span of the curved cylinder	m
S_{ij}	symmetric component of the velocity gradient tensor	-
St	Strouhal number	-
$\tilde{\boldsymbol{u}}$	velocity vector	ms^{-1}
$\boldsymbol{u}$	non-dimensional velocity vector	-
$\tilde{u}$ $\tilde{v}$, $\tilde{w}$	velocity components	ms^{-1}
u, v, w	non-dimensional velocity components	-

U_0	inflow velocity at the bottom plane	ms^{-1}
U_c	inflow velocity at the mid height of the domain	ms^{-1}
U_∞	inflow velocity	ms^{-1}
U_n	normal component of inflow velocity	ms^{-1}
U_t	tangential component of inflow velocity	ms^{-1}
X_i	distance between inflow plane and body	m
Y_h	half-width of the domain	m
Z_u	vertical extension of curved cylinder	m
α	yaw angle	rads
δ	boundary layer thickness	m
Δx Δy, Δz	grid spacing along the x-, y- and z-directions	m
ϵ	energy dissipation rate	$\mathrm{m}^2\mathrm{s}^{-3}$
η	Kolmogorov length scale	m
θ	angle measure from the top plane	rad
λ_2	second largest eigenvalue of the symmetric tensor $\Omega_{ij}\Omega_{ij} + S_{ij}S_{ij}$	-
ν	kinematic viscosity	$\mathrm{m}^2\mathrm{s}^{-1}$
ρ	density	kgm^{-3}
$\boldsymbol{\omega}$	vorticity vector	s^{-1}
ω_x,ω_y,ω_z	vorticity components	s^{-1}
Ω_{ij}	antisymmetric component of the velocity gradient tensor	-

Chapter 1

Introduction

Flow over bluff bodies, in association with the flow over an obstacle or the movement of a body, are commonly encountered in nature and engineering applications. Typical examples within the context of marine applications are the flows past a fishing net, a submarine, a ship, the legs of an oil platform, and a riser. The three-dimensional complexity that these flows possess makes them a significant topic of research by means of experiments and numerical simulations, being perhaps the flow past a circular cylinder the bluff-body configuration that have received most of the attention during the 20^{th} century (see for instance the work by Zdravkovich, 1997). In many cases, however, cylindrical geometries are non-uniform, introducing further complexities into the flow features that are interesting to study.

In order to highlight some relevant topics for the development of this thesis, this chapter presents a brief description of the dynamics of the flow past three types of bluff-body geometries: straight circular cylinders, yawed circular cylinders and curved circular cylinders. In this case, yawed cylinders have been included to link the flow past straight cylinders with the flow past curved cylinders. In section 1.4, the effects of having shear flow in the free-stream is discussed . Finally, the motivation to carry out this work is presented in section 1.5.

1.1 Flow past circular cylinders

One of the most popular problems in fluid mechanics is the flow around a uniform circular cylinder. The fact that there is a huge amount of available literature on this subject is not surprising, since flow past cylinders has been a topic of theoretical, experimental and numerical research for many years. In the extensive review made by Zdravkovich (1997), three main components of the flow past a circular cylinder (and past a bluff body in general) are mentioned: the *boundary layer*, the *separated shear layers* and the *wake* (see figures 1.1 and 1.2). In the absence of surface roughness and blockage effects, these interacting components undergo a transition process towards turbulence that depends on only one parameter of the flow, namely the *Reynolds number*, Re, which is defined as

$$Re = \frac{U_\infty D}{\nu}, \tag{1.1}$$

with U_∞ the characteristic velocity of the incoming flow, D the cylinder diameter and ν the kinematic viscosity of the fluid. Some stages of this transition process as Re increases are summarized in this section.

At very low Reynolds numbers, i.e. $Re < 4$–5, the boundary layers are completely attached to the cylinder walls, this steady regime is known as *creeping flow*. At 4–$5 < Re < 30$–49 a *steady separation regime* develops in which the boundary layers separate and are transported downstream as two free shear layers and eventually reattach along the wake centerline, thus forming a *recirculation region* composed of two steady, symmetric, and closed vortices that adhere to the cylinder (see figure 1.1). It has been observed that the maximum length of the wake (recirculation region) increases linearly with increasing Reynolds number due to viscous stresses (see Coutanceau and Bouard, 2006), whereas the base pressure coefficient decreases (Henderson, 1995). In this context, the base pressure corresponds to the pressure measured at the rear stagnation point of the cylinder, i.e. the point located at 180° from the leading edge of the cylinder.

When the Reynolds number is increased beyond 49, a transition from the steady state to an unsteady state occurs, giving raise to the *laminar vortex shedding* regime (in the range $49 < Re < 190$). A characteristic flow feature in this regime is the *Kármán-Bénard eddy street*, which consits of a staggered array of vortices that are shed periodically from

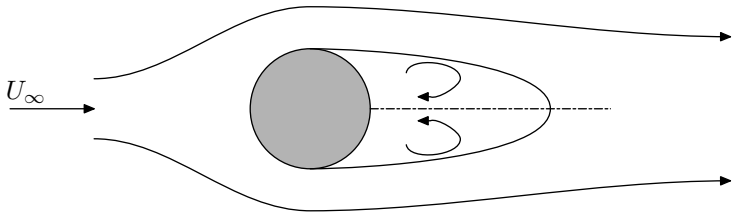

FIGURE 1.1: Wake pattern in the steady regime, depicting the pair of symmetric recirculating vortices.

alternates sides of the body, as seen in figure 1.2. The departure from the steady state is marked by instabilities that start developing at the downstream end of the recirculation bubble; these instabilities gradually grow in strength and amplification with Re. The behaviour of this instability near the transition threshold, i.e. $Re \approx 49$, was investigated by Provansal et al. (1987); the separated near-wake undergoes a Hopf bifurcation, and the flow can be represented as a dynamical system with its behaviour described by a Stuart-Landau equation. Williamson (1996a) proposed that this transition process can be measured in terms of amplitude of maximum wake velocity fluctuations, which increase monotonically with Re, and a gradual displacement upstream towards the cylinder of the instability formation length. Various formulations have been proposed for the relationship between the Strouhal number ($St = fD/U_\infty$, where f is the frequency of the vortex shedding) and Re. The work of Williamson (1998), for instance, proposed a relationship between St and Re based on an expansion in powers of $1/\sqrt{Re}$. Although the upper limit for the laminar vortex shedding regime in terms of Reynolds number is rather spread in the literature, with $Re = 140$ up to 194 Williamson (1996b), experimental and numerical results obtained in the last decade suggest that the critical Reynolds number is placed around 190 (Barkley and Henderson, 1996, Miller and Williamson, 1994, Persillon and Braza, 1998). At this point a second transition takes place.

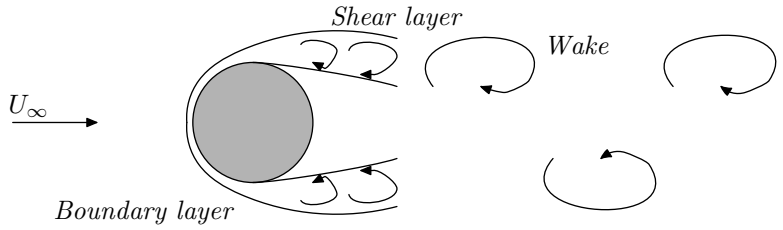

FIGURE 1.2: Wake pattern in the unsteady regime, depicting the vortex eddy street.

The *wake-transition regime* occurs at $Re \approx 190$ to 260, here the flow becomes intrinsically three-dimensional and two marked discontinuities in the St-Re relationship arise as

a distinguishing feature. The first of these discontinuities, identified as 'mode A' instability by Williamson (1996a), takes place near $Re = 180$–190 and involves the formation of vortex loops and streamwise vortex pairs due to the deformation of the primary vortices; the spanwise wavelength of these instabilities may vary between 3 and 4 diameters. This transition is identified as a drop in the Strouhal frequency from the laminar *St*-*Re* curve, and is known to be hysteric, i.e. the exhibited critical *Re* value for the transition will be different depending on whether the free-stream speed is increased or decreased. A further increase of the Reynolds number to the range $Re = 230$–260 yields the second discontinuity ('mode B') in the *St*-*Re* relationship. This mode is characterized by streamwise vortices of finer-scale with a spanwise wavelength close to one diameter. Williamson (1992) showed for this transition regime the formation of large-scale spot-like "vortex dislocations" between spanwise cells of different frequency, explaining thus the presence of large intermittent low-frequency wake velocity fluctuations found in previous studies. In contrast to 'mode A', the 'mode B' discontinuity depends on the reverse flow of the bluff-body wake, and is responsible for the break-up to turbulence of the wake as it is transported downstream. The *wake-transition regime* has also been analyzed by means of numerical simulations, obtaining good agreement with the experimental studies (Barkley and Henderson, 1996, Karniadakis and Triantafyllou, 1992, Persillon and Braza, 1998).

Around $Re = 260$ the base pressure attains a peak which, according to Williamson (1996a), is associated with a peak in the Reynolds stresses and a particularly regular arrangement of the fine-scale streamwise vortices in the near wake. Although fine-scale streamwise vortices are present, the wake behaves much like the laminar vortex shedding regime up to this *Re*. A further increase of the Reynolds number leads to increasing disorder in the fine-scale three-dimensional structures, resulting in an apparent reduction in the two-dimensional Reynolds stresses, a marked reduction in the base pressure, and an increasing *vortex formation length*, which is defined as the distance downstream from the cylinder axis to the point where the root mean square (rms) velocity fluctuations are maximized on the wake center line. Using Direct Numerical Simulation (DNS), Karniadakis and Triantafyllou (1992) investigated the transition to turbulence in the wake of a circular cylinder (*Re* beyond 260), reporting a chaotic state in the flow at *Re* around 500 resulting from a cascade of period-doubling bifurcations; they concluded that the *transition to turbulence in the wake* follows this period-doubling route.

In the range of Reynolds numbers greater than 260 at which the wake becomes turbulent, the transition point moves upstream and instabilities in the shear layer arise; this phenomenon marks the beginning of the *shear layer transition regime* ($Re = 1 \times 10^3$ to 2×10^5). In connection with transition, Bloor (1968) observed regular sinusoidal waves within the region of vortex formation at $Re > 1300$. The frequency of these waves was found to be roughly proportional to $Re^{3/2}$, suggesting that they may be identified with Tollmien-Schlichting waves. Moreover, a decrease in the length of the formation region beyond $Re = 1300$ was reported by Bloor (1968). A Kelvin-Helmholtz that develops from the instability of the shear layers, which is basically a two-dimensional phenomenon, contributes to the increase in the two-dimensional Reynolds stresses and thereby to the rise in base suction. The developing instabilities of the separating shear layers from the sides of the cylinder are also known to induce a gradual decrease in Strouhal frequency associated with the increase in the base suction (Norberg, 1994). A development of three-dimensional structures on the scale of the shear layer vortices, as well as three-dimensionality on the scale of the primary vortices, are expected in this regime (Williamson, 1996b). The boundary layer in this regime still remains laminar.

Since flows at Reynolds numbers beyond the shear layer transition range are out of the scope of the present work, they will not be described here. For further reading, please refer to the comprehensive reviews by Roshko (1993), Williamson (1996b) and Zdravkovich (1997).

1.2 Flow past yawed circular cylinders

The description given in the previous section applies for cylinders with their axes perpendicular to the free-stream direction. In many engineering applications, however, circular cylinders are positioned at a certain *yaw angle* α, which is defined as that between the cylinder axis and the normal to the free-stream velocity. A typical flow configuration of the flow past a yawed cylinder is shown in figure 1.3. The response of a yawed cylinder in terms of vortex shedding frequency, base pressure and hydrodynamic forces may differ from the normal incidence case. According to Zdravkovich (2003), the following features are associated to flow past yawed cylinders:

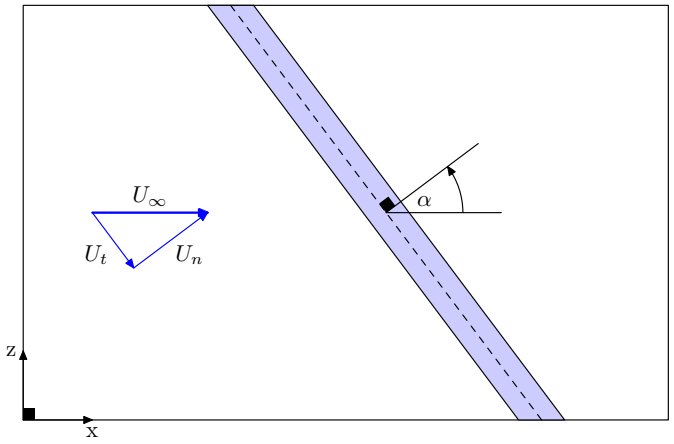

FIGURE 1.3: Schematic view of the flow past a yawed cylinder. Here α is the yaw angle and U_∞ is the inflow velocity, which is decomposed in its normal U_n and tangential U_t components. For the configuration shown here, $\alpha = 0°$ corresponds to cross flow and $\alpha = 90°$ corresponds to axial flow.

i. The cross-section of a yawed circular cylinder becomes elliptical, being the ratio of the major-to-minor axis of the ellipse proportional to the yaw angle.
ii. The free stream velocity has two components, one normal to the cylinder axis $U_n = U_\infty \cos\alpha$, and the other parallel to the cylinder axis $U_t = U_\infty \sin\alpha$. From this two, it has been argued that U_n has a larger effect on the flow.

A common approach to modelling the hydrodynamics of the flow past yawed cylinders is to use the *Independence Principle* (IP), also known as the *Cosine Law*. In this formulation the projected flow in the normal plane, based on the component of the free-stream velocity normal to the cylinder axis U_n, is similar to the normal incidence case. Zdravkovich (2003) mentions the following limitations of the IP:

i. Originally the IP was derived from the laminar boundary layer theory, which becomes invalid beyond separation.
ii. As the flow past yawed cylinders is subjected to end effects, the mathematical idealization of two-dimensional flow past cylinders of infinite aspect ratio cannot be realized in practice. This is especially relevant for experimental studies.
iii. The transition around separation for unyawed cylinders occurs at a certain Reynolds number due to instability of the boundary layers. It may be expected that the instability would occur at the same Re for a yawed cylinder, but the spanwise flow is likely to modify the disturbances and the Re value at which separation occurs.

Early attempts to experimentally verify the IP in the laminar regime were done by Hanson (1966). He measured the frequency of the wake trail oscillations, and subsequently the eddy shedding in the range $40 \leq Re \leq 150$ for the yaw angles $0° \leq \alpha \leq 72°$. It was reported that α has an effect upon the onset of the laminar vortex shedding regime Re_{osc}, based on the free stream velocity. Hanson noted that Re_{osc} rises with increasing α. However, when using the local Reynolds number $Re_n = U_n D/\nu$, the critical Reynolds number at which vortex shedding initiates was constant up to $\alpha = 50°$.

Hanson (1966) also studied vortex shedding for low Reynolds number from vibrating yawed hot wires in an air stream. Using the Roshko's number ($Ro = fD^2/\nu$), Hanson obtained different straight lines of Ro vs. Re for various values of α in the low Reynolds number range 40–150. Scaling this data by Re_n gave evidence that the following linear relationship derived for uniform cylinders could be extended for yawed cylinders

$$Ro_n = 0.212 Re_n - 4.5, \qquad \text{for } \alpha \leq 50°. \tag{1.2}$$

For $\alpha = 72°$, however, Hanson (1966) noted that the shedding frequencies values (or values of Ro) departed from equation (1.2).

In an attempt to explain the apparent discontinuity reported by Hanson (1966) for α in the range $50° \leq \alpha \leq 75°$, Van Atta (1968) carried out careful measurements of the vortex shedding frequency. For constant Re_n, he reported a steady decrease of St as the yaw angle α increases. He concluded that the discontinuity observed by Hanson was not due to the large α, but to the existence of locked-in modes depending on the value of the wire tension. He also reported that for a given tension, the wire does not necessarily vibrate with the frequency of the harmonic that is nearest to the natural shedding frequency, but always locks-in to the frequency that is lower than the natural shedding frequency. In the case of non-vibrating yawed cylinders, Van Atta (1968) showed that for $\alpha \leq 35°$ the vortex shedding frequency decreases nearly like the IP, whereas for larger angles the decrease with increasing angle of yaw α is slower than the proposed IP.

Ramberg (1983) studied the effect of yaw angle ($\alpha = 0$–$60°$) and end-conditions for stationary and forced vibrating circular cylinders (with aspect ratio 20–100) in the Reynolds number range 150–1000. He found that the results were very sensitive to end-conditions especially at the lower Reynolds numbers, showing that slantwise shedding at angles

other than the cylinder yaw angle is intrinsic to stationary inclined cylinders in the absence of end-effects. Ramberg (1983) suggested that the IP fails in the case of stationary yawed cylinders because the shedding frequency is always greater than that expected from the IP, while the shedding angle, the vortex-formation length, the base pressure and the wake width are all less than expected. Nevertheless, he concluded that locked-in vortex wakes of vibrating yawed cylinders can be described successfully by the IP. In this case, frequency lock-in between the vortex wake and the cylinder motion was accompanied by vortex shedding parallel to the cylinder axis.

A numerical study using DNS at $Re = 1000$ and a yaw angle range 0-60° was conducted by Zhao et al. (2009), showing that the Strouhal frequency at various yaw angles followed the Independence Principle. In this case, the use of DNS allowed for better visualization of additional flow features in the streamlines and the vortical structures. The streamlines approached the leading edge of the cylinder with an increasing bending and sliding along the cylinder, followed by a deflection in the main flow direction. After passing the cylinder, a fraction of the streamlines are retained inside the recirculation region and move in the spanwise direction of the cylinder in helical tracks, while others move in the free stream direction. Once the primary vortex is shed from the cylinder surface, the trapped streamlines are released and their directions change back to the incoming flow direction. The spanwise vortices in this study were identified as isosurfaces of spanwise vorticity ω_z. At $\alpha = 45°$ the spanwise vortices were shed parallel to the cylinder axis, whereas at $\alpha = 60°$ the shedding angle was less defined. This was in good agreement with a previous study by Lucor and Karniadakis (2003), in which they observed that the spanwise wake vortices are oriented at a smaller angle than the yaw angle of the cylinder for $\alpha > 45°$. Zhao et al. (2009) also noticed that the mean pressure coefficient C_p along the surface of the cylinder decreases with increasing α, reducing the difference in pressure between the front and rear stagnation lines as well. The validity of the IP was obtained by normalizing the pressures coefficients by U_n, in this case the pressure coefficient curves for different α's collapsed into a single curve. The frequency spectra were obtained for different values of α, no variation in the peak locations with α was detected. Moreover, the peak region for $\alpha = 60°$ was broader than that for the unyawed cylinder, indicating that with the increase of the yaw angle, the rate of the breakdown of the vortical structures is increased.

Using a phase averaged technique, Zhou et al. (2010) investigated the dependence of the wake vortical structures on cylinder yaw angle 0–45°. All three-velocity and vorticity components were measured simultaneously using an eight-hot wire vorticity probe in the intermediate region $x/D = 10$ of a yawed stationary circular cylinder wake. It was found that when $\alpha \leq 15°$, the maximum coherent concentrations of the three vorticity components do not change with α. However, when α is increased to 45°, the maximum concentrations of the coherent transverse and spanwise vorticity components decrease by about 33% and 50%, respectively, while that of the streamwise vorticity increases by about 70%, suggesting that the strength of the primary vortices shed from the yawed cylinder decreases and the three dimensionality of the flow is enhanced.

1.3 Flow past curved circular cylinders

Although there is a considerable amount of research on yawed cylinders, as seen in the brief review of section 1.2, the wake behind curved or deformed cylinders have received much less attention, perhaps because of the higher degree of complexity involved in the three-dimensional geometry. Begak et al. (1985) published a short paper reporting an investigation with yawed and curved cylinders in a wind tunnel, obtaining two main conclusions from this experimental work. The first was that reducing the radius of curvature of the cylinder induces a reduction in the Strouhal number, and the second, that the frequency of the vortex shedding along the model remains constant. No further studies on curved cylinders are reported by these authors, however. Recently, detailed investigations of the flow past curved cylinders have been carried out with the help of DNS. This studies have considered stationary geometries (Miliou et al., 2003a,b, 2005, 2007) as well as oscillating geometries (De Vecchi et al., 2008, 2009). The curved cylinder in all these cases consisted of a quarter section of a ring.

In order gain preliminary understanding of the flow dynamics that develop past a curved cylinder, Miliou et al. (2003b) performed simulations at a Reynolds number of 100. Different inflow velocity profiles and inflow directions were used in this study. They observed that when the flow acted normal to the plane of curvature, a shedding pattern similar to that corresponding to a uniform cylinder was produced, i.e. in-phase parallel shedding. A shear velocity profile was found to be more significant than the effects of curvature in this case. When the flow was in the direction parallel to the plane of

curvature of the cylinder, the shedding of vortices was found to be less energetic as the cylinder bends to become aligned with the main flow.

The investigation on the wake of curved circular cylinders with the main flow direction parallel to the plane of curvature was continued by Miliou et al. (2007). Computations using three-dimensional spectral/*hp* at Reynolds numbers of 100 and 500 were conducted in order to study the shedding dynamics. Fully three-dimensional wake dynamics were observed when the flow was directed towards the outer face of the bend (convex configuration), with the vortex shedding driven mainly from the vortices shed at the top of the cylinder. However, when they directed the free stream towards the inside of the bend (concave configuration), no vortex shedding was detected. An explanation suggested to this latter phenomenon was that the shedding was suppressed by the strong axial flow driven by the horizontal extension attached to the curved cylinder. Furthermore, the numerical results presented in this study were contrasted qualitatively with experimental work. A model of a cylinder with the same aspect ratio as in the DNSs was towed in a water tank at Reynolds numbers equal to that of the simulations, obtaining flow visualizations with dye markers. Good qualitative agreement was obtained between the numerical simulations and the flow visualizations.

De Vecchi et al. (2008) further extended these studies by performing numerical simulation of forced oscillations at $Re = 100$ on the same geometries tested in Miliou et al. (2003b, 2007). In a first stage, the cylinder was forced to transversely oscillate at a fixed amplitude, while the frequency was varied around the Strouhal value. Although the wake topology of the convex and concave configurations was noticeable different, both geometries were characterized by in-phase vortex shedding with the vortex cores bent according to the cylinder's curvature. This is in accordance with the observations made by Ramberg (1983) for oscillating yawed cylinders. Of particular importance was the fact that the concave configuration, which was shown to suppress the vortex shedding when the body was stationary (Miliou et al., 2007), exhibited a primary instability in the presence of a forced motion. An oscillatory roll motion, which consisted in a rotation about the axis of the bottom section (horizontal extension), was also imposed to the body. This case exhibited out-of-phase vortex shedding and straight vortex cores.

More recently, De Vecchi et al. (2009) forced the convex configuration to sinusoidally

vibrate in the cross-flow direction at different amplitudes and frequencies. The three-dimensional numerical simulations were again performed at $Re = 100$. The shedding past the bluff body was influenced by curvature and the flow behaviour depended on whether the frequency ratio f_s/f_0 was within or outside the lock-in region for a straight cylinder. Here f_0 is the input frequency for the oscillatory motion, and f_s is the Strouhal frequency for a stationary uniform cylinder at $Re = 100$. Within the lock-in region the shedding exhibited a 2S mode, whereas outside this region a so-called "weak" form of shedding consisting of two pairs of counter-rotating vortices (per cycle) appeared in the top part of the geometry. Finally, at lower amplitudes of oscillation and frequencies below the St value for a straight cylinder, dislocations arose in the middle part of the curved geometry.

1.4 Effects of uniform shear as an inflow boundary condition

In addition to geometry, the wake dynamics of the flow past bluff bodies are also affected by the incoming flow condition. This issue is of particular relevance to the marine industry, since ocean currents interacting with waves, wind and the sea bottom have non-uniform vertical velocity profiles. The experimental (Kappler et al., 2005, Mair and Stansby, 1975, Maull and Young, 1973, Sumner and Akosile, 2003, Woo et al., 1989) and numerical (Mukhopadhyay et al., 1999, 2002, Silvestrini and Lamballais, 2004) investigations of the flow past a circular cylinder in uniform shear flow have revealed the presence of secondary flows, as well as oblique and cellular vortex shedding, as a direct consequence of the inflow condition.

The experimental study by Maull and Young (1973) gave early evidence of the cellular pattern in the vortex shedding behind a bluff body when *uniform shear* is imposed as an incoming flow condition, i.e. a velocity profile that varies linearly in the vertical direction. The model they employed consisted of a semi-elliptic nose followed by a parallel-sided section. The experiments were performed in a low-speed wind tunnel at $Re = 2.85 \times 10^4$, measuring base pressure as well as vortex shedding frequency with a hot-wire anemometer. A spectral analysis based on the velocity measurements revealed the occurrence of shedding cells with constant frequency along the vertical axis. They

suggested that the splitting of the vortex shedding in cells of constant frequency occurred in order to maintain certain degree of coherence in the shed vortices. A constant frequency is required over certain lengths for coherence, but at the same time the flow tends to maintain a constant St with basis on the local velocities, thus the shedding frequency is forced to vary in this cellular pattern. In connection with this, a variation of the pressure coefficient within each constant frequency cell was also reported. Furthermore, the presence of horseshoe vortices was mentioned as an important physical mechanism in this study. These vortices appear because the shear flow contains a vorticity component normal to the plane of the flow, thus the vorticity filaments originally perpendicular to the flow direction are progressively tilted and bent into the streamwise direction as they approach the body. It was suggested that when interacting with the Kármán vortex street, this streamwise vorticity component caused the division between the vortex shedding cells. This was supported by experiments in which a delta wing was placed in the bluff body to produce streamwise vorticity in uniform inflow, obtaining the same pattern of cell division as in the shear flow tests.

A review of the results obtained by Maull and Young (1973), accompanied by results from new experiments of the flow past a bluff body in uniform shear, were reported by Mair and Stansby (1975). The experiments were performed with cylinders of circular and D-shaped section in a wind tunnel, where measurements of base pressure and vortex shedding frequency at different spanwise positions were carried out. Spanwise cells of constant shedding frequency were also reported in this case. A similar mechanism to that proposed by Maull and Young (1973), i.e a concentration of streamwise vorticity between cell boundaries, was suggested as an explanation to the cellular vortex shedding phenomenon. The largest cell lengths observed were in the range $4D$ to $6D$, suggesting that there is an upper limit to the length of any spanwise vortex cell. Above this limit the vortices have a tendency to lose their coherence. Inclination or obliqueness of the primary vortices was directly observed by introducing smoke to the stream, and explained by the spanwise variation of the inflow velocity, which carries the vortices downstream at different velocities along the span. Although there were some differences in the shape of the frequency spectra, results with the D-shaped section were closely similar to those reported by Maull and Young (1973). Additionally, the influence of the aspect ratio H/D (where H is the spanwise length of the cylinder and D its diameter), the boundaries, and the use of end plates was explored.

Mukhopadhyay et al. (1999, 2002) conducted three-dimensional numerical simulations of uniform shear flow past a circular cylinder at a mean Reynolds number of 131.5. The cylinder spanned 24 diameters, and free-slip and non-slip plates boundary conditions were tested. Previous experimental observations such as dislocations and obliqueness of the vortex shedding were reproduced in this study, obtaining always shedding frequencies lower than those corresponding to parallel shedding (calculated from correlation formulas at the same local Reynolds numbers). Additionally, it was determined that the cell boundaries moves continuously in time. The lengths of the vortex shedding cells were observed to be between $3D$ and $7D$, with the larger cells located at the low velocity end.

Numerical simulations involving shear flow are affected by the vertical extension of the shear zone, the vertical domain size (span) and the shear intensity. These were addressed in the study by Silvestrini and Lamballais (2004), which conducted DNSs at a mean Reynolds number of 200 using four different flow configurations. The velocity profile considered in this study consists of two regions of constant velocity at the ends of the cylinder, and a region with constant shear between these two regions of constant velocity. This profile shape, according to the authors, enables preservation of the free-slip boundary condition at the spanwise ends while considering shear flow extending over a wide region. The free slip condition imposes a kinematic blocking associated with the vertical velocities at the spanwise ends, which involves the formation of sharp gradients of the vertical velocity at the boundaries. Despite these effects, the authors mention that the main features of the wake dynamics were preserved when the free-slip walls were used instead of the periodic boundary condition. Based on visualizations of isosurfaces of the square-root of the enstrophy, or vorticity modulus $|\boldsymbol{\omega}| = (\omega_x^2 + \omega_y^2 + \omega_z^2)^{1/2}$, it was noticed that the extent of the regions where oblique vortex shedding was found do not necessarily coincide with the regions of constant shear. Moreover, since the vortices were observed to propagate from the high speed region towards the low speed region, the angle of the vortex shedding was associated with the characteristic speed of vortex shedding propagation in the spanwise direction. It is noteworthy that the range of Reynolds number used in this study involves instabilities corresponding to the transition to three-dimensionality (Williamson, 1988), and thus the dislocations attributed to the shear effects were not isolated.

1.5 Motivation

The main objective of the present work is to study the wake dynamics of the flow past a curved circular cylinder. Flows past this type of bluff body have direct engineering significance in the field of offshore marine applications involving catenary risers, cables and pipelines, which are cylindrical structures that resemble the shape of the curved cylinder studied here. When subjected to hydrodynamic loads, the wake past such structures may contain complex three-dimensional flow patterns. In addition, the shedding of vortices is accompanied by fluctuating pressure forces in a direction transverse to the flow, leading to vortex induced vibration (VIV) which, due to fatigue or damage accumulation, may trigger structural failure. Although VIV is out of the scope of this work, a detailed knowledge of the flow physics when the body is fixed constitutes a first step towards more elaborated studies.

It is well known that waves and currents have non-uniform velocity profiles that, as seen in section 1.4, affect the flow past a bluff body. Due to interactions with the curvature effects described by Miliou et al. (2007), the three-dimensional effects induced by shear flow in a straight cylinder are not easily extended to a curved circular cylinder. It is therefore interesting to explore the effects of shear flow combined with curvature, since this may reveal new flow physics.

In the present thesis, the results from DNSs of the flow past a curved circular cylinder in uniform shear flow are presented and discussed. This will enable the study of the effects of curved geometry, uniform shear-rate and aspect ratio on the instantaneous vortex topology, recirculation region as well as on the shedding mechanisms. The previous DNSs with this geometry were performed using a spectral/*hp* element Navier-Stokes solver and a boundary-fitted grid. In the present study the solution of the Navier-Stokes equations is obtained with a Cartesian grid solver, and a direct forcing Immersed Boundary Method (IBM) is used to implement the non-slip boundary condition at the solid surfaces. It is thus intended to check the overall performance of these methods for the complex geometry involved. In order to achieve this comparison, we intentionally considered a convex-shape geometry identical to that studied by Miliou et al. (2007) with uniform inflow in the first set of simulations.

Part of this work has been presented at the conferences 8^{th} *International ERCOFTAC Symposium on Engineering Turbulence Modelling and Measurements* (ETMM8) in Marseille, France; and the 5^{th} *European Conference on Computational Fluid Dynamics* (ECCOMAS CFD 2010) in Lisbon, Portugal; both in June of 2010. The papers published in the proceedings of both conferences are included as appendices.

Chapter 2

Numerical Solution of the Navier-Stokes Equations

This chapter contains a summary of the relevant issues associated to the numerical solution of the Navier-Stokes equations, starting from the governing equations for the incompressible flow past a bluff body. Section 2.2 contains a description of the code MGLET, including the numerical schemes employed to discretize the Navier-Stokes equations in time and space, and a discussion regarding parallelization of the code. Finally, the immersed boundary technique is discussed in section 2.3.

2.1 Governing equations of flow

The dynamics of the flow are described by the time-dependent Navier-Stokes equations for an *incompressible Newtonian fluid*. These equations are normalized by the cylinder's diameter D and the inflow velocity U_∞ as

$$u_i = \frac{\tilde{u_i}}{U_\infty}, \qquad t = \frac{\tilde{t}}{T_0}, \qquad x_i = \frac{\tilde{x_i}}{D}, \qquad p = \frac{\tilde{p}}{P_0},$$

where

$$T_0 = \frac{D}{U_\infty}, \qquad P_0 = \frac{1}{2}\rho U_\infty^2.$$

Applying this normalization, the non-dimensionalized equations for mass conservation and momentum can thus be written in tensorial notation as

$$\frac{\partial u_i}{\partial x_i} = 0, \tag{2.1}$$

$$\frac{\partial u_i}{\partial t} + u_j \frac{\partial u_i}{\partial x_j} = -\frac{\partial p}{\partial x_i} + \frac{1}{Re} \frac{\partial^2 u_i}{\partial x_j \partial x_j}. \tag{2.2}$$

Here, the Reynolds number is based on the cylinder diameter and the inflow velocity $Re = U_\infty D/\nu$.

2.2 The Navier-Stokes solver MGLET

The governing equations (2.1) and (2.2) have been directly solved with the code MGLET. This section briefly explains the discretizations schemes used in this code, the solution algorithm implemented, and its parallelization.

2.2.1 Finite volume discretization

In the finite-volume code MGLET, the Navier-Stokes equations for an incompressible fluid (2.1) and (2.2) are discretized on a staggered Cartesian mesh with non-equidistant grid-spacing (Manhart, 2004). The starting point for the finite volume discretization is the integral form of equation (2.2)

$$\frac{\partial}{\partial t} \int_\Omega u_i \, \mathrm{d}\Omega + \int_S u_i \boldsymbol{u} \cdot \boldsymbol{n} \, \mathrm{d}S - \int_S \left(\frac{1}{Re} \operatorname{grad} u_i - p \right) \boldsymbol{i}_i \cdot \boldsymbol{n} \, \mathrm{d}S. \tag{2.3}$$

Here the velocities u_i and pressure p are defined on a staggered arrangement in the control volume shown in figure 2.1. The *mid-point rule* is employed to approximate the fluxes with the variables defined on the control cell. The velocities $u(i+1/2, j)$ and $u(i, j+1/2)$ at the faces of the momentum cell for the u-velocity are obtained by linear interpolation. A central difference scheme is used to approximate the derivatives in the x- and y-directions at the positions $(i+1/2, j)$ and $(i, j+1/2)$ respectively, ensuring second order accuracy in the spatial discretization of the convective and diffusive terms (Ferziger and Perić, 2002).

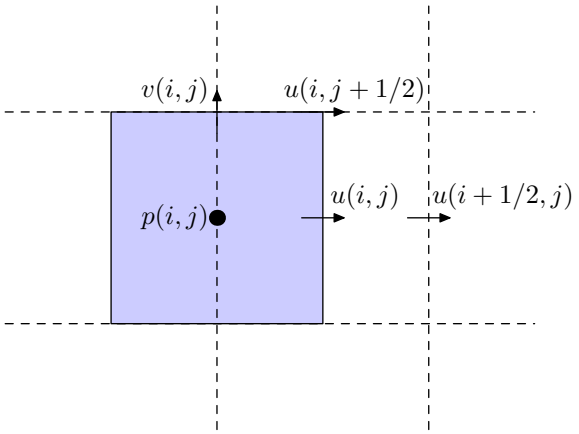

FIGURE 2.1: Control volumes for the u-velocity (dashed lines) and the pressure (gray) in the staggered grid.

2.2.2 Temporal discretization and solution of the Poisson equation

For the time advancement of the momentum equations, an explicit third-order Runge-Kutta scheme is used (Williamson, 1980). The pressure at the new time level $n+1$ is found by solving the Poisson equation for the pressure correction $\Delta p^{n+1} = p^{n+1} - p^n$

$$\nabla^2(\Delta p^{n+1}) = \frac{1}{2\Delta t}\mathrm{div}(\boldsymbol{u}^*) \tag{2.4}$$

where $\boldsymbol{u}^*$ is an intermediate velocity field computed from the momentum equation.

Equation (2.4) is solved iteratively by Stones strongly implicit procedure (SIP), yielding intermediate pressure p^* and velocity $\boldsymbol{u}^*$ fields at each iteration. According to equation (2.1) for mass conservation, the divergence of the intermediate velocity field $\mathrm{div}(\boldsymbol{u}^*)$ must approach zero as the number of iteration increases. In order to meet this condition, the divergence of the intermediate velocity field must be reduced to some value below a tolerance ϵ, which is defined by the user. When $\mathrm{div}(\boldsymbol{u}^*) \leq \epsilon$, the intermediate pressure and velocity fields are updated at the next time step t^{n+1} as $p^{n+1} = p^*$ and $\boldsymbol{u}^{n+1} = \boldsymbol{u}^*$ respectively.

Defining k as an iteration counter, the three steps constituting one iteration are the pressure estimate

$$\Delta p^{k+1} = \Omega\frac{1}{2\Delta t}\mathrm{div}(\boldsymbol{u}^*)^k\frac{1}{1/(\Delta x)^2 + 1/(\Delta y)^2 + 1/(\Delta z)^2}, \tag{2.5}$$

the correction of the velocity field

$$(\boldsymbol{u}^*)^{k+1} = (\boldsymbol{u}^*)^k + 2\Delta t \nabla(\Delta p^{k+1}), \tag{2.6}$$

and the correction for the pressure

$$p^{k+1} = p^k + \Delta p^{k+1}. \tag{2.7}$$

An overrelaxation factor Ω is introduced in equation (2.5) in order to obtain the same convergence properties as a conventional Gauss-Seidel iteration with successive overrelaxation (SOR); details of the SOR method are given by Ferziger and Perić (2002).

2.2.3 Parallelization

The most reliable approach to the prediction of turbulent flows is to solve the Navier-Stokes equations using DNS, which provides all the relevant turbulent length and time scales. However, as the Reynolds number increases, the computation times and memory requirements become too high and parallel processing has to be taken into account.

The code MGLET is designed to run efficiently on vector and parallel computers (Manhart et al., 2001), making it suitable for large scale computations on High Performance Computing (HPC) facilities. When running on several processors (it can run as a single-grid code as well), the parallelization algorithm generates multiple grid blocks that are handled with single-grid subroutines. These subroutines were originally part of the code before it was parallelized. The domain decomposition, i.e. division of the grid in an arbitrary number of subgrids according to the number of processors, can be done in two directions. Message Passing Interface (MPI) is the communication protocol that allows for communication between different processors. A *red-black algorithm* is employed in order to interchange data between neighbouring grids for the velocity pressure iterations specified in equations (2.5) to (2.7). This parallel code was tested in massive parallel machines and vector supercomputers by Manhart et al. (2001), who reported that the performance scales well with the problem size and the number of processors.

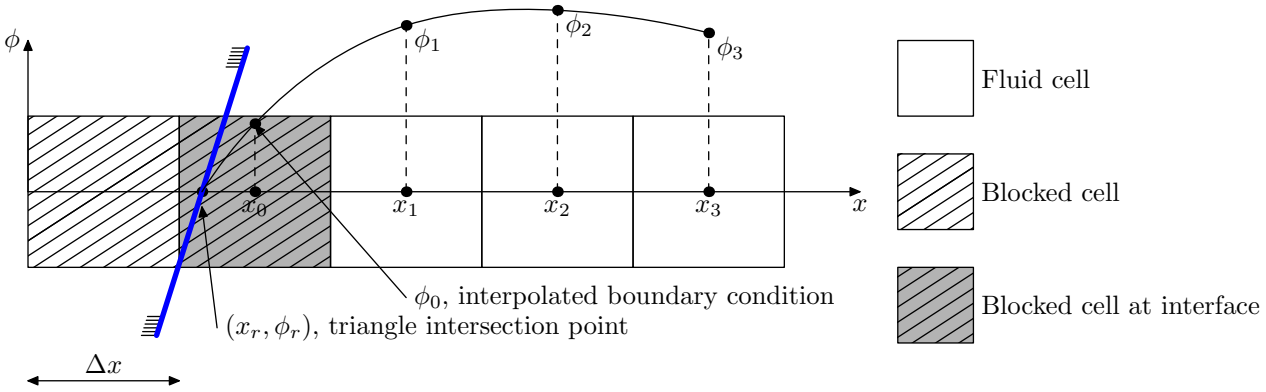

FIGURE 2.2: One-dimensional stencil for the interpolation in the x-direction using the IBM method; the body boundary corresponds to the thick blue line. Adapted from the work by Peller et al. (2006).

2.3 The Immersed Boundary Method

At the walls, the non-slip and non-impermeability conditions are taken into account by using a *direct forcing Immersed Boundary Method* (IBM). Basically, the cells at the fluid-solid interface are transformed into internal boundary conditions on the corresponding computational domain by using higher order interpolation from the fluid cells in the vicinity of the body. This method represents a simple way to deal with complex geometries avoiding the need to generate a body fitted grid. A detailed review of the IBM method is found in the work by Mittal and Iaccarino (2005).

The general stencil configuration for the IBM method is depicted in figure 2.2 for the one-dimensional case. Here ϕ represents one of the velocity components, ϕ_0 is the internal Dirichlet boundary condition, ϕ_r the value at the wall; and ϕ_1, ϕ_2 and ϕ_3 the values in the fluid used for the interpolation. The internal boundary condition based on interpolation from N neighboring cells is determined by the following expression

$$\phi_0 = \left(\sum_{i=1}^{N} \alpha_i \phi_i \right) + \alpha_r \phi_r \tag{2.8}$$

where α_i and α_r are the interpolation coefficients for the variable ϕ at the fluid cells and the body, respectively.

As mentioned above, MGLET uses a Cartesian staggered grid, which means that the boundaries between velocity and pressure cells do not coincide (see 2.1). The blocking strategy for the IBM method is pressure oriented, then the blocked cells are pressure cells

that lie within the surfaces that demarcate the solid walls. According to this criterion, the blocked velocity cells are those touched by the blocked pressure cells.

The interpolation can be either carried out by Lagrange polynomials or using least squares interpolation. It was shown by Peller et al. (2006) that the interpolation coefficients α_i and α_r depend only on the geometry, thus they can be determined in a preprocessing step. In order to account for three-dimensionality, weighting factors are estimated in the different directions to compute ϕ_0. Finally, the computational representation of the body can be done analytically or using a non-structured mesh consisting of triangles.

Chapter 3

Flow Configuration and Simulation Tests

In this chapter, the basic geometry and flow configuration used for the simulations is presented in section 3.1. In section 3.2, relevant computational issues such as boundary conditions, the grid resolution and parallelization are discussed. Finally, the influence of the computational domain size in different directions is presented in section 3.3.

3.1 Problem definition

Figure 3.1 shows a schematic view of flow past a curved cylinder which is composed of a quarter segment of a ring and a horizontal extension. Of particular importance in curved cylinder flows is the non-dimensional radius of curvature. This dimensionless parameter is defined as the ratio of the radius of curvature of the quarter-ring R to its cross-sectional diameter D. In the present set of simulations we consider a flow configuration identical to that of Miliou et al. (2007). This consists of a quarter-ring with curvature ratio $R/D = 12.5$ and a horizontal extension of length $10D$ between the end of the bend and the outflow plane; the free-stream corresponds to uniform flow parallel to the plane of curvature and directed to the outside region of the bend (convex configuration). Throughout the present work, the span s is defined as the arc-length of the curved cylinder measured from the top plane; i.e. $s = R\theta$ with θ the angle measured in radians from the top plane.

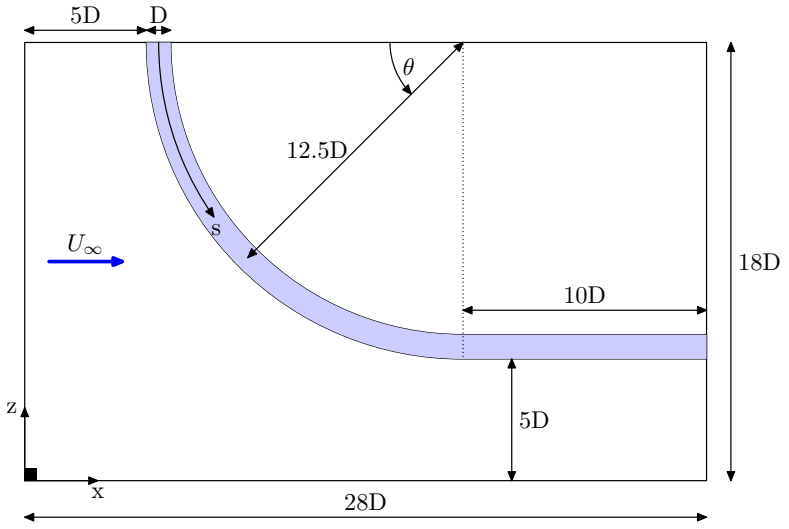

FIGURE 3.1: Computational domain size, geometry and flow configuration shown at the middle (x, z)-plane. The size of the computational domain is $28D$, $11D$ and $18D$ in the x-,y- and z-directions, respectively. The inflow is uniform in this case and denoted by U_∞. The spanwise coordinate s is measured along the cross-sectional axis following the curvature of the cylinder from the top plane, varying between 0 and $19.6D$ at the end of the bend.

Miliou et al. (2003b) selected this geometry according to the generic shape for a catenary riser. The top portion nearly perpendicular to the inflow is directed towards the offshore vessel, while the length of the horizontal extension was selected in order to allow the wake to evolve and stabilize. Perhaps a more realistic approach would consider the vertical extension lying in the seabed rather than hanging in the free-stream; although this was initially addressed by Miliou et al. (2003b), no further investigations were done with this configuration.

3.2 Simulation parameters and implementation

In the first set of simulations, the dimensions of the grid in each direction are $N_x = 400$, $N_y = 150$ and $N_z = 258$, resulting in a total of 15.48×10^6 grid points. Tabulated values of boundary layer thickness versus Reynolds number for a straight uniform circular cylinder (Zdravkovich, 1997) were used to estimate the boundary layer thickness δ, resulting in $\delta \approx 0.5D$ at $Re = 100$. Another possibility is to use equations for the viscous flow near a stagnation point proposed by Hiemenz (see White, 2006). The boundary layer thickness δ according to this approach is given by

(*a*) (*b*)

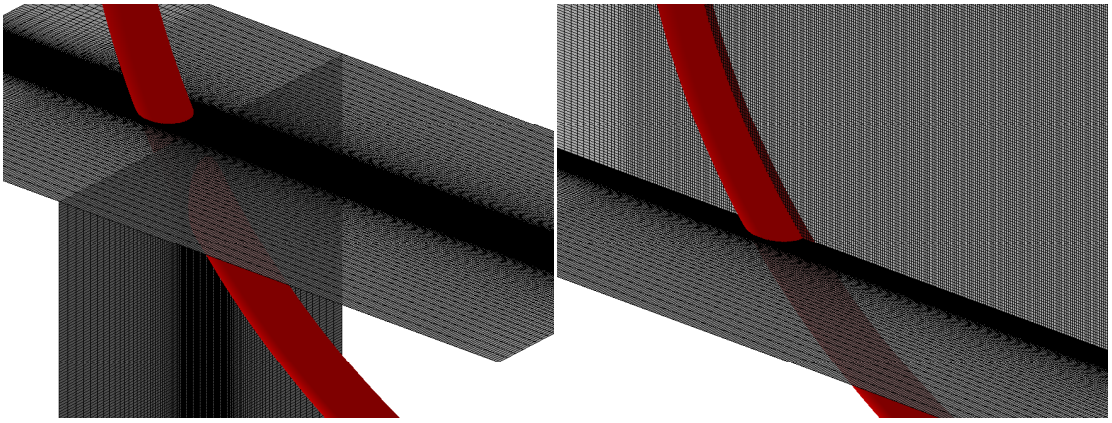

FIGURE 3.2: Detail of the $400 \times 150 \times 258$ Cartesian mesh around the curved cylinder . (a) View of the (x, y)- and (y, z)-planes; (b) (x, y)- and (x, z)-planes.

$$\frac{\delta}{D} = \frac{1.2}{\sqrt{Re}}. \tag{3.1}$$

At $Re = 100$, the boundary layer thickness obtained from equation (3.1) is $\delta \approx 0.12D$. Of these two approaches, perhaps the former gives a more reliable estimation of δ/D than the latter. The reason is that the values given by Zdravkovich (1997) are obtained from experimental data for circular cylinders, while the equation (3.1) consist on a general formulation for the boundary layer close to a plane stagnation point, giving only a rough estimate of δ.

In order to adequately resolve the details of the boundary layer and the wake without using too many grid points where not required, non-uniform grid spacing is used in the three spatial directions. The minimum grid spacing for the uniform and shear flow cases are $\Delta x/D = 0.05$, $\Delta y/D = 0.02$ and $\Delta z/D = 0.057$ in the x-, y- and z-directions respectively. Different planes of the mesh close to the body are shown in figure 3.2, depicting the clustering of points in the vicinity of the body.

Figure 3.3 shows the blocking of the Cartesian grid by the IBM method in the (x, y)- and (y, z)-planes. The *least squares method* was chosen as interpolation scheme since it possesses better stability properties than the Lagrange interpolation method (Peller et al., 2006). The body composed of a quarter-ring and a horizontal extension was

represented by a structured mesh consisting of triangles. The resolution of this mesh was rather high in order to avoid errors in the representation of the curved surfaces.

In many physical situations the flow is not confined, and boundary conditions are therefore not necessary. In a numerical simulation, however, the computational domain has a finite extension and the confination problem has to be taken into account. A suitable choice of boundary conditions is therefore essential in order to not confine the computational domain from the external flow. For the cases studied, the boundary conditions imposed are:

i. A uniform velocity profile at the inlet ($u = U_\infty$).

ii. At the walls of the curved cylinder, non-slip and non-impermeability conditions, i.e. $\boldsymbol{u} = 0$.

iii. A free-slip condition on the horizontal top ($z = 18D$) and bottom ($z = 0$) planes,

$$w = 0, \qquad \frac{\partial u}{\partial z} = 0, \qquad \text{and} \qquad \frac{\partial v}{\partial z} = 0; \tag{3.2}$$

as well as on the vertical sides ($y = 0$ and $11D$) of the computational domain:

$$v = 0, \qquad \frac{\partial u}{\partial y} = 0, \qquad \text{and} \qquad \frac{\partial w}{\partial y} = 0. \tag{3.3}$$

iv. At the outlet ($x = 28D$), a Neumann boundary condition was prescribed for the velocities:

$$\frac{\partial u}{\partial x} = 0, \qquad \frac{\partial v}{\partial x} = 0, \qquad \text{and} \qquad \frac{\partial w}{\partial x} = 0; \tag{3.4}$$

in addition the pressure was set to zero ($p = 0$). This gives a fully developed zero stress condition in order to avoid reflections from the outlet.

The constant time step used for the simulations was $\Delta t = 0.005D/U_\infty$, which ensured low values of the maximum Courant number. The flow field evolved to the laminar vortex shedding regime at $tU_c/D \approx 100$, after which statistics were gathered for a period of $300D/U_c$.

The code was run in parallel on an *IBM p*575+ machine. The simulations for this case were run on 48 processors, the domain decomposition consisted of 16 processors in the

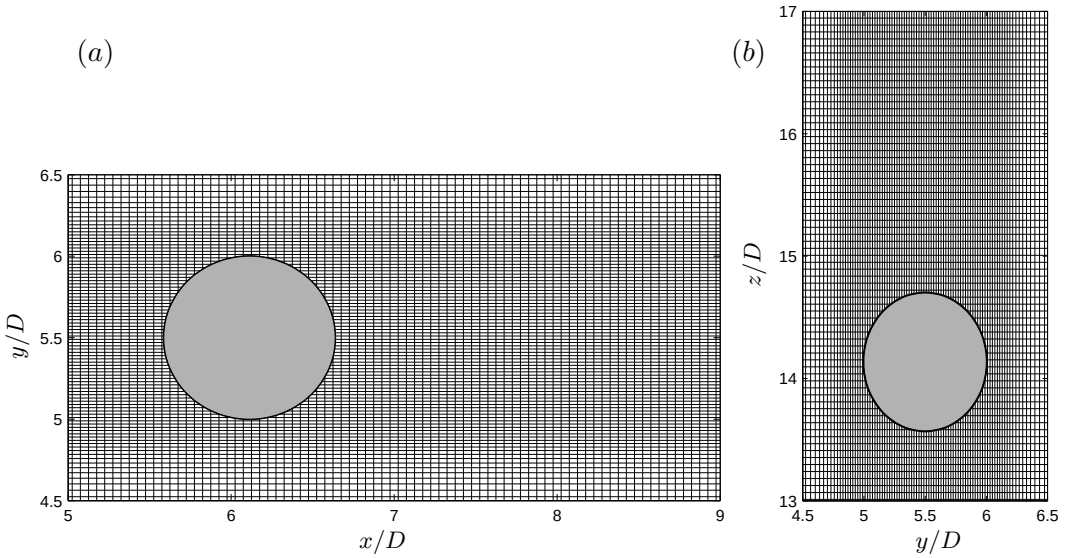

FIGURE 3.3: View of the blocking of cells in the Cartesian mesh by the IBM method. (a) View of the (x, y)-plane at $z/D = 14$; (b) (y, z)-plane at $x/D = 12$.

x-direction and 3-processors in the y-direction. In average, the time required to compute one time-step was 2 seconds, resulting in approximately 33 hours to run the 60000 time steps required to gather statistics.

3.3 Influence of the domain size

The domain size presented in section 3.2 was chosen in order to compare the results obtained with MGLET and the previous published results by Miliou et al. (2007). Before undertaking any further analysis with this domain, the influence of the computational domain has to be analyzed to check if there is any blockage effect. To this purpose, three specific dimensions have been chosen for the analysis of the computational domain: the length X_i, which specifies minimum distance between the inflow boundary and the body, Y_h is the half-width of the domain in the horizontal direction, and Z_u which represents the length of an extension of the curved cylinder in the vertical direction. The minimum grid spacing in the three additional cases were kept the same as those presented in see section 3.2; the Reynolds number is $Re = 100$. The influence of the domain in terms of the Strouhal frequency is summarized in table 3.1.

For the first computational domain denoted by $D1$, the Strouhal frequency attains a value of 0.176; this is in excellent agreement with the Strouhal frequency of 0.1761

Domain	$N_x \times N_y \times N_z$	X_i	Y_h	Z_u	$St = fD/U_\infty$
$D1$	$400 \times 150 \times 258$	$5D$	$5.5D$	0	0.176
$D2$	$432 \times 150 \times 258$	$10D$	$5.5D$	0	0.170
$D3$	$400 \times 240 \times 258$	$5D$	$10.5D$	0	0.170
$D4$	$400 \times 150 \times 360$	$5D$	$5.5D$	$6D$	0.176

TABLE 3.1: Parameters of the different computational domains.

reported by Miliou et al. (2007). Increasing the inflow length X_i by $5D$ yields a Strouhal frequency of 0.170, the same frequency was obtained when the horizontal half-length Y_h is increased by $5D$. This difference in frequency is 3.41%, and although it could be attributed to blockage effects, no experimental data has been published yet (to the knowledge of the author) to validate this argument; the experimental data mentioned by Miliou et al. (2003b, 2007) consists only of qualitative data used for visualization purposes.

As discussed in section 1.2, the Strouhal frequency for yawed cylinders decreases with increasing yaw angle α (Van Atta, 1968). As an example, if we use the St-Re relationship for a straight cylinder proposed by Williamson (1998)

$$St = 0.2731 - \frac{1.1129}{\sqrt{Re}} + \frac{0.4821}{Re}, \tag{3.5}$$

we obtain $St = 0.167$ for a straight cylinder at $Re = 100$. Then, for a cylinder with a certain yaw angle we will have that $St \leq 0.167$ at a Reynolds number of 100. By analogy with a yawed cylinder, a similar behaviour may be expected for a curved cylinder. The results from the simulations show, however, that this is not the case since the Strouhal frequencies obtained in the cases $D1$ to $D4$ are higher than those corresponding to a straight cylinder.

The last configuration tested was obtained by adding a vertical extension of $6D$ on the top of the curved cylinder (domain $D4$). This constitutes an addition of approximately 50% of the height of the curved cylinder. The Strouhal frequency in this case remained the same as that without a vertical extension. Additionally, in order to determine if there were any changes in the wake topology by adding this extension, the vortical structures based in the λ_2 method (Jeong and Hussain, 1995) were obtained for the domains $D1$ and $D4$. The scalar quantity λ_2 defines a region of minimum pressure due to swirling motion in an incompressible fluid based on the second largest eigenvalue

of the symmetric tensor $\Omega_{ij}\Omega_{ij} + S_{ij}S_{ij}$, where S_{ij} is the symmetric component of the velocity gradient tensor and Ω_{ij} the antisymmetric part.

$$S_{ij} = \frac{1}{2}\left(\frac{\partial u_i}{\partial x_j} + \frac{\partial u_j}{\partial x_i}\right), \tag{3.6}$$

$$\Omega_{ij} = \frac{1}{2}\left(\frac{\partial u_i}{\partial x_j} - \frac{\partial u_j}{\partial x_i}\right). \tag{3.7}$$

Figures 3.4.(a) and (b) depict that the vertical extension has almost no effect on the shape of the vortex cores, except for a slight distortion between $z/D = 16$ and 18. This slightly wavy shape of the vortex cores in figure 3.4.(b) is probably due to the fact that the vertical extension in the domain $D1$ (figure 3.4.a) has been replaced by a symmetry boundary condition on the top plane.

The analysis presented in this section shows that, despite some minor differences in the Strouhal frequency and in the wake topology, the simulations with the domain $D1$ are be able to predict the three-dimensional flow around the curved cylinder. Moreover, the exact values of the Strouhal frequency for this case are still unknown, and the only available studies for comparison consider a computational domain identical to the case $D1$ (De Vecchi et al., 2008, 2009, Miliou et al., 2003b, 2007).

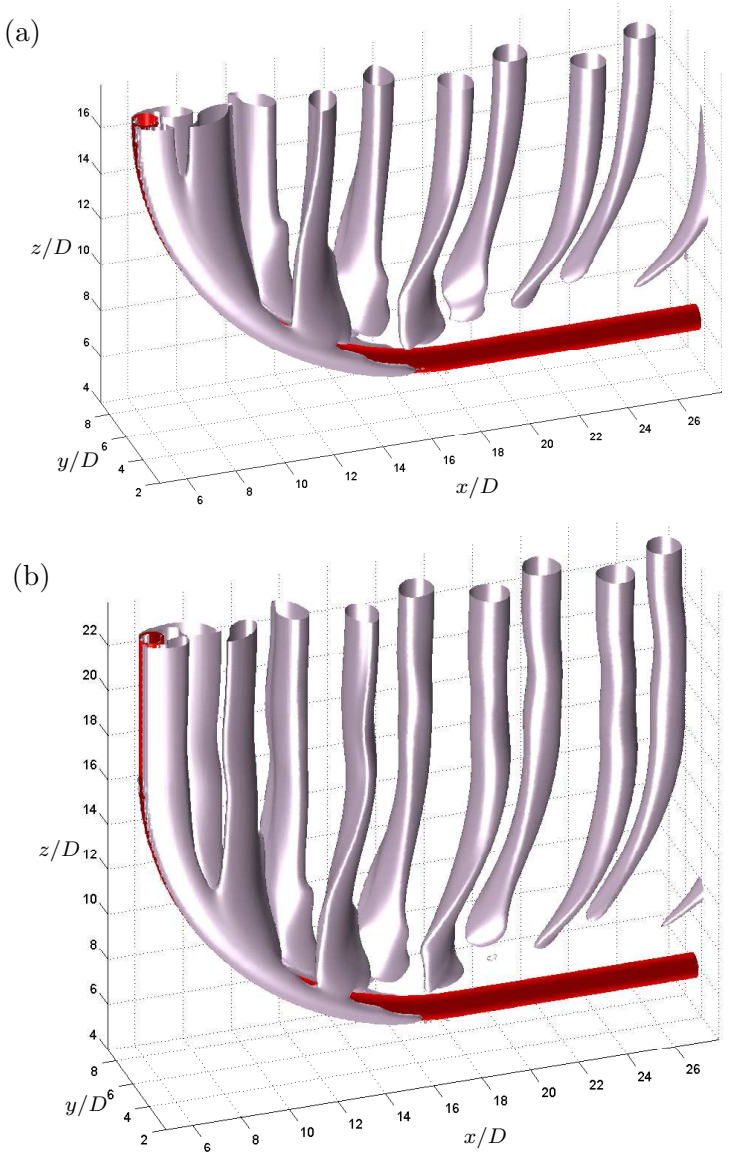

FIGURE 3.4: Perspective view of the vortex cores at $Re = 100$ to analyze the effect of adding a vertical extension. Here the inflow is uniform flow and $\lambda_2 = -0.1$. (a) Computational domain size $L_x \times L_y \times L_z = 28D \times 11D \times 18D$; (b) addition of a vertical extension of $6D$, with computational domain size $L_x \times L_y \times L_z = 28D \times 11D \times 24D$

Chapter 4

Results and Discussion: Uniform Flow

This chapter presents a summary of the results obtained from the simulations when the flow at the inlet is uniform. The main objective here is to compare our results with those published by Miliou et al. (2007). This was a necessary step in order to check the results obtained with the code MGLET, because no experimental data was available for validation purposes. Moreover, these results constitute a basis for comparison when uniform shear flow is introduced as an inflow boundary condition. A second set of simulations at $Re = 100$ was conducted in order to study the effect of doubling the non-dimensional radius of curvature R/D.

One of the difficulties associated with the analysis of the data obtained from these DNSs is the three-dimensional character of the results. While some quantities such as vortical structures can be easily visualized as iso-surfaces, other scalar or vector quantities have to be chosen at a specific location within the flow field. In this work, most of the results that are not presented in three-dimensional form are referred to the middle (x, z)-plane shown in figure 4.1, i.e. the plane at $y/D = 5.5$.

Sections 4.1 and 4.2 present and discuss the results at Reynolds numbers of 100 and 500; the results are associated with stagnation pressure, recirculation region, vortex shedding frequency and wake topology. Section 4.3 is related to the effects of increasing the non-dimensional radius of curvature R/D.

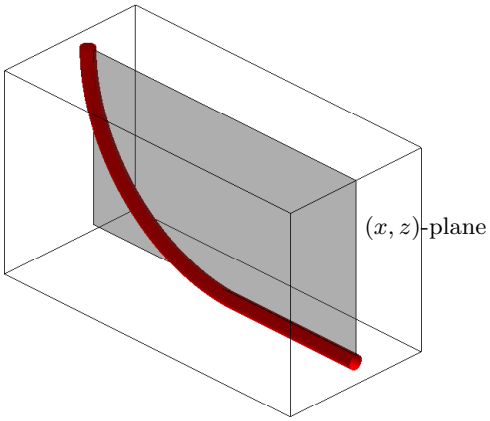

FIGURE 4.1: Location of the middle (x, z)-plane for the analysis of results.

4.1 $Re = 100$

At $Re = 100$, the flow past the convex configuration shown in figure 3.1 is expected to be laminar. Although laminar flows past bluff-bodies rarely occur in practical applications, the laminar wake features give a good starting point to understand the flow physics before moving towards higher Reynolds numbers. The analysis presented herein starts at the near wake with the stagnation pressures and the recirculation region, and then it moves downstream to study the vortex shedding frequency and the wake topology.

4.1.1 Stagnation pressures and recirculation region at $Re = 100$

An interesting feature of the flow field is the variation of the mean pressure along the front and rear stagnation lines. The pressure coefficient is defined as

$$C_p = \frac{p - p_\infty}{\frac{1}{2}\rho U_\infty^2}, \tag{4.1}$$

where p_∞ denotes the pressure at the inlet. The variation of C_p along the stagnation lines up to the horizontal extension is shown in figure 4.2. Along the front stagnation line the pressure gradient is negative (i.e. $\partial C_p/\partial s < 0$). This *favourable pressure gradient* induces an axial flow along the convex face of the quarter ring towards the horizontal cylindrical extension. On the other hand, the rear stagnation line exhibits a positive pressure gradient along the entire span length ($\partial C_p/\partial s > 0$). The general tendency here is that the pressure coefficient decreases as the angle measured from the top plane

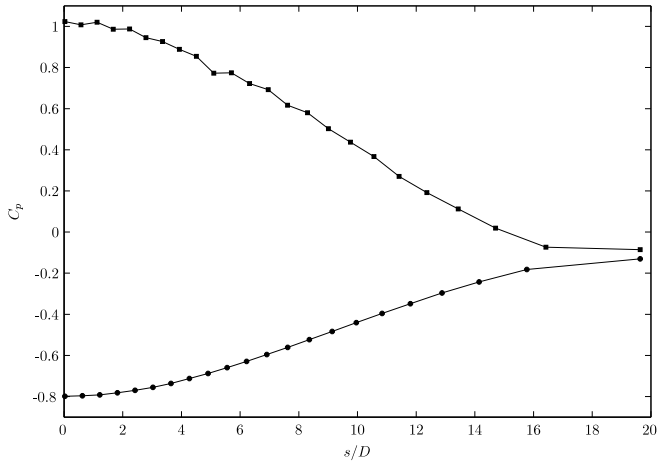

FIGURE 4.2: Mean pressure coefficients C_p along the span of the curved cylinder at $Re = 100$. Here —■—, stagnation pressure coefficient; —●—, base pressure coefficient.

θ increases (see figure 3.1), attaining a value of zero at the location where the curved segment and the horizontal extension meet. A similar phenomenon was reported for yawed cylinders; Zhao et al. (2009), for instance, noted that C_p along the surface of a yawed cylinder decreases with increasing yaw angle, reducing thus the difference in pressure between the front and rear stagnation lines as α increases. They showed, however, that the Independence Principle was valid when the pressure coefficients where normalized by the normal component of the free stream velocity,

$$C_{pn} = \frac{p - p_\infty}{\frac{1}{2}\rho U_n^2}. \tag{4.2}$$

Following this idea, it is expected that when the pressure coefficients for the curved cylinder are normalized by U_n, the C_{pn} values obtained will be close to unity; this normalized mean pressure coefficient has been plotted along the span of the curved cylinder in figure 4.3. It can be noticed in figure 4.3 that the Independence Principle (i.e. $C_{pn} \approx 1.0$) is valid up to $s/D \approx 10$, or $\theta \approx 45°$. At $s/D > 10$, the normalized mean pressure coefficient decreases monotonically on both, front and rear stagnation lines, and the IP ceases to be valid.

Regarding C_p along the front stagnation line, it was commented before that the pressure gradient along the front stagnation line is associated with a spanwise flow along the outer face of the quarter ring towards the horizontal cylindrical extension. The streamlines of the mean flow in the (x, z)–plane shown in figure 4.4 clearly depict this phenomenon; here the streamlines approach the convex face with an increasing bending and sliding

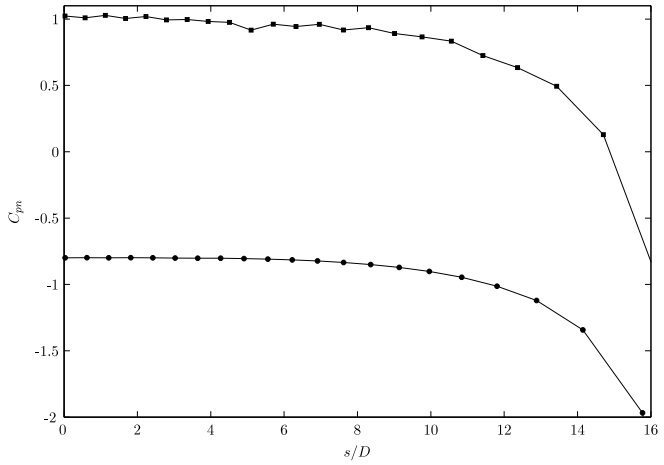

FIGURE 4.3: Mean pressure coefficients normalized by U_n along the span of the curved cylinder at $Re = 100$. The values of C_{pn} are close to one from $s/D = 0$ to $s/D \approx 10$, or $\theta \approx 45°$, revealing that the Independence Principle is valid within this interval. Here —■—, stagnation pressure coefficient; —●—, base pressure coefficient.

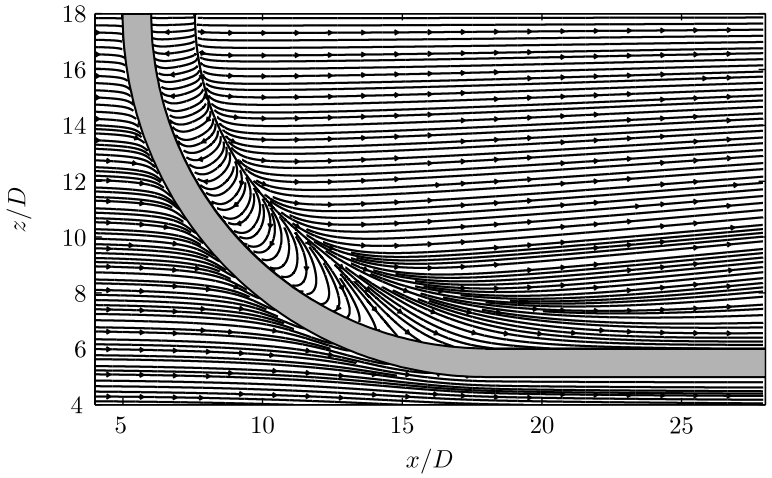

FIGURE 4.4: Streamlines of the mean flow taken at the middle (x, z)-plane at $Re = 100$.

along the cylinder. Curvature is also affecting the back–flow direction in the recirculation region. Close to the top part of the cylinder the vertical component of the back–flow is almost negligible, whereas an increase on this vertical component takes place as we move along the span.

It is well known that the base pressure distribution (i.e. pressure along the rear stagnation line) influences, among other quantities, the size of the recirculation region which develops in the near-wake due to the separation of boundary layers from the surface of the solid body. This is reflected in figure 4.5 where the non-dimensional local separation length L_s/D is plotted along the span of the quarter-ring segment. Here, L_s is defined as the streamwise distance from the rear stagnation line to where the mean streamwise

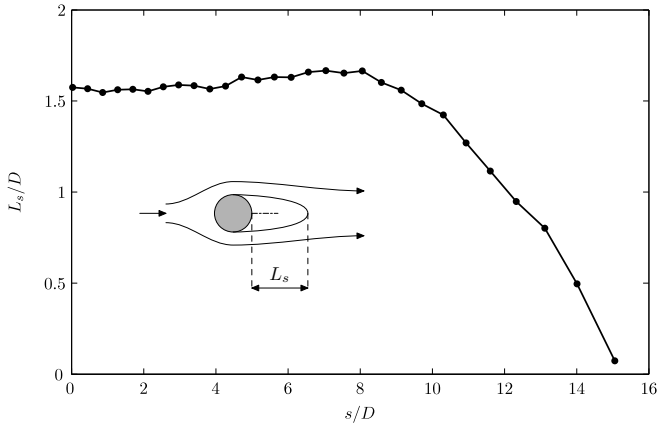

FIGURE 4.5: Recirculation length L_s along the span of the curved cylinder at $Re = 100$.

velocity changes sign from negative to positive. At the top plane ($s/D = 0$), the local separation length is $1.575D$; this value remains approximately constant up to $s/D = 8$, where it starts decreasing monotonically, reaching zero at $s/D \approx 15$, or $\theta \approx 69°$.

4.1.2 Frequency analysis at $Re = 100$

The discussion in the previous section was related to the flow features in the *near–wake*. As the flow evolves downstream, the different types of instabilities created by the separation of the boundary layers will be amplified, leading to a regular shedding of vortices commonly referred to as a Kármán vortex street. In this context, one of the parameters that may affect the frequency of the this vortex shedding is the bluff–body geometry. In order to investigate the influence of curvature on the shedding frequencies, the time evolution of the cross-stream velocity v has been evaluated within the (x, z)–plane of symmetry of the cylinder. For this purpose, a non-dimensional time of $300U_\infty/D$ was considered for the simulation, which covers about 53 shedding cycles in this case.

Shown in figure 4.6(a) is the time evolution of the v-velocity component taken along a sampling line located at $x/D = 18$. The pattern clearly corresponds to regular alternating vortex shedding along a large portion of the sampling line; the fact that no distortions or dislocations arise indicates that the flow is laminar. This is in accordance with the observations reported by Miliou et al. (2007), the vortex shedding pattern corresponds to that of laminar flow, and no dislocations occur despite the non-uniform geometry of the cylinder.

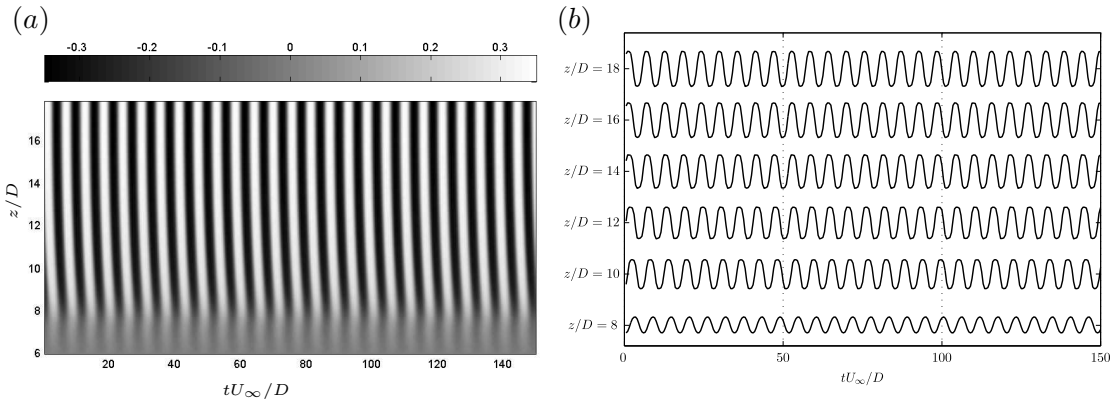

FIGURE 4.6: Time analysis at $Re = 100$ of cross-stream velocity v along a sampling line taken at $x/D = 18$ in the middle (x, z)–plane. (a) Time evolution of the velocity; (b) time trace of velocity.

Further insight of the periodic behaviour of the flow in this case can be gained from the plot of the time traces of the v–velocity at $x/D = 18$, taken at six different positions along the z-axis, as seen in figure 4.6(b). With the exception of the time trace at $z/D = 8$, where the vortex shedding is less energetic, all the traces exhibit the same amplitude and frequency. The suppression of the vortex shedding due to the low local Reynolds number ($Re_n \approx 50$) occurs at $z/D \approx 7$ in this case.

In order to obtain the exact value of the dominant shedding frequency, a spectral analysis with basis on the time-domain signals of the v-velocity has been carried out. The spectra are obtained by the Fast Fourier Transform method (FFT). The signals are sampled each 100^{th} time–step during the simulation; this sampling frequency is lower than the maximum value $D/(U_\infty \Delta t) = 200$ required to avoid aliasing effects (see Persillon and Braza, 1998). The v-velocity signals were taken at $x/D = 18$, and $z/D = 7$ and 16, and their spectra are shown in figure 4.7. The peak in both spectra occurs at $fD/U_\infty = 0.176$, which corresponds to the Strouhal number for this case. Although both cases exhibit a clear peak, the spectrum at $x/D = 7$ in figure 4.7(a) contains less energy because, as mentioned above, the vortex shedding is suppressed at this location due to the low values of Re_n. Furthermore, previous studies conducted on straight cylinders have shown that as the Reynolds increases, an amplification of the odd harmonics occurs (Persillon and Braza, 1998). The incipience of this phenomenon can be seen in figure 4.7(b), here the spectrum contains a the second peak at $3St$.

As discussed in section 1.4, a cellular pattern arrangement consisting of constant frequency cells characterizes flows past straight cylinders which are subject to varying

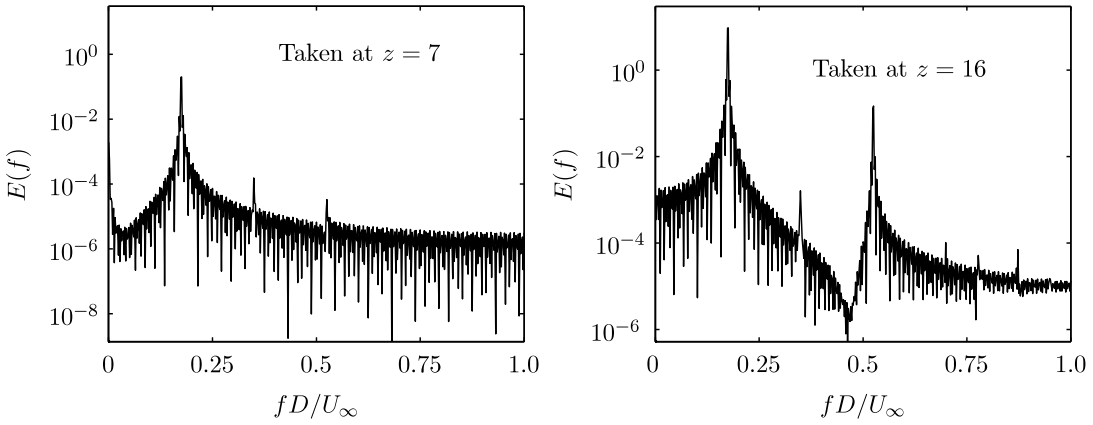

FIGURE 4.7: Power spectra of the v-velocity signal at $Re = 100$, the signal is taken at $x/D = 18$. (a) Spectrum at $z/D = 7$ and; (b) Spectrum at $z/D = 16$.

Strouhal numbers. The results presented here and those published by Miliou et al. (2007) show, nevertheless, that the flow past this type of curved cylinder is characterized by one single Strouhal frequency. This may seem surprising given the variation of the local Reynolds number Re_n based on the normal component of the inflow velocity, and shows therefore that approaches based on a sectional approximation of the flow, or the IP, could be misleading when using this type of geometry. A question that remains open here is whether cellular vortex shedding will occur or not if the radius of curvature R is changed; this will be addressed in section 4.3.

4.1.3 Wake topology at $Re = 100$

The wake topology based on the λ_2–criterion of Jeong and Hussain (1995) is depicted in figure 4.8 at a λ_2 value of -0.1. In order to capture the main features of the wake topology, three different views are shown. The first one is the projection from the side (or (x, z)–plane), where the vortex cores are observed to be almost normal to the flow direction close to the cylinder, and inhabit slight distortions as they move further downstream. A staggered array of vortices with a clear alternating pattern depicted by the projection from the top or (x, y)–plane. The combination of these two characteristics of the wake topology can be seen in the perspective view. The same wake topology was reported by Miliou et al. (2007) from both numerical simulations and experimental visualization studies. They noted an inconsistency between the shape of the primary vortices and the plot of the sectional forces on the cylinder. While the vortices are straight and similar to those observed from the flow past a straight cylinder, the sectional

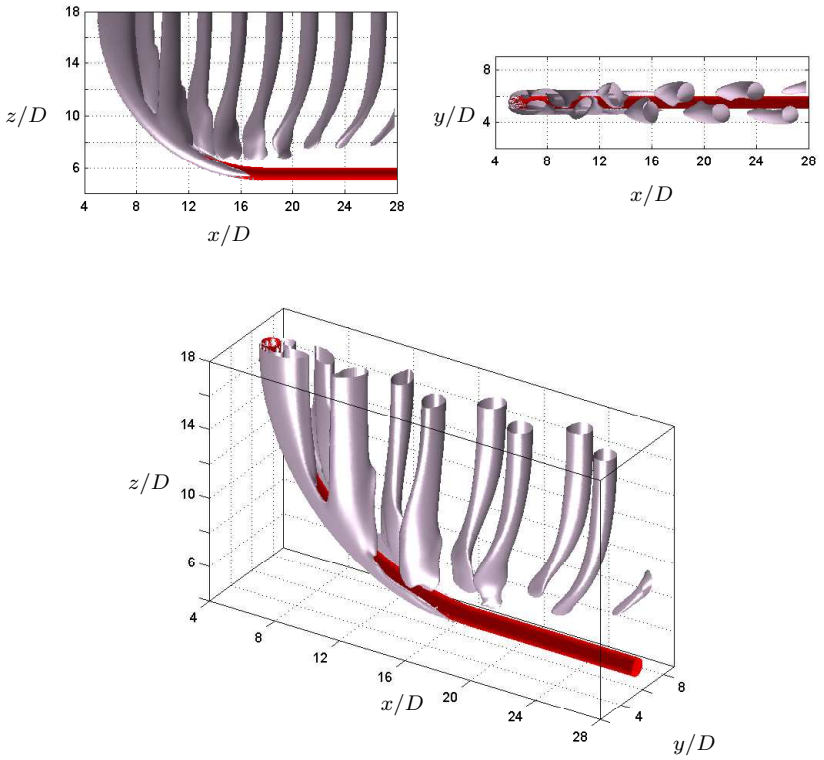

FIGURE 4.8: Wake topology at $Re = 100$ depicted as instantaneous iso–surfaces of λ_2. In the clockwise direction: side view, top view and perspective view of the vortex cores in the wake of the curved cylinder; here $\lambda_2 = -0.1$.

forces plot changed sign along the span at a given time. This discrepancy was attributed to curvature effects by noting that the gradual reduction of the distance between the vortex cores and the cylinder along the span (see figure 4.8) leads to a gradual phase change in the sectional forces.

Further insight of the wake topology can be gained from the iso–surfaces of instantaneous streamwise and vertical vorticity, denoted as ω_x and ω_z respectively. These components of the vorticity vector can be expressed as

$$\omega_x = \frac{\partial w}{\partial y} - \frac{\partial v}{\partial z}, \tag{4.3}$$

$$\omega_z = \frac{\partial v}{\partial x} - \frac{\partial u}{\partial y}. \tag{4.4}$$

The iso–surfaces of ω_x and ω_z have been plotted in figure 4.9, where the black and white iso–surfaces represent streamwise and vertical vorticity, respectively. The shape of the iso–surfaces of ω_z is clearly associated with the shape of the primary vortices shown in figure 4.8; they constitute layers of vorticity that roll–up from the walls of the

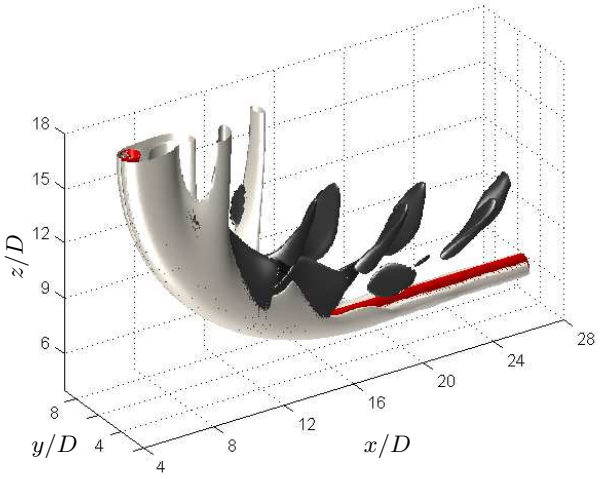

FIGURE 4.9: Isosurfaces of instantaneous vorticity ω_x (black) and ω_z (white) at $Re = 100$. The isosurfaces are obtained at $\omega_x = \pm 0.3$ and $\omega_z = \pm 1.2$.

cylinder. This is not very different from what happens in a straight circular cylinder at this Reynolds number, however. Perhaps the presence of streamwise vorticity is a more interesting phenomenon since this is directly relate to the curvature of the cylinder. The black–isosurfaces reveal that streamwise vorticity is triggered in the lower part of the domain, affecting the vortex shedding pattern with respect to that of a straight circular cylinder. Previous studies have reported that streamwise vorticity may be the cause of cellular vortex shedding, see for instance the work by Maull and Young (1973). This is nevertheless not the case for this particular geometry since, as discussed in subsection 4.1.2, there is a single frequency at which vortices are shed. Further analysis of the amount of streamwise vorticity to break–up the primary vortices may help to determine whether cellular vortex shedding may occur in the wake of a curved cylinder in uniform flow or not.

Finally, in order to study the evolution of the wake at different spatial locations, the instantaneous vorticities ω_x and ω_z were plotted in three consecutive planes (figure 4.10). The instantaneous streamwise vorticities in the (y, z)–planes shown in figure 4.10(a) give a clear picture of the evolution of ω_x in the x–direction. The plane at $x/D = 7$ is located within the recirculation region in the upper portion of the cylinder, and the amount of the streamwise vorticity here is rather low. At $x/D = 12$, two regions of ω_x with different sign can be identified close to the cylinder; here the amount of streamwise vorticity has increased with respect to the previous location. As we move further downstream at $x/D = 18$, the streamwise vorticity decreases in intensity; this reduction may be attributed to the axial flow that develops close to the horizontal extension.

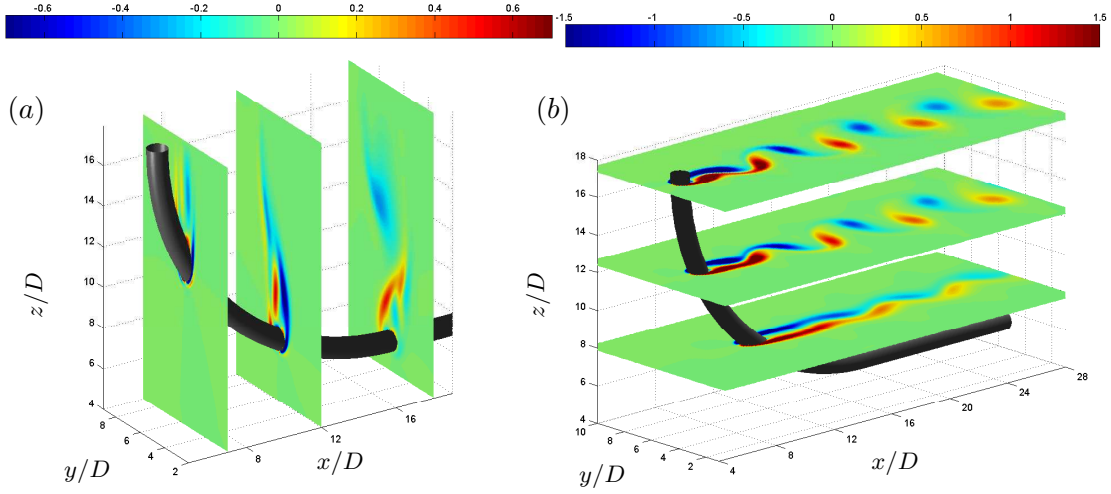

FIGURE 4.10: Isocontours of instantaneous vorticity at $Re = 100$. (a) ω_x in the (y, z)–planes at $x/D = 7$, 12 and 18; (b) ω_z in the (x, y)–planes at $z/D = 8$, 12.5 and 17.5.

A similar analysis may be performed with the vertical vorticity ω_z. Figure 4.10(b) depicts this instantaneous component of the vorticity vector on three consecutive (x, y)–planes. At $z/D = 12.5$ and $z/D = 17.5$ a clear pattern of laminar vortex shedding is observed. On the other hand, even though the wake could be regarded as unsteady at $z/D = 8$, the pattern is more close to the first transition to instability described in section 1.1 for a straight circular cylinder, i.e. Reynolds numbers slightly above 50. In fact, this location is very close to $x/D = 7$, where the vortex shedding is suppressed due to the low value of the local Reynolds number Re_n. In addition, the three consecutive planes (by looking from $x/D = 7$ to $x/D = 17.5$) also depict how the vortex formation region moves upstream as the Re_n increases.

4.2 $Re = 500$

At a Reynolds number of 500, the wake of the flow past a straight circular cylinder contains fine scale three-dimensional structures arranged in an irregular pattern. Whether this regime corresponds to turbulence or not has been discussed in previous studies. For instance, although a chaotic state in the flow at Re around 500 was obtained from the numerical simulations of Karniadakis and Triantafyllou (1992), it was not decisively concluded that the flow at this Re was turbulent; the authors suggested that further analysis of particle trajectories and mean turbulence intensities may help to determine

whether the flow is turbulent or not. In analogy with a circular cylinder, a curved cylinder at $Re = 500$ is expected to exhibit an unstable and irregular general pattern of the flow; this was shown by Miliou et al. (2007) when they reported small vortical structures associated to three–dimensional wake instabilities.

In this section, the results obtained from DNSs at $Re = 500$ are presented in a similar arrangement as the results in section 4.1, in order to enable comparison between both flow regimes. The simulations were conducted using the same mesh as that used for the case at $Re = 100$. This mesh had enough resolution to be able to capture the small scale three-dimensional structures at this Re. In order to verify quantitatively that the current simulation is a fully resolved DNS, the Kolmogorov length scale η was estimated from the energy dissipation rate ϵ as $(\nu^3/\epsilon)^{1/4}$. The adopted grid spacing turned out to never exceed 4η.

4.2.1 Near wake flow at $Re = 500$

The variation of the time–averaged pressure coefficients along the stagnation lines at $Re = 500$ is shown in 4.11. The behaviour of the mean pressures along the front and rear stagnation lines is similar to that exhibited at a Reynolds number of 100. While the stagnation line develops a negative pressure gradient expressed as $\partial C_p/\partial s < 0$, the base pressure along the rear stagnation line exhibits a positive gradient, i.e. $\partial C_p/\partial s > 0$. In this case also, the pressure gradients affect the flow in the vicinity of the body, as seen in the streamlines of the mean flow taken at the middle (x, z)–plane shown in figure 4.12. The streamlines clearly depict the development of an axial flow along the convex face of the quarter ring towards the horizontal cylindrical extension, which seems to slide in a direction tangential to the quarter–of–ring. Regarding the recirculation region, close to the top plane the streamlines are almost parallel to the free–stream, but when proceeding along the span towards the horizontal extension, they are gradually deflected in the anti–clockwise direction (or negative z–direction) until they become parallel to the main flow at the junction between the curved and horizontal segments. This may be explained by the fact that the absolute value of the base pressure decreases monotonically along the span, as seen in figure 4.11. This causes that the main flow gradually prevails over the suction induced by the negative pressure, and therefore the base suction can no longer maintain the streamlines in a direction parallel and opposite in sign to the free–stream.

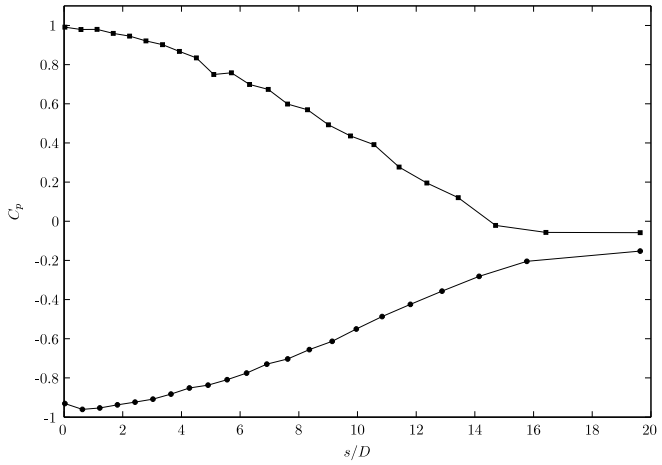

FIGURE 4.11: Mean pressure coefficients C_p along the span of the curved cylinder at $Re = 500$. Here —■—, stagnation pressure coefficient; —●—, base pressure coefficient.

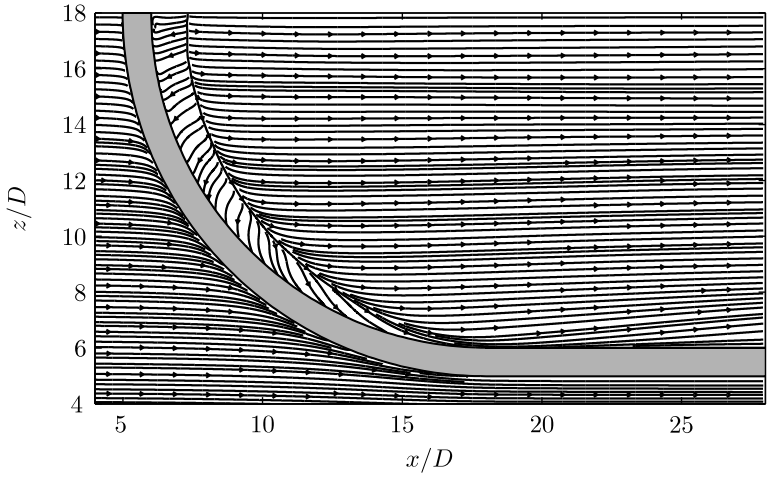

FIGURE 4.12: Streamlines of the mean flow taken at the middle (x, z)–plane at $Re = 500$.

The previous discussion above regarding the recirculation bubble can be complemented by the observation of the instantaneous streamlines shown in figure 4.13. Here the fraction of the streamlines the pass the body close to $y/D = 6$ continue in the direction of the free–stream, as depicted in figure 4.13(a). The remaining streamlines that pass the body at about $y/D = 5$ correspond to the recirculating streamlines which, in addition, move downwards as seen in figure 4.13(a). Figure 4.13 also allows to visualize the complex three-dimensional structure that develops in the near wake.

The variation of the non-dimensional local separation length L_s/D along the span of the curved cylinder at $Re = 500$ is shown in figure 4.14. At this Reynolds number, L_s/D is plotted up to $s/D = 9$ only due lack of resolution in the mean pressure, which is probably attributed to short time to gather statistics (60000 time–steps). Despite this

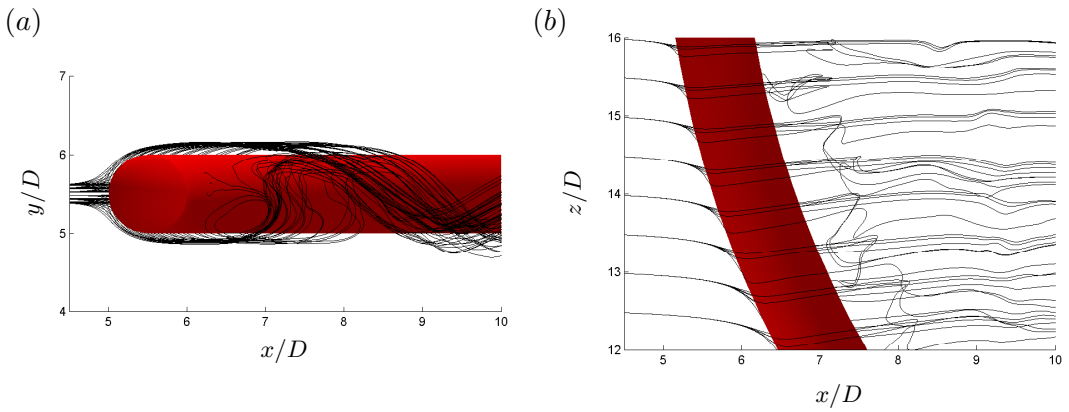

FIGURE 4.13: Instantaneous streamlines at $Re = 500$ close to the recirculation region. (a) Projection in the (x, y)–plane; (b) projection in the (x, z)–plane.

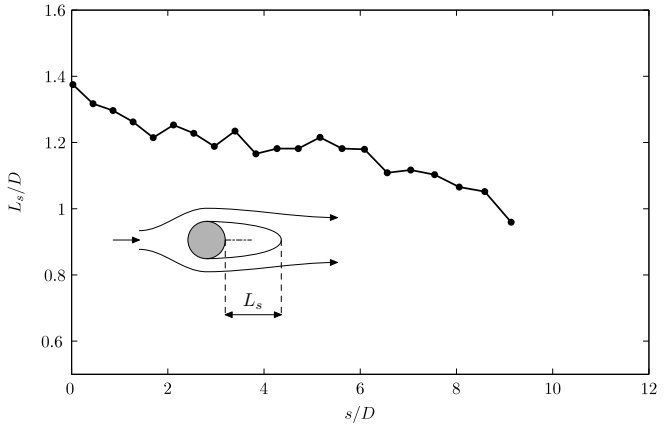

FIGURE 4.14: Recirculation length L_s along the span of the curved cylinder at $Re = 500$.

limitation, some important features of the recirculation length are identified. As seen in figure 4.14, L_s exhibits a monotonic decrease along the span, with its highest value equal to $1.375D$ at the top of the computational domain, i.e. $s/D = 0$. Although the lowest value of L_s is $0.96D$ at $x/D = 9.14$, the recirculation length is supposed to reach zero at some point in the interval $10 \leq s/D \leq 19.6$; for instance at $Re = 100$ the recirculation length attains a zero value at $s/D \approx 15$. It can be further noticed that the maximum value of L_s at 500 is lower than that at $Re = 100$, being the exact difference in terms of L_s equal to $0.2D$. Moreover, the L_s/D-s/D curve starts decreasing immediately from $s/D = 0$, instead of having a plateau as that exhibited in figure 4.14 at $Re = 100$.

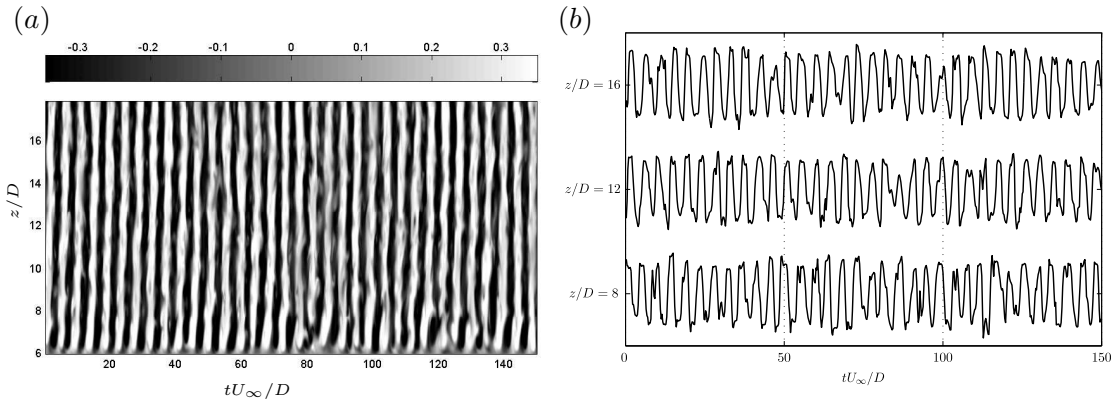

FIGURE 4.15: Time analysis of cross-stream velocity v at $Re = 500$ along a sampling line taken at $x/D = 18$ in the middle (x, z)-plane. (a) Time evolution of the velocity; (b) time trace of velocity.

4.2.2 Frequency analysis at $Re = 500$

In a similar way as in the case at $Re = 100$, the time evolution of the cross-stream velocity v has been evaluated within the (x, z)-plane of symmetry of the cylinder. The time evolution of this velocity component along a sampling line located at $x/D = 18$ is shown in figure 4.15(a); the pattern corresponds to strong alternating vortex shedding, which due to the higher Re_n, occurs along the whole sampling line in this case. Although a quasi–periodic pattern is clear in figure 4.15(a), some dislocations appear close to the horizontal extension between $z/D = 6$ and $z/D = 8$. The corresponding time-traces of the v-velocity are shown in figure 4.15(b) at three locations along the sampling line. The signals are characterized by a fairly periodic behaviour with similar amplitudes at the different vertical positions. Furthermore, the presence of interspersed distortions in the signal reveal the same characteristic features of the transitional and turbulent regimes in the wake of a straight cylinder (Karniadakis and Triantafyllou, 1992, Williamson, 1996a).

The spectral analysis with basis on the time-domain signals of the v-velocity was conducted with basis on a time–series of length $300D/U_c$, which covers about 67 shedding cycles at $Re = 500$. The analysis was performed under the same conditions defined for the case at $Re = 100$, and the spectra obtained at two different locations along the sampling line at $x/D = 18$ are shown in figure 4.16. In contrast with the spectra obtained at $Re = 100$, the spectra at $Re = 500$ exhibits wideband with the Strouhal frequency prevailing at a value of 0.2246. This shows again that despite the intermittent character of the flow observed in figure 4.15(b), a coherent vortex street pattern is still present

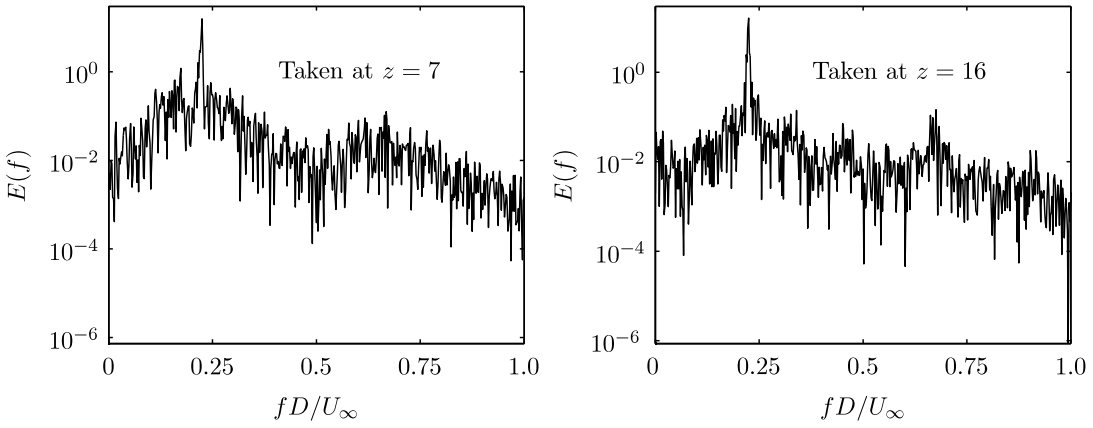

FIGURE 4.16: Power spectra of the v-velocity signal at $Re = 500$ taken at $x/D = 18$. (a) Spectrum at $z/D = 7$ and; (b) Spectrum at $z/D = 16$.

at one single shedding frequency along the span of the curved cylinder. The Strouhal frequency obtained from this analysis was compared with St for a straight circular cylinder at $Re = 500$, estimated from the St-Re relationship proposed by Williamson (1998) and expressed in equation (3.5). According to this relationship, the Strouhal frequency obtained for an uniform circular cylinder is 0.2243, which agrees remarkably well with $St = 0.2246$ for a curved cylinder at $Re = 500$.

4.2.3 Wake topology at $Re = 500$

A first impression of the three-dimensional vortical structures at $Re = 500$ is obtained using the λ_2–criterion. The iso–surfaces of $\lambda_2 = -1.5$ are able to educe the presence of instabilities in the form of streamwise vortical structures, as seen in the different views displayed in figure 4.17. This wake topology is similar to that observed by Miliou et al. (2007); the primary vortices are roughly aligned with the geometry of the curved cylinder, and the stretching of these primary vortices gives birth to streamwise vorticity. The projection on the (x, y)–plane, i.e. viewed from the top, highlight the shape and alternating pattern of these rib–like vortical structures associated with ω_x.

According to Williamson (1992), a fundamental mechanism in the transition to turbulence in the wake of a straight cylinder is the appearance of intermittent spanwise vortex dislocations. This feature has its origin in the differences in frequency of the spanwise vortex shedding cells, producing streamwise vorticity where the spanwise vortices split. This process is shown in figures 4.18(a) and (b). The instantaneous streamwise vorticity, represented by the black isosurfaces, appears at the locations where splitting of the

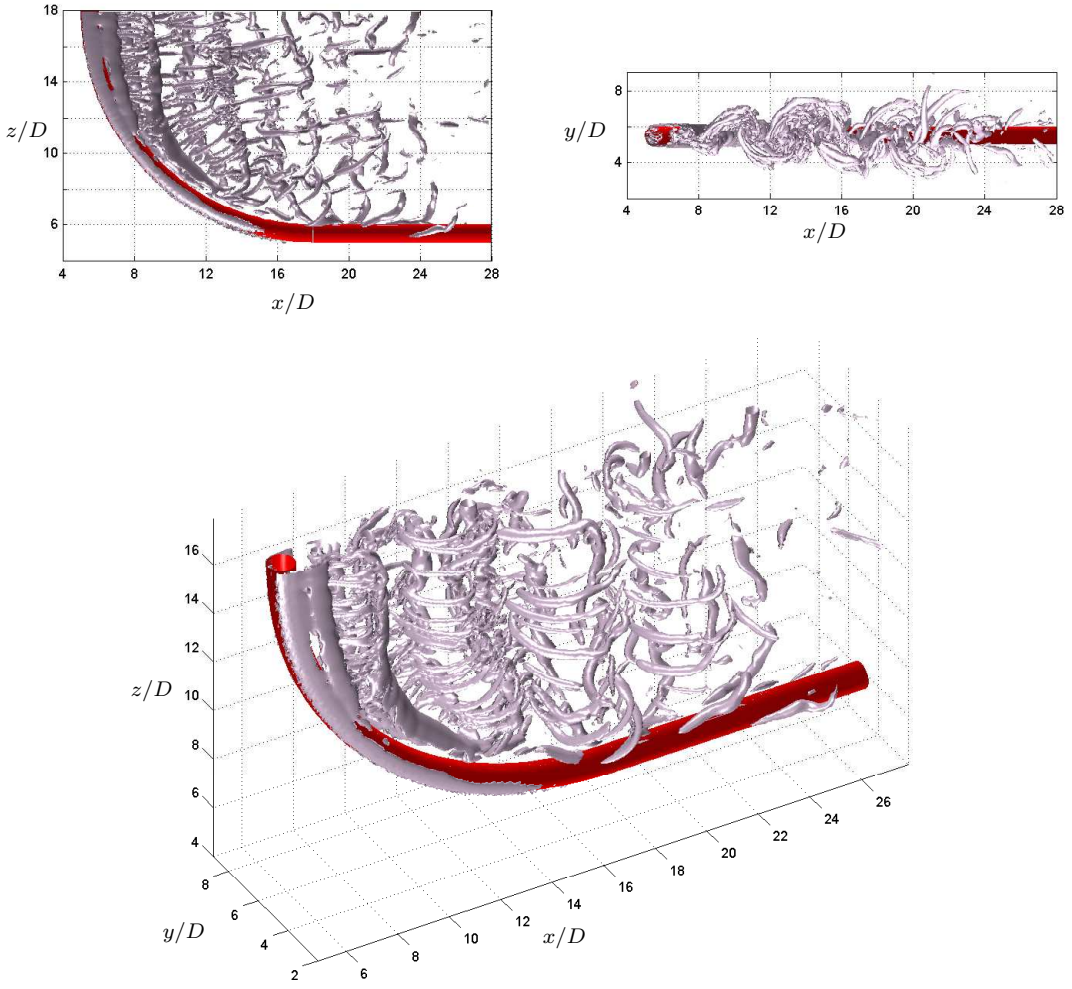

FIGURE 4.17: Wake topology at $Re = 500$ depicted as instantaneous iso–surfaces of λ_2. In the clockwise direction: side view, top view and perspective view of the vortex cores in the wake of the curved cylinder; here $\lambda_2 = -1.5$.

vertical vortices (white isosurfaces) occur. Another feature mentioned by Williamson (1992) is an helical twisting of the vortices, which is noticeable in the ω_z-isosurfaces in figure 4.18(b). Williamson concluded that these helical twisting are the fundamental cause for the rapid spanwise spreading of dislocations, and, indeed, for the large-scale distortion and break–up to turbulence in a natural transitional wake behind an uniform cylinder.

As figure 4.19(a) depicts, there is a rapid spreading of the streamwise vorticity as the wake evolves downstream. In the recirculation region, at $x/D = 7$ the streamwise vorticity is concentrated towards the axis of the cylinder. Then, at $x/D = 12$ two different patterns coexist in the same slice: on the upper part, the vorticity is concentrated only on one side, revealing the alternating pattern of ω_x after the vortices are shed; the lower portion, on the other hand, is still in the recirculating region and exhibits a behaviour

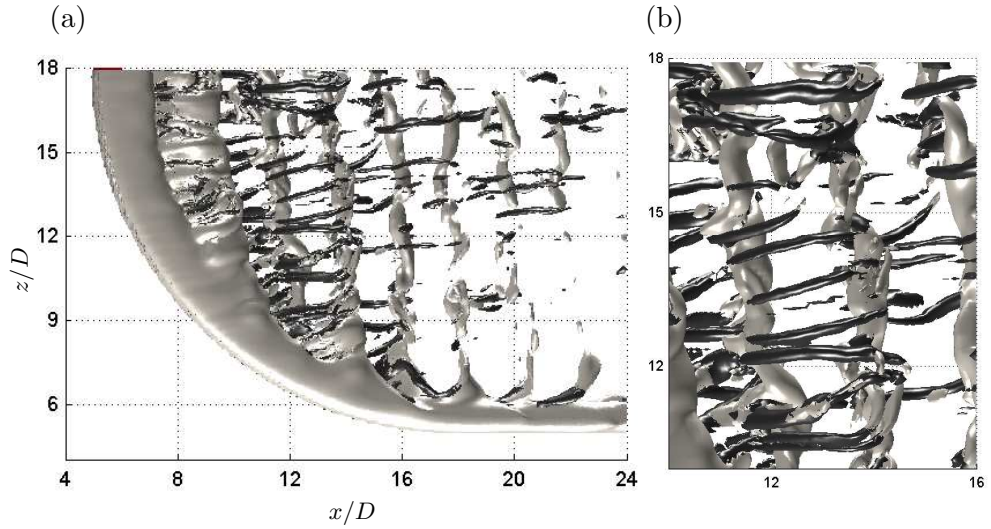

FIGURE 4.18: Isosurfaces of instantaneous vorticity ω_x (black) and ω_z (white) at $Re = 100$. The isosurfaces are obtained at $\omega_x, \omega_z = \pm 1.8$.

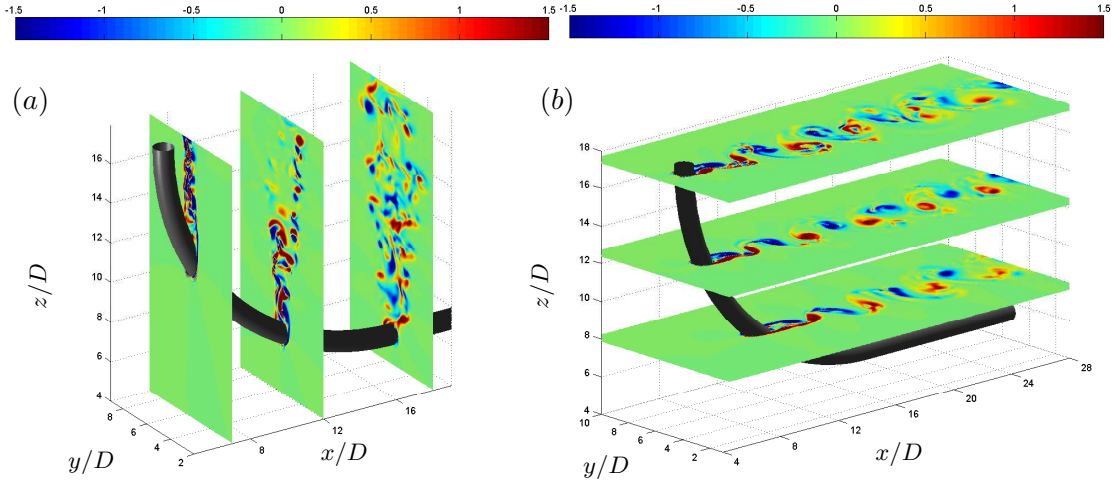

FIGURE 4.19: Isocontours of instantaneous vorticity at $Re = 500$. (a) ω_x in the (y, z)-planes at $x/D = 7$, 12 and 18; (b) ω_z in the (x, y)-planes at $z/D = 8$, 12.5 and 17.5.

similar to that shown at $x/D = 7$. Further downstream, at $x/D = 18$, a dispersed and irregular distribution of ω_x prevails. Moreover, the slices of ω_z clearly depict that vortex shedding takes place at all levels, supporting the observations based on the frequency analysis in section 4.2.2. Finally, and in analogy with the case at $Re = 100$, a displacement of the vortex formation region towards the rear stagnation line is evident by observing sequentially the slices at $z/D = 8$, 12.5 and 17.5.

4.3 Effects of a larger radius of curvature at $Re = 100$

In the first set of simulations, some physical mechanisms governing the dynamics of the flow past a curved cylinder have been analyzed in terms of the Reynolds number. Another non–dimensional quantity that may affect dynamics of the flow past a curved cylinder is the non–dimensional radius of curvature R/D. In order to analyze the influence of this parameter, a second set of simulations with $R/D = 25$ was conducted at $Re = 100$ with the flow configuration shown in figure 4.20. The dimensions of the grid in each direction are $N_x = 640$, $N_y = 160$ and $N_z = 400$, resulting in a total of 40.96×10^6 grid points. The minimum grid spacing is $\Delta x/D = 0.03$, $\Delta y/D = 0.02$ and $\Delta z/D = 0.06$ in the x-, y- and z–directions respectively. The number of processors for the domain decomposition was $n_{px} \times n_{py} = 20 \times 8$, i.e. a total of 160 processors. Other parameters such as the time–step and the temporal length for statistics were kept the same as in the previous cases presented.

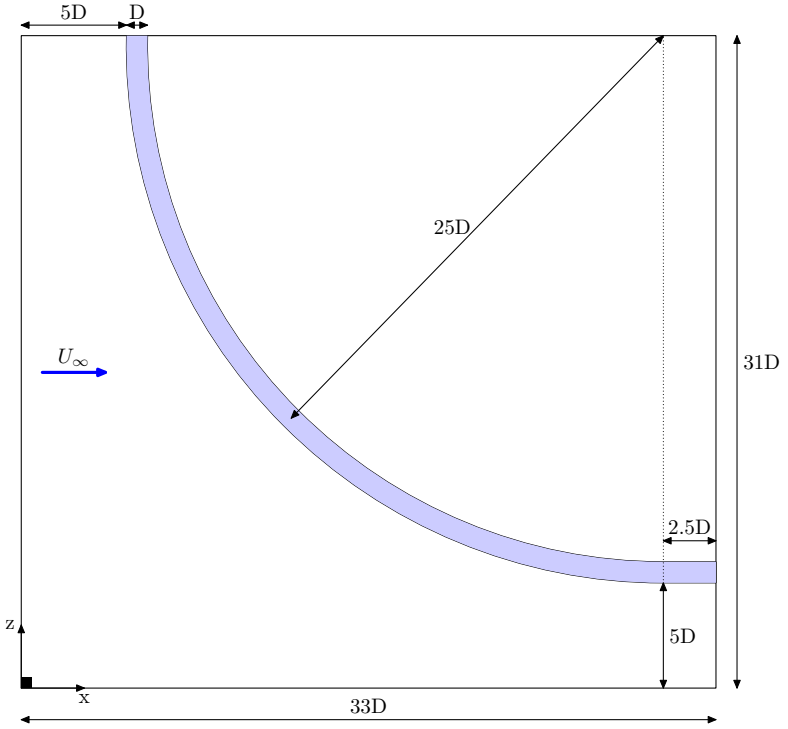

FIGURE 4.20: Computational domain size, geometry and flow configuration shown at the middle (x, z)-plane and at $R/D = 25$. The size of the computational domain is $33D$, $11D$ and $31D$ in the x-,y- and z-directions, respectively.

Begak et al. (1985) reported a variation of the Strouhal number with the radius of curvature, and proposed the following empirical relationship between these two parameters

$$St = 0.19 - \frac{1}{1.4R^3}, \tag{4.5}$$

where R is the radius of curvature. Using $R/D = 12.5$, the Strouhal frequency obtained from this expression is 0.1896, which is larger than St obtained from the frequency analysis in this work, and that reported by Miliou et al. (2007) as well. The range of validity in terms of R/D for equation (4.5) is not given by the authors, however.

In order to determine if there is any variation in the Strouhal frequency when R/D is changed, a frequency analysis similar to that presented in sections 4.1 and 4.2 (i.e. based on the time-domain signals of the v-velocity) was conducted. The spectra obtained at four different vertical locations along a sampling line at $x/D = 25$ are shown in figure 4.21. The characteristics of the spectra are identical to those exhibited when $R/D = 12.5$ at a Reynolds number of 100, and the Strouhal frequency surprisingly remained the same ($St = 0.1758$). Although this is in contrast with the observations by Begak et al. (1985), further investigation with other radii of curvature is required in order to be conclusive.

Another feature which is interesting to note from the spectral analysis is the amplification of the odd harmonics, which are exhibited in all the spectra except the spectrum taken at $z/D = 8$. Particularly interesting is the spectrum shown in figure 4.21(c) at $z/D = 24$, which besides the secondary peak at $3St$ contains a small peak at $5St$.

Finally, the vortical structures depicted as iso–surfaces of $\lambda_2 = -0.1$ are shown in figure 4.22. Despite differences in geometry, the vortex cores are similar to those obtained at a non–dimensional radius of curvature of 12.5. This complements the frequency analysis in the sense that, at least at this Reynolds number, increasing the radius of curvature does not affect the wake dynamics. Further work has to be conducted in order to explain these facts, however.

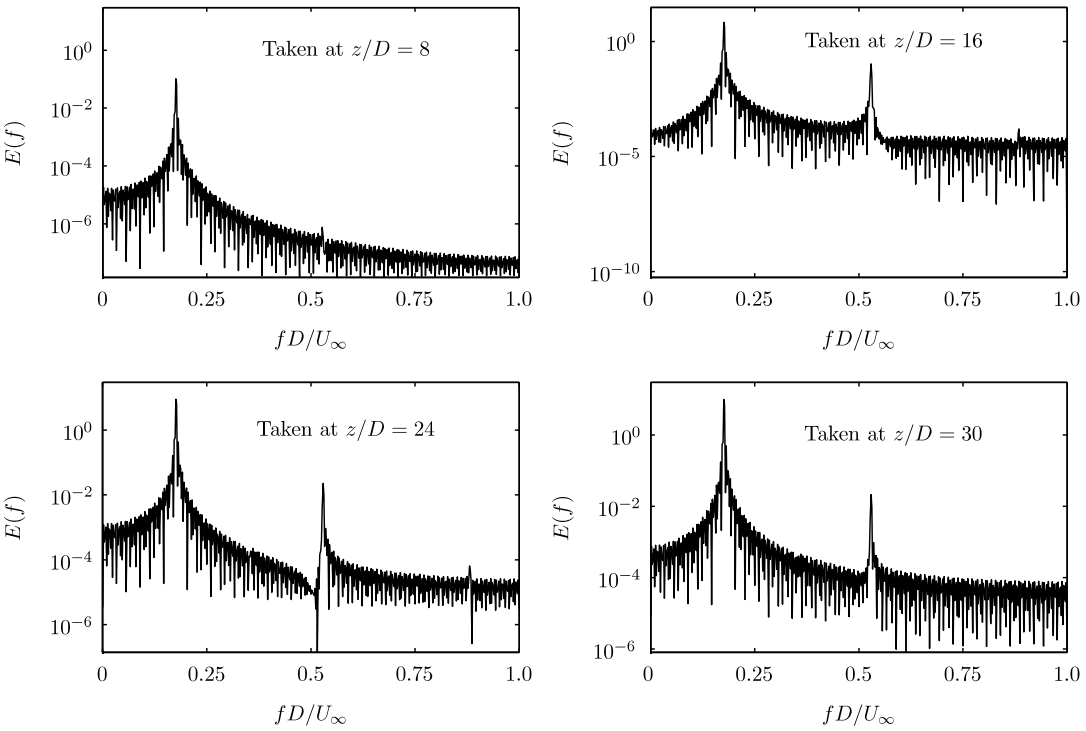

FIGURE 4.21: Power spectra of the v-velocity signal at $Re = 100$ and $R/D = 25$; signal taken at $x/D = 25$. (a) Spectrum at $z/D = 8$; (b) Spectrum at $z/D = 16$; (b) Spectrum at $z/D = 24$ and; (b) Spectrum at $z/D = 30$.

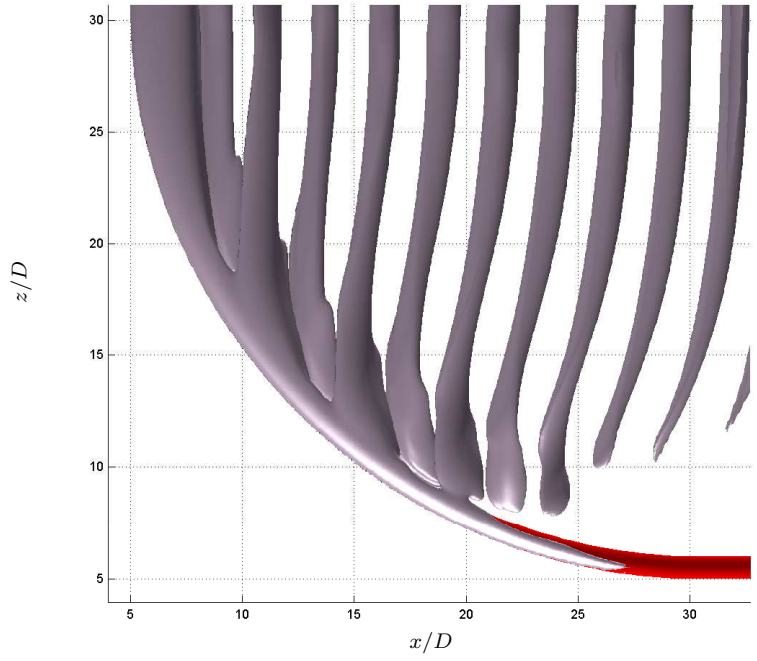

FIGURE 4.22: Wake topology at $Re = 500$ and $R/D = 25$ depicted as instantaneous iso–surfaces of λ_2. Here $\lambda_2 = -0.1$.

Chapter 5

Results and Discussion: Shear Flow

In addition to the effects of non–uniform geometry, three–dimensionalities in the wake of bluff bodies are also enhanced by imposing a non-uniform velocity profile in the free–stream. As discussed in section 1.4, features like oblique and cellular vortex shedding are found in the wake of the flow past straight cylinders in uniform shear. Although no cellular arrangement of the vortex shedding frequencies was detected as a consequence of the curved geometry, the presence of a sheared flow may disrupt the vortex shedding pattern in a curved cylinder, leading thus to the same types of phenomena as those observed in the flow past straight cylinders in uniform shear. Therefore the interaction between curved cylinders and shear flows, whose understanding is important in the design of marine structures, will be addressed in this chapter.

With the exception of the inlet boundary condition, the flow configuration used here is the same as that used in the previous analysis with uniform inflow, as figure 5.1 depicts. The linearly varying velocity profile prescribed at the inlet can be expressed mathematically as

$$\frac{U_\infty(z)}{U_c} = \frac{Kz}{D} + \frac{U_0}{U_c}, \tag{5.1}$$

where the non-dimensional inlet shear rate K was set to 0.1. Here, $K = (dU_\infty/dz)D/U_c$, with dU_∞/dz defined as the inflow shear rate, U_c is the inflow velocity at the mid height (or average of the inflow velocity in the z–direction), and U_0 is the inflow velocity at

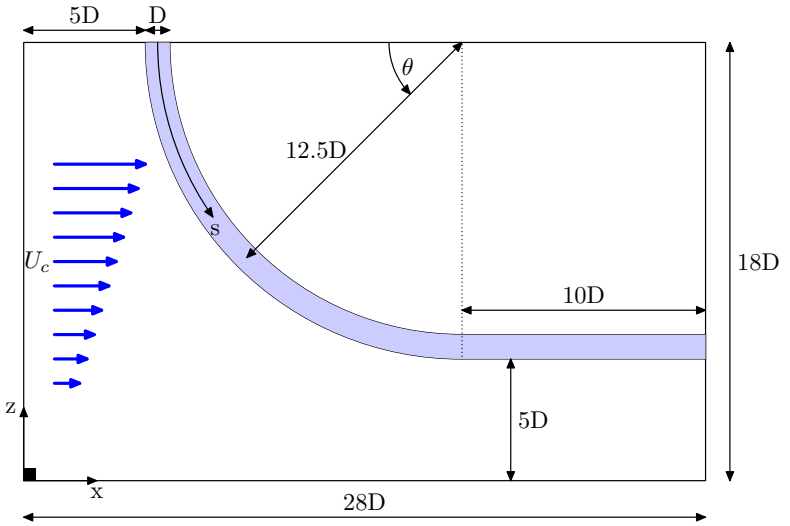

FIGURE 5.1: Flow configuration considering shear flow at the inlet. Computational domain size, geometry and flow configuration shown at the middle (x, z)-plane. The inflow velocity varies linearly in the z-direction, with an average value U_c at the mid height of the computational domain.

the bottom plane ($z = 0$). In most of the normalizations, the velocity U_c will be used instead of the non–uniform velocity $U_\infty(z)$. Two cases at Reynolds 100 and 500 were studied with this shear rate; the Reynolds number here is defined as $Re = U_c D/\nu$. In this context, we also define the local Reynolds based on the shear velocity profile as $Re_l(z) = U_\infty(z)D/\nu$.

5.1 Effects of the shear flow in the near wake

The variation of the mean pressure along the stagnation lines, this time normalized by the dynamic pressure $1/2\rho U_c^2$, is shown in figure 5.2 at $Re = 100$ and 500. The variation of the C_p along the front stagnation line is identical at both Reynolds numbers, and besides, they are substantially steeper than the curves of C_p in uniform flow, presented in section 4.1 (see figures 4.2 and 4.11). This is a clear example of the combined effect of curvature and a linearly varying velocity profile; both conditions induce separately a negative pressure gradient along the span ($\partial C_p/\partial s < 0$), that results in a large rate of change of C_p from the combined effect. Moreover, the decreasing of C_p remains monotonic.

On the rear stagnation line, a region of almost zero mean pressure gradient is exhibited at $Re = 100$ and 500 on the top part of the curved cylinder (i.e. low values of s/D). At $Re = 100$, as figure 5.2(a) depicts, this plateau extends up to $s/D \approx 4$, where a positive

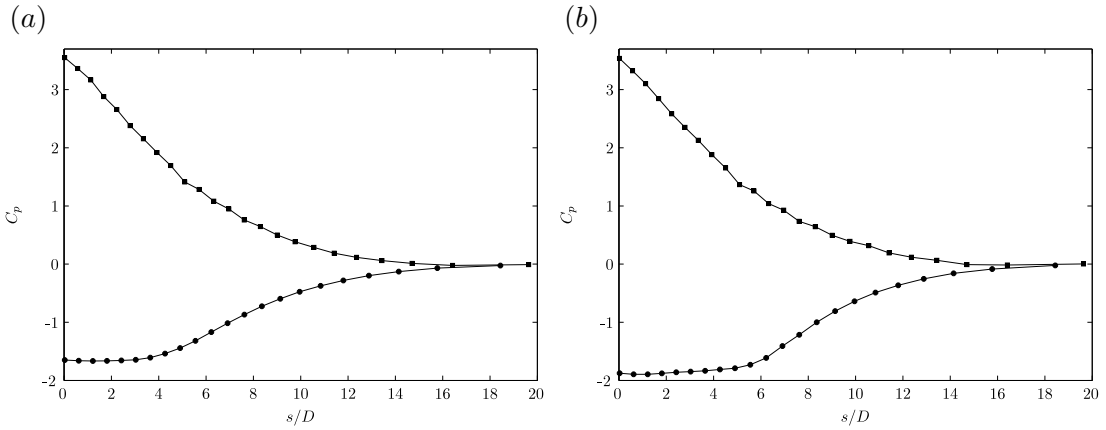

FIGURE 5.2: Mean pressure coefficients C_p along the span of the curved cylinder at $Re = 100$ and 500 in uniform shear. Here —■—, stagnation pressure coefficient; —●—, base pressure coefficient. (a) $Re = 100$ and; (a) $Re = 500$.

pressure gradient builds-up afterwards. At $Re = 500$, on the other hand, the plateau extends further down along the span to $s/D \approx 5$ before the gradient increases (see figure 5.2.b). Regions of constant base pressure coefficient were previously reported by Maull and Young (1973) for a straight cylinder in uniform shear. Regarding the cellular vortex shedding pattern detected in this experimental work, the flat regions of C_p along the base line occurred at the division between cells of constant frequency; within each constant frequency cell the base pressure varied.

The axial flow developed along the front stagnation line, attributed to the favourable pressure gradient $\partial C_p/\partial s < 0$, does not differ much from that obtained in uniform flow, as the streamlines in figure 5.3 depicts. The mean streamlines in the recirculating region, on the other hand, clearly differ from those obtained with uniform flow at the inlet. The recirculating streamlines in the vicinity of the upper part of the curved cylinder have a positive component of the mean velocity in the z–direction, giving the impression that they are drawn from their original position towards the upper plane. This behaviour may be associated with the region of sustained base pressure observed in figure 5.2, which drives the recirculating streamlines upwards. Furthermore, in figure 5.3(a) the upheaving of the streamlines seems to be stronger than that depicted by figure 5.3(b). An explanation to this difference is that at $Re = 500$, the base suction that attracts the streamlines has to compete with the mixing and dissipation levels expected at this Reynolds number, while at $Re = 100$ the flow regime remains laminar.

In order to support the observations above, streamlines obtained from the instantaneous flow field are shown in figures 5.4. While some streamlines pass the body and continue in

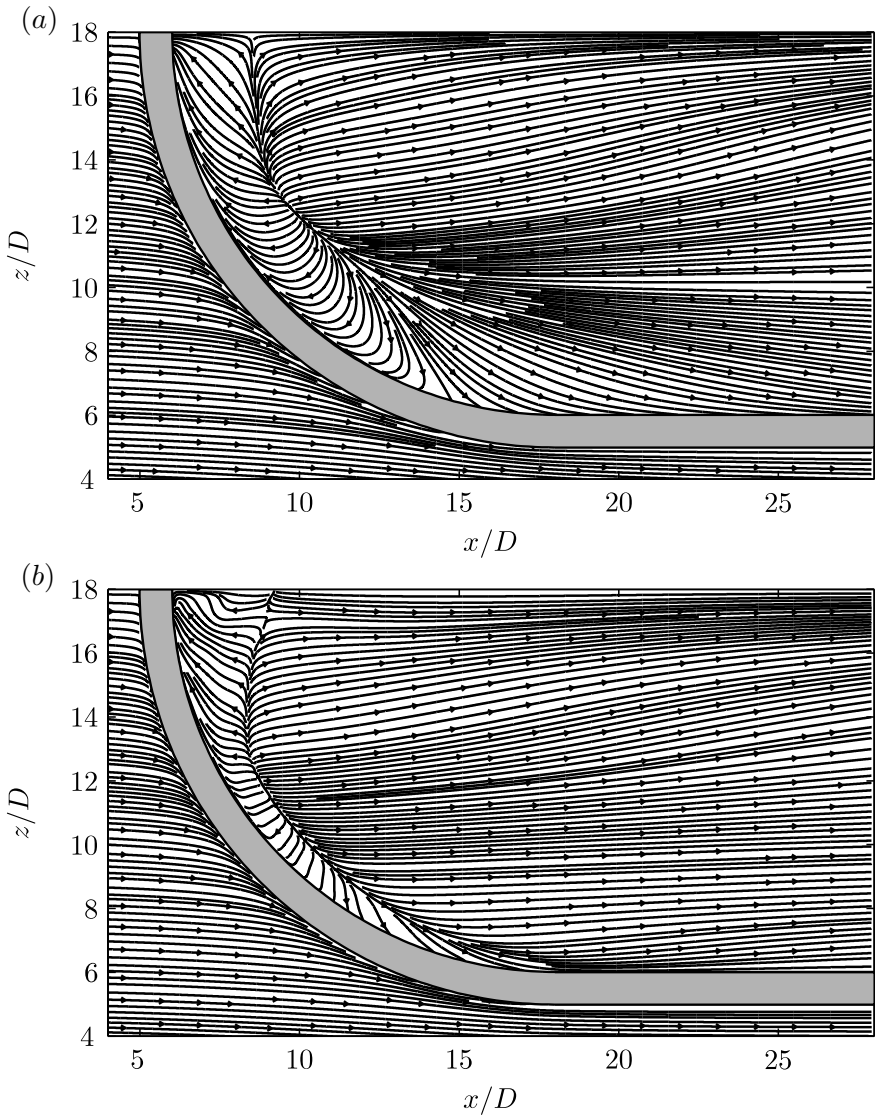

FIGURE 5.3: Streamlines of the mean flow taken at the middle (x, z)-plane at $Re = 100$ and 500 in uniform shear. (a) $Re = 100$ and; (b) $Re = 500$.

the direction of the main flow, as seen in figures 5.4(b) and (d), part of the recirculating streamlines exhibit an helical motion in the positive z–direction. It can be further noticed that although the pattern of recirculation at $Re = 100$ depicted by figure 5.4(a) is more regular than that at $Re = 500$, the presence of two groups of streamlines recirculating in opposite directions[1] at the same time indicates that cellular vortex shedding is occurring. Each of the two groups are shed with a phase difference in this case. In figures 5.4(c) and (d) the streamlines exhibit a tangled form, which is related to the increasing disorder in the fine scale structures due to higher local Reynolds numbers. Despite this spatial complexity, the typical structure of the three-dimensional vortex shedding remains.

[1] Although these two regions can be identified as vortices, Jeong and Hussain (1995) showed that streamlines do not provide an absolute criterion to identify a vortex.

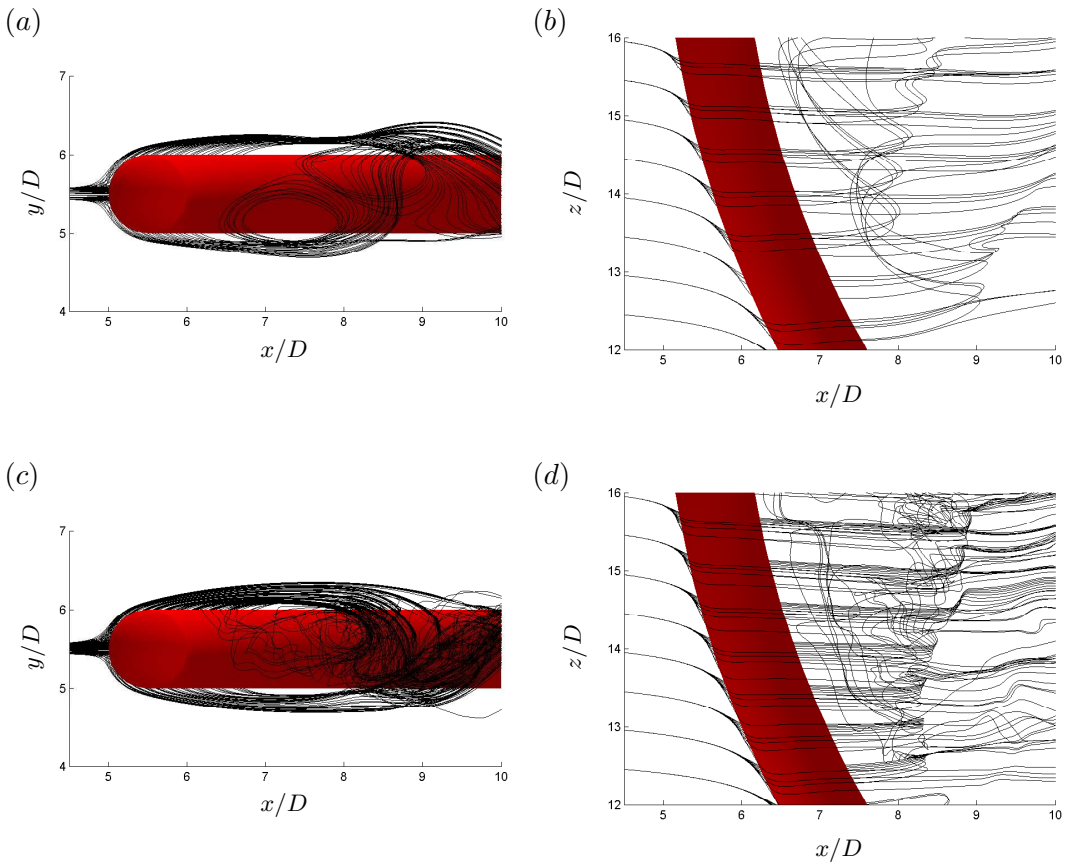

FIGURE 5.4: Instantaneous streamlines at $Re = 100$ and 500, and $K = 0.1$; close view of the recirculation region. (a) Projection in the (x, y)–plane at $Re = 100$; (b) projection in the (x, z)–plane at $Re = 100$; (c) Projection in the (x, y)–plane at $Re = 500$ and; (b) projection in the (x, z)–plane at $Re = 500$.

Finally, the non–dimensional local separation length L_s/D is plotted along the span of the curved cylinder in figure 5.5. The variation of L_s at $Re = 100$ in the presence of shear is fairly similar to that observed in the uniform flow case (see figure 4.5), but instead of being almost constant between the non–dimensional spanwise locations 0 and 8, it exhibits a local minimum at $s/D \approx 5$. Such behaviour along the first part of the span has its origin in the pressure coefficient distribution shown in figure 5.2(a). Moreover, at $Re = 100$ the recirculation length for the shear flow case ($K = 0.1$) is larger than that for the uniform flow case at all the spanwise locations; in this case the maximum value of L_s is $2.475D$, and it becomes zero at $s/D = 16.41$. At a Reynolds number of 500, the local separation length at the top plane for uniform shear is twice as that for uniform flow; here the maximum value of L_s/D is 3.175 at the top plane, reaching zero at $s/D = 12.33$. Furthermore, the shape of the recirculation region is substantially affected by the shear induced motion; the curve in figure 5.5 exhibits a

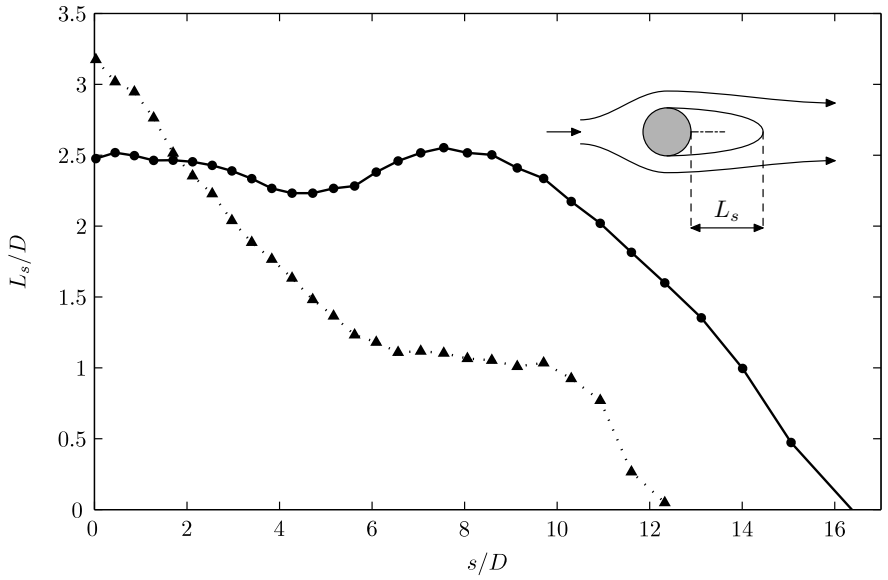

FIGURE 5.5: Recirculation length L_s along the span of the curved cylinder at $Re = 100$ and 500 in uniform shear: —●— at $Re = 100$ and ; ···▲··· at $Re = 100$.

steep slope up to $s/D = 6$, then L_s/D is relatively constant before it drops to zero in the interval $s/D = 10$–12. On both cases, $Re = 100$ and 500, uniform shear creates longer separation length which is coupled with higher base pressure for $s/D < 5$.

5.2 Cellular vortex shedding

Vortices shed at different frequencies characterize the flow past a circular cylinder in the presence of uniform shear. The arrangement of the streamlines shown in figure 5.4(a) gave an indication that, at least for $Re = 100$, a cellular pattern of the vortex shedding is occurring. In order to validate this observation, a frequency analysis of the time evolution of the cross-stream velocity v, evaluated within the (x, z)-plane of symmetry, has been carried out. As in the previous cases, the total simulated time was $300D/U_c$, which covers about 73 shedding cycles (taken at the mid height, i.e $z/D = 9$) at $Re = 100$ and 500.

Figure 5.6 contains the plots of the time evolution and time traces of the v-velocity component taken along a sampling line located at $x/D = 18$ for the two Re under investigation. At $Re = 100$, periodic dislocations in the time evolution of v can be identified in the upper part of the domain, as figure 5.6(a) depicts; this supports the observation that vortices are shed at different frequencies, based on the streamlines plot

in section 5.1. These dislocations arise at a local Reynolds number of 167 ($z/D = 15.7$), which is lower than the critical Reynolds number range ($Re = 180$–194) for the mode A instability described by Williamson (1996b). The discontinuities in the vortex shedding frequency are therefore attributed to the shear rate imposed ($K = 0.1$). The time traces of the v-velocity signals at four different vertical positions shown in figure 5.6(b) clearly differ from those corresponding to uniform inflow. The behaviour in this case is quasi–periodic, with the suppression of vortex shedding occurring around $z/D \approx 10$, where the signal almost dissappear. The periodic dislocations shown in figure 5.6(a) are due to the splitting of the Kármán vortices as they are shed from the upper segment of the curved cylinder. This splitting, for instance, can be identified in the periodic distortions arising in the v-velocity trace at $z/D = 16$, and in the low frequency modulation at $z/D = 14$; both features are characteristic of dislocations between cells in uniform cylinders (Williamson, 1992). The period of the dislocations is five shedding cycles.

The time evolution of the v-velocity obtained at $Re = 500$ is shown in figure 5.6(c). Here the signal is less synchronized and characterized by non-periodic occurrence of vortex dislocations or vortex splits along the span. The corresponding time-traces of the v-velocity are shown in figure 5.6(d). It was previously stated in section 4.2 that, even though at $Re = 500$ in uniform flow the signals are distorted, they exhibit a fairly periodic behaviour with similar amplitudes at different vertical positions. This is not the case in the presence of shear, as seen figure 5.6(d), because noticeable differences exist between the amplitude and frequency of the time-traces at the lower position at $z/D = 10$, and those at the upper positions at $z/D = 14$, 16 and 18. Additionally, the time-traces become less periodic as compared to the uniform flow case. Despite the random fluctuations due to turbulence, a low frequency modulation is still visible in certain signals.

In figure 5.7, we can also compare the power spectra of the v–velocity signal at two different positions along the sampling line. The spectrum taken at $z/D = 12$ and $Re = 100$ (figure 5.7.a) do not differ much from the spectrum obtained when the flow is uniform at this Re. The peak corresponds to the dominant Strouhal frequency, and most of the energy in the spectrum is concentrated around this point, with the peak differing by a factor of $\approx 10^4$ from the spectral densities at other frequencies. At $z/D = 17$ (figure 5.7.b), the spectrum exhibits a higher dominant shedding frequency together with a increase in the energy level, this is evidently due to the higher local Reynolds

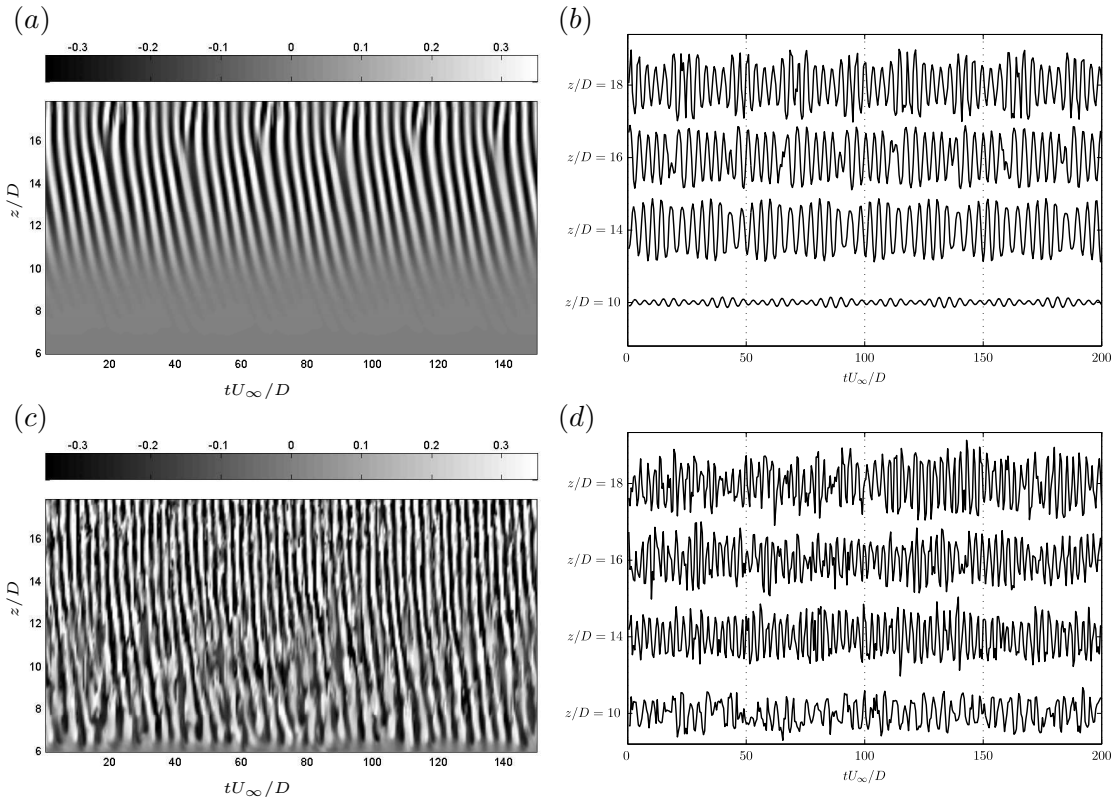

FIGURE 5.6: Time analysis of cross-stream velocity v at $Re = 100$ and 500 in uniform shear; sampling line taken at $x/D = 18$ in the middle (x, z)–plane. (a) Time evolution of the velocity at $Re = 100$; (b) time trace of velocity at $Re = 100$; (c) Time evolution of the velocity at $Re = 500$ and; (d) time trace of velocity at $Re = 500$.

number Re_l. The spectral densities at $Re = 500$ become substantially more wideband; this is especially evident at $z/D = 9$ (figure 5.7.c), where the peak in the spectrum at $fD/U_c = 0.244$ differs only by a factor of ≈ 100 from the lower spectral densities. The peak at $z/D = 17$ occurs at a higher frequency ($fD/U_c = 0.367$), as seen in figure 5.7(d), and although the spectrum also possesses wideband, this peak is easily distinguished from the other lower spectral densities.

The cellular pattern of the vortex shedding is even more clear in figure 5.8, where the dominant shedding frequencies normalized by both, local $U_\infty(z)$ and mid height U_c velocities, are plotted versus the local Reynolds numbers Re_l. The *St-Re* curve at $Re = 100$ (figure 5.8.a) exhibits two frequency cells at $fD/U_c = 0.240$ and 0.283, the length of these cells are $5.63D$ and $2.37D$ respectively; here the dislocation occurs at $Re_l = 167$ ($z/D = 15.7$). When the Reynolds number is increased to 500, on the other hand, the *St-Re* curve exhibits four frequency cells at $fD/U_c = 0.152$, 0.176, 0.244 and 0.367; with dislocations occurring at $Re_l = 361$, 384 and 575, as seen in figure 5.8(b). The length of these cells is $0.17D$, $0.40D$, $3.71D$ and $7.35D$. It can be further

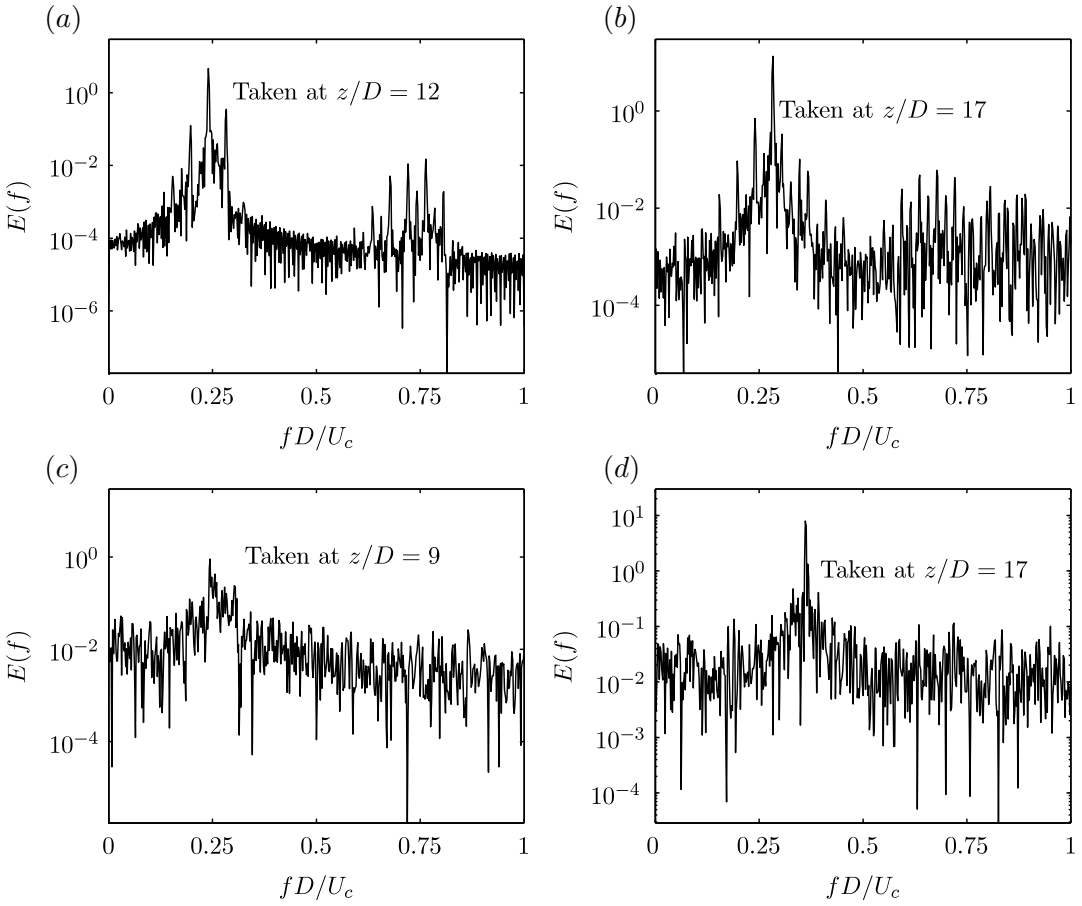

FIGURE 5.7: Power spectra of the v-velocity signal at $Re = 100$ and 500 in uniform shear; signal taken at $x/D = 18$. (a) Spectrum at $z/D = 12$ and $Re = 100$; (b) Spectrum at $z/D = 17$ and $Re = 100$; (c) Spectrum at $z/D = 9$ and $Re = 500$ and; (d) Spectrum at $z/D = 17$.

noticed that below $z/D = 10$ at $Re = 100$, the vortex shedding is suppressed despite the fact that $Re_l = 110$ (based on the local inflow velocity only), this is evidently due to the interaction between shear flow and curvature effects. This interaction also occurs at $Re = 500$, but since the local Reynolds numbers are higher, it is more difficult to become aware of the combined effect between curvature and shear flow from the visual inspection of figure 5.8(b).

5.3 Influence of the shear rate on the wake topology

Previous studies of uniform shear flow past a straight cylinder have reported obliqueness of the vortical structures, see for instance the work by Mair and Stansby (1975), Mukhopadhyay et al. (2002), Silvestrini and Lamballais (2004). This is due to the fact that the vortices are transported downstream at different velocities as they are shed from

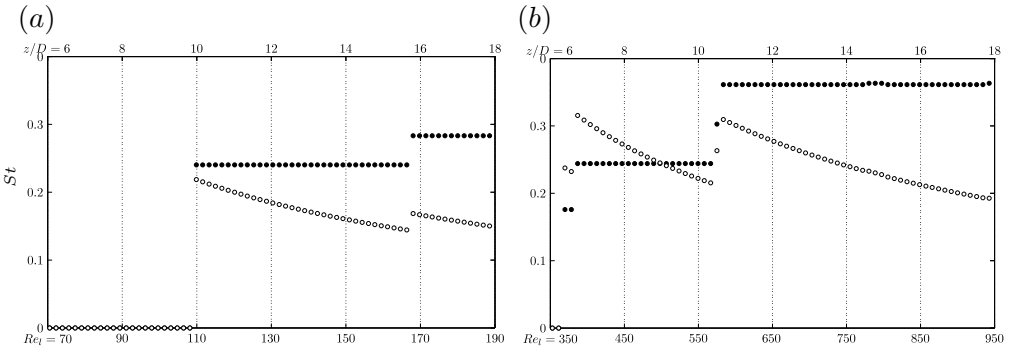

FIGURE 5.8: Strouhal frequencies along a sampling line taken at $x/D = 18$ in the middle (x, z)–plane. Shear flow cases, ○, St computed with the local inflow velocity U_∞; ●, St computed with U_c. (a) $Re = 100$ and; (b) $Re = 500$.

the cylinder. This phenomenon was also detected on the flow past a curved cylinder at $K = 0.1$, as seen in figure 5.9. Here the two cases analyzed in uniform shear ($Re = 100$ and 500) exhibit a rather high degree of obliqueness in their vortical structures.

The vortex cores at $Re = 100$ shown in figures 5.9(a) and (b) exhibit two distinct behaviours related to the presence of uniform shear at the inlet. Close to the top of the computational domain, where the highest local velocities of the free-stream occur, the iso–surfaces of λ_2 are associated to streamwise vorticity (ω_x). This component arises from two sources, one of them is the local Reynolds number range ($Re_l = 180$–190), and the other is the horseshoe vortex that form due to the bending of the vorticity contained in the shear flow (ω_y) when it encounters the cylinder (see section 1.4). The presence of ω_x leads to instabilities and the periodic splitting of the primary vortices (or dislocations) discussed previously in the frequency analysis. Below the upper part of the cylinder, the vortex cores becomes increasingly slanted as they are transported further downstream. Previous studies of the cellular pattern of the vortex shedding and the obliqueness of the vortices in the presence of shear consider a straight cylindrical geometry (Kappler et al., 2005, Mair and Stansby, 1975, Mukhopadhyay et al., 2002, Silvestrini and Lamballais, 2004, Woo et al., 1989), hence, further studies with different shear rates are relevant for the understanding of the interaction between shear flow and curved cylinders. For the uniform flow case at $Re = 100$, for instance, the streamwise vorticity arises as an effect of curvature (see figure 4.9); the streamwise vorticity induced by different shear rates may have either an adverse or favourable effect when interacting with the streamwise vorticity due to curvature, changing thus the wake dynamics.

Besides the increasing obliqueness in the downstream direction, the shear flow case at

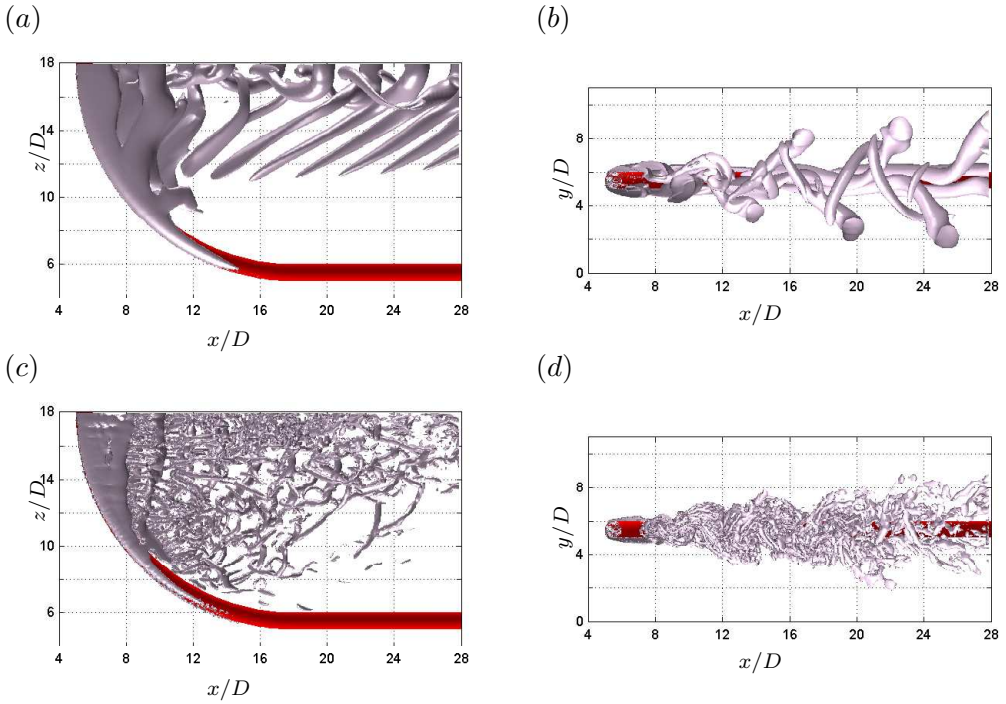

FIGURE 5.9: Wake topology depicted as instantaneous iso–surfaces of λ_2 for the cases in uniform shear. (a) Projection in the (x, z)–plane at $Re = 100$ and $\lambda_2 = -0.2$; (b) projection in the (x, y)–plane at $Re = 100$ and $\lambda_2 = -0.2$; (c) projection in the (x, z)–plane at $Re = 500$ and $\lambda_2 = -2.5$ and; (d) projection in the (x, y)–plane at $Re = 500$ and $\lambda_2 = -2.5$.

$Re = 500$ exhibits vortical structures of a much finer–scale compared to the uniform flow case. As seen in figure 5.9(c), these fine–scale structures are produced on the upper portion of the domain ($z/D = 14$–18) due to the higher local Reynolds number. Below $z/D = 10$, the structures associated with streamwise vorticity appears at the locations where the primary vortices split.

The instantaneous streamwise vorticity components ω_x and ω_z at $Re = 100$ were plotted in three consecutive planes in figure 5.10. The instantaneous streamwise vorticity in the (y, z)–planes shown in figure 5.10(a) give a clear picture of the evolution of ω_x in the x–direction. The plane at $x/D = 7$ is located well within the recirculation region in the upper portion of the cylinder, here we observe two parallel layers of ω_x with opposite sign corresponding to the bended vortex filaments of ω_y in the shear flow. The plane at $x/D = 12$ exhibits a similar pattern at the lower part of the curved cylinder, but the layers of ω_x here have different sign than those at $x/D = 7$; on the upper half of this plane negative values of ω_x prevail. At $x/D = 18$ the streamwise vorticity is split into several regions of counter rotating vorticity. Regarding the vertical vorticity component, figure 5.10(b) depicts the pattern for ω_z on three consecutive (x, y)-planes.

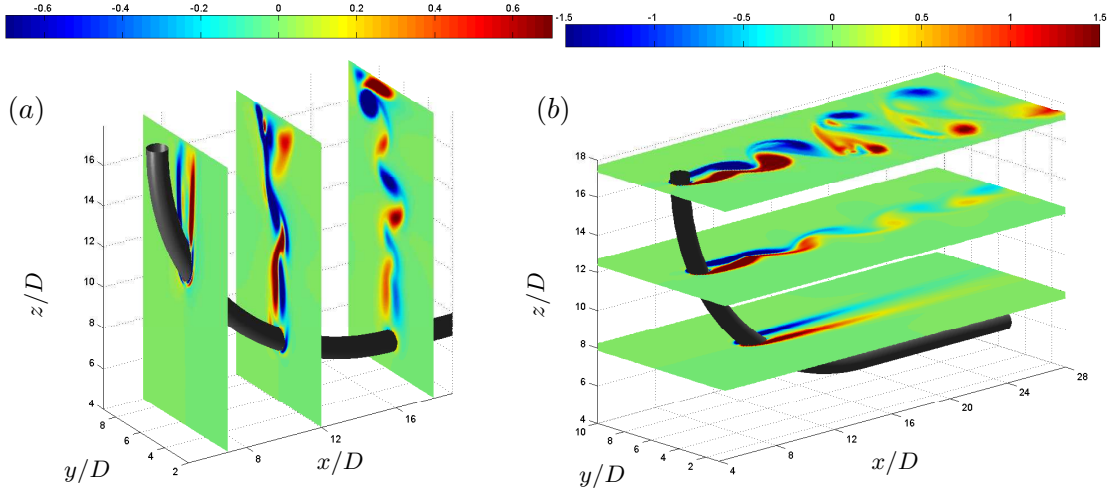

FIGURE 5.10: Isocontours of instantaneous vorticity at $Re = 100$ in uniform shear. (a) ω_x in the (y, z)-planes at $x/D = 7$, 12 and 18; (b) ω_z in the (x, y)-planes at $z/D = 8$, 12.5 and 17.5.

Since the vortex shedding starts above $z/D = 10$, only two regions of ω_z appear at $z/D = 8$, here the flow could be regarded as locally stationary. At $z/D = 12.5$, where the local Reynolds number is 135, a clear pattern of vortex shedding is represented by the isocontours of ω_z. Close to the top of the domain at $z/D = 17.5$ the pattern of ω_z is more irregular than that at $z/D = 12.5$, the ω_z–cores are spread, covering a larger area at this vertical location. Here $Re_l = 185$, i.e. within the range at which the mode A instability occurs (Williamson, 1988), thus the wake instabilities will be amplified as they are transported further downstream.

Finally, the same analysis based on the vorticity components was performed at $Re = 500$. In figure 5.11(a), the (y, z)-plane at $x/D = 7$ exhibits lower magnitudes of streamwise vorticity in the recirculation zone as compared to the planes at $z/D = 12$ and 18, where the wake has evolved. The two thin layers of ω_x correspond to the horseshoe vortices discussed above. This increase of ω_x is not surprising since this case possesses three sources of ω_x, namely the curvature of the cylinder, the wake instabilities due to the turbulent regime, and the shear rate imposed. As for the vertical component of the vorticity ω_z, figure 5.11(a) shows at the upper plane ($z/D = 17.5$) a stretching of the vertical vorticity in the downstream direction close to the recirculation zone, presenting a rather diffusive pattern as it continues downstream. The lower planes at $z/D = 12.5$ and 8 exhibit a characteristic vortex shedding pattern with some irregularities associated to $Re = 500$.

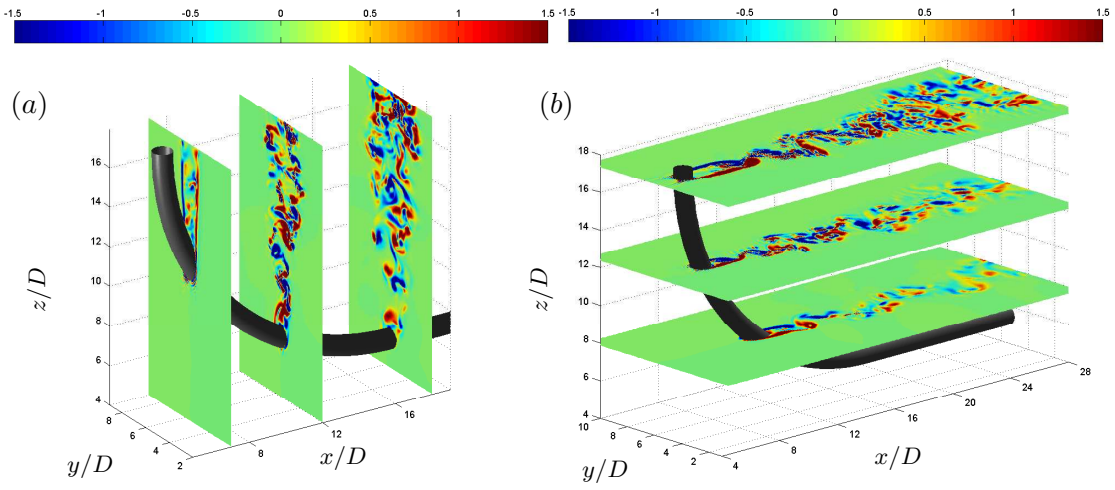

FIGURE 5.11: Isocontours of instantaneous vorticity at $Re = 500$ in uniform shear. (a) ω_x in the (y, z)-planes at $x/D = 7$, 12 and 18; (b) ω_z in the (x, y)-planes at $z/D = 8$, 12.5 and 17.5.

Chapter 6

Conclusions

This work presents a series of numerical simulations of the flow past a curved circular cylinder at Reynolds numbers of 100 and 500. The bluff body geometry was composed of a quarter segment of a ring, and a horizontal extension between the end of the bend and the outflow plane. The free-stream was parallel to the plane of curvature of the deformed cylinder, and directed towards the outside region of the quarter-or-ring; this was the so-called convex configuration. In the first set of simulations, a radius of curvature of $12.5D$ was selected in order to enable comparison with the previous published study of Miliou et al. (2007). In a second stage, the effects of increasing the radius of curvature to $25D$ and the influence of a sheared inflow were also investigated. In general terms, the results obtained were in excellent agreement with those published by Miliou et al. (2007). In addition, a combination of shear flow and curvature effects that led to oblique and cellular vortex shedding was shown to occur for this convex configuration. Regarding the DNS code MGLET used for the computations, the performance of the IBM method was very promising when performing the simulations using this curved cylinder geometry embedded in a Cartesian mesh.

The analysis of the mean pressure coefficients along the front and rear stagnation lines revealed some characteristic features associated to the curvature of the cylinder, that were previously reported by Miliou et al. (2007). In uniform flow, a negative pressure gradient occurred along the front stagnation line at $Re = 100$ and 500. This pressure variation induced the development of a significant axial flow aligned to the leading edge of the curved cylinder. In the presence of shear, on the other hand, the pressure

gradient along the front stagnation line was larger on the upper part of the cylinder, due to the higher variation of the local velocities that resulted from the combination of shear and curvature. Also in the shear flow cases, the mean pressure coefficient along the rear stagnation line (or base line) exhibited a region of almost zero pressure gradient on the upper part of the cylinder. This clearly affected the distribution of velocities in the recirculation zone and the size of the recirculation bubble. Additionally, the Independence Principle was shown to be valid for the pressure coefficients along the stagnation lines up to an angle of 45° measured from the top plane. This was in good agreement with the observations by Zhao et al. (2009) for a yawed cylinder.

The frequency of the vortex shedding, obtained from a spectral analysis of the temporal evolution of cross-stream velocities, was an important parameter for comparison between the different cases. When the flow was uniform the vortices were shed at one single frequency along the span of the cylinder. This behaviour was previously reported by Begak et al. (1985) and Miliou et al. (2007). Additionally, when at $Re = 100$ the radius of curvature was increased from $12.5D$ to $25D$, the Strouhal frequency remained the same ($St = 0.1758$). This is in contrast with the observations by Begak et al. (1985), who proposed a relationship for the variation of the Strouhal frequency with the radius of curvature. Further work will help to elucidate this discrepancy. It was also noticed that the domain size may influence the Strouhal frequencies at some degree. A difference of 3.4% was estimated when the domain was increased in $5D$ between the inlet plane and the cylinder, and $10D$ in the horizontal y-direction, independently. Furthermore, the Strouhal frequency obtained at $Re = 100$ is higher than that corresponding to a straight cylinder at the same Re, whereas at $Re = 500$ the Strouhal frequency for curved and straight cylinders were the same.

A distinct vortex shedding pattern was observed in the presence of uniform shear flow, with the vortices shed in cells of different frequency depending on the Reynolds number used for the simulation. At a Reynolds number of 100, two distinct cells of different shedding frequency with values $fD/U_c = 0.240$ and 0.283 were identified. The computed length of these cells was $5.63D$ and $2.37D$, with a dislocation at $z = 15.7D$ occurring periodically each five shedding cycles. A Reynolds number of 500 also yielded two cells, this time with values $fD/U_c = 0.244$ and 0.367 and lengths of $3.71D$ and $7.35D$, respectively. The dislocation here occurred at $z = 10.5D$.

The vortical structures in uniform flow at $Re = 100$ and 500 were in good qualitatively agreement with those reported by Miliou et al. (2007). At $Re = 100$ the vortex cores were vertical close to the body and exhibited slight distortions as they traveled further downstream, whereas at $Re = 500$ the vortical structures were characterized by three-dimensional wake instabilities of a smaller scale. While at $Re = 500$ most of the streamwise vorticity was due to instabilities, at a Reynolds number of 100 the production of streamwise vorticity was associated to curvature effects only. In the shear flow cases, due to the high shear rate imposed ($K = 0.1$), the vortical structures exhibited an increasing rate of obliqueness as they evolved downstream.

The issues presented in this work appear as very promising in the context of marine structures such as catenary risers and cable lines. It is therefore intended to extend this study to similar flow configurations, contributing thus to the knowledge of the flow physics of the wake past such geometries.

Appendix A

Paper Presented at the ETMM8 Conference

This appendix contains the paper included in the proceeding of the 8^{th} *International ER-COFTAC Symposium on Engineering Turbulence Modelling and Measurements* (ETMM8) in Marseille, France. Additionally, a poster was presented at the conference venue in June of 2010.

FLOW PAST A CURVED CIRCULAR CYLINDER IN UNIFORM SHEAR AT REYNOLDS NUMBER OF 500

J. P. Gallardo[1], *G. K. El Khoury*[1], *B. Pettersen*[1] *and H. I. Andersson*[2]

[1] *Department of Marine Technology, Norwegian University of Science and Technology, NO-7491 Trondheim , Norway*
[2] *Department of Energy and Process Engineering, Norwegian University of Science and Technology, NO-7491 Trondheim , Norway*

bjornar.pettersen@ntnu.no

Abstract

The effect of uniform shear on the flow past a curved cylinder has been studied by means of direct numerical simulations. The geometrical configuration consisted of a quarter-of-ring segment of non-dimensional radius of curvature 12.5, and a horizontal extension between the end of the bend and the outflow plane. The flow was directed towards the external face of the quarter-ring, and the non-dimensional shear-rate at the input was set to $K = 0$ and 0.1. One single shedding frequency prevailed along the entire span of the cylinder for $K = 0$ whereas at a non-dimensional shear-rate of $K = 0.1$, the shear flow gave rise to an oblique and cellular vortex shedding pattern with two dominant shedding frequencies decreasing toward the horizontal extension. The local base pressure coefficient for uniform shear gave evidence of a region dominated by favourable pressure gradient close to the top of the cylinder which resulted in a longer recirculation bubble in this region than for $K = 0$.

1 Introduction

Many offshore structures consist of several cylindrical elements. Catenary risers, cables and pipelines are examples of simple marine structures which create complex three-dimensional flow patterns when subjected to hydrodynamic loads. Miliou *et al.* (2003) approached this problem by considering the geometry of a catenary riser as a quarter segment of a ring, and performed simulations at $Re = 100$ for different flow configurations. In a subsequent work, Miliou *et al.* (2007) studied the same geometry with the free stream aligned with the plane of curvature of the cylinder at Reynolds numbers of 100 and 500. An interesting finding in their work was the presence of one single shedding frequency along the span of the cylinder when the flow was directed towards the outer face of the quarter-ring. This led to the conclusion that the vortex shedding was driven by the shedding arising at the top of the curved geometry.

Due to effects like wind and bottom interaction, ocean currents have non-uniform velocity profiles that affect the flow around bluff bodies. The physics of uniform shear flow past a straight circular cylinder are described by Zdravkovich (1997). The presence of a uniform shear-rate gives rise to a spanwise pressure-gradient that leads to a secondary flow in the front and rear stagnation zones. A similar type of secondary flow is induced by vorticity generated from the shear flow. Another interesting phenomenon that occurs in the presence of shear at the inlet is a cellular vortex shedding pattern induced by the spanwise variations in the Strouhal frequency. These three-dimensional effects are not easily extended to a curved circular cylinder because the distribution of the stagnation and the base pressure along the span is also affected by the curved geometry (see Miliou *et al.*, 2007).

In the present study we perform direct numerical simulation (DNS) of flow past a curved circular cylinder in uniform shear flow. This will enable us to study the effect of a uniform shear-rate on the instantaneous vortex topology, recirculation region as well as on the shedding mechanisms. In order to enable comparison with the published data, we intentionally considered a convex-shape geometry identical to that studied by Miliou *et al.* (2007) with uniform inflow.

2 Method

Flow configuration

Figure 1 shows a schematic view of flow past a curved cylinder which is composed of a quarter segment of a ring and a horizontal extension. Of particular importance in curved cylinder flows is the non-dimensional radius of curvature. This dimensionless parameter is defined as the ratio of the radius of curvature of the quarter-ring R to its cross-sectional diameter D. In the present study we consider a flow configuration identical to that of Miliou *et al.* (2007). This consists of a quarter-ring with curvature ratio $R/D = 12.5$ and a horizontal extension of length $10D$ between the end of the bend and the outflow plane. Throughout the present paper, the span s is defined as the arc-length of the deformed cylinder measured from the top plane; $s = R\theta$ with θ the angle measured from

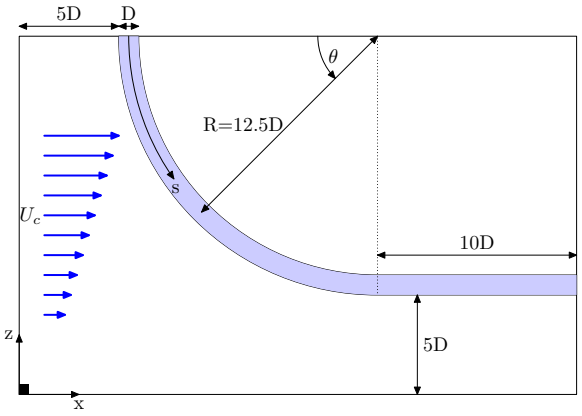

Figure 1: Computational domain size, geometry and flow configuration shown at the middle (x, z)-plane. The inflow velocity varies linearly in the z-direction, with an average value U_c at the mid height of the computational box. The spanwise coordinate s is measured along the cross-sectional axis following the curvature of the cylinder from the top plane, varying between 0 and $19.6D$ at the end of the bend.

the top plane.

The dynamics of the flow are described by the time-dependent Navier-Stokes equations for an incompressible Newtonian fluid expressed in non-dimensional form:

$$\frac{\partial u_i}{\partial x_i} = 0, \tag{1}$$

$$\frac{\partial u_i}{\partial t} + u_j \frac{\partial u_i}{\partial x_j} = -\frac{\partial p}{\partial x_i} + \frac{1}{Re}\frac{\partial^2 u_i}{\partial x_j^2}, \tag{2}$$

Here, the Reynolds number is based on the cylinder diameter and the inflow velocity at the mid height of the computational domain $Re = U_c D/\nu$, with ν the kinematic viscosity. For the simulations presented in this work we set $Re = 500$.

Numerical approach

The computational domain has streamwise length $L_x = 28D$, cross-stream width $L_y = 11D$ and vertical height $L_z = 18D$. The center of the ring is placed at $(18D, 5.5D, 18D)$. This gives a minimum distance of $5D$ between the solid body and the front, side and bottom planes. The grid resolution was kept the same for all simulations, and the number of grid points was $400 \times 150 \times 258$ in the x, y and z-directions, respectively. Non-uniform grid spacing has been used in the three non-homogeneous directions in order to adequately resolve the whole spectrum of scales. The minimum grid spacing was thus $\Delta x/D = 0.05$, $\Delta y/D = 0.02$ and $\Delta z/D = 0.057$.

As for boundary conditions, the following have been used:

(i) A free-slip condition on the top and bottom planes as well as on the sides of the computational domain.

(ii) A uniform shear velocity profile at the inlet, $U_\infty(z)/U_c = Kz/D + U_0/U_c$, where the non-dimensional inlet shear rate K was set to 0 and 0.1 for the two cases. Here, $K = (\partial U_\infty/\partial z)D/U_c$, with $\partial U_\infty/\partial z$ defined as the inflow shear rate; and U_0 is the inflow velocity at the bottom plane. In this context, we also define the local Reynolds number as $Re_l = U_\infty D/\nu$.

(iii) At the outlet, a Neumann boundary condition was prescribed for the velocities, i.e. $\partial u/\partial x = 0$, $\partial v/\partial x = 0$, and $\partial w/\partial x = 0$; in addition the pressure was set to zero. This gives a fully developed zero stress condition in order to avoid reflections from the outlet.

(iv) A direct forcing immersed boundary method (IBM) was used to transform the no-slip condition at the cylinder surface into internal boundary conditions at the nodes of the Cartesian grid on which the computations were performed. A least squares high-order method was considered for the interpolations. The detailed derivation, validation, and implementation of this technique in the code MGLET can be found in Peller *et al.* (2006).

The governing equations (1) and (2) have been directly solved with the code MGLET (see Manhart, 2004). MGLET is a finite-volume code in which the Navier-Stokes equations are discretised on a staggered Cartesian mesh with non-equidistant grid-spacing. The spatial discretization for the convective and diffusive terms is of second order. For the time advancement of the momentum equations an explicit third-order Runge-Kutta scheme is used. The incompressibility constraint is satisfied by solving the Poisson equation for the pressure by Stones strongly implicit procedure.

The constant time step used for the simulations was $\Delta t = 0.005D/U_c$ which ensured small values of the maximum Courant number. The flow field evolved to a quasi-periodic state at $tU_c/D \approx 100$, after which statistics were gathered for a period of $300D/U_c$. In order to verify that the current simulation is a fully resolved DNS, the Kolmogorov length scale η was estimated from the energy dissipation rate ϵ as $(\nu^3/\epsilon)^{1/4}$. The adopted grid spacing turned out to never exceed 4η.

3 Results and discussions

An interesting feature of the flow field is the variation of the mean pressure coefficient along the front and rear stagnation lines. This is depicted in figure 2 where C_p is defined as $2(P - P_\infty)/\rho U_\infty^2$. Along the front stagnation line, both the uniform ($K = 0$) and shear flow ($K = 0.1$) cases are characterized by a favourable pressure gradient which leads to the development of an axial flow along the outer face of the

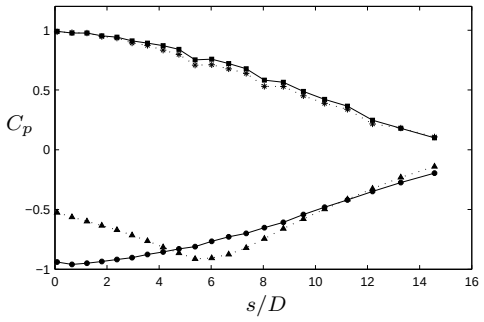

Figure 2: Mean pressure coefficients C_p along the span of the curved cylinder. Uniform flow at the inlet ($K = 0$): —■—, stagnation pressure coefficient; —●—, base pressure coefficient. Shear flow at the inlet ($K = 0.1$): $\cdots * \cdots$, stagnation pressure coefficient; $\cdots \blacktriangle \cdots$, base pressure coefficient.

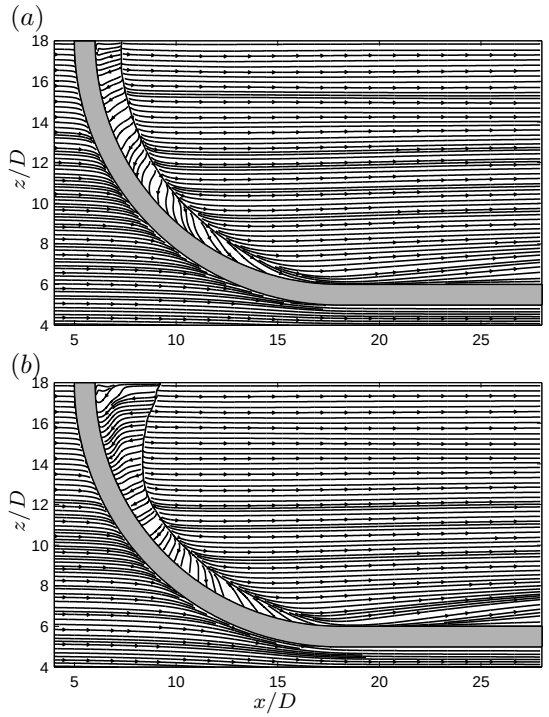

Figure 3: Streamlines of the mean flow in the middle (x, z)-plane. (a) Uniform; (b) shear flow.

quarter ring towards the horizontal cylindrical extension; see figure 3. Along the rear stagnation line the uniform flow case ($K = 0$) indicates the presence of an adverse pressure gradient along the entire span length. For the shear flow case ($K = 0.1$), however, the mean pressure coefficient exhibits a local minimum at $s/D \approx 5.5$, where a favorable pressure gradient builds-up afterwards. The region of favourable gradient yields a positive mean w-velocity which deflects the streamlines of the mean flow on the upper part of the recirculation zone as shown in figure 3(b).

It is well known that the base pressure distribution (i.e. pressure along the rear stagnation line) in-

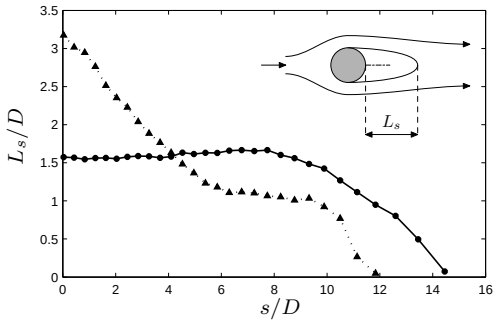

Figure 4: Recirculation length L_s along the span of the curved cylinder: —●— uniform flow ($K = 0$); —▲— shear flow ($K = 0.1$).

fluences, among other quantities, the size of the recirculation region which develops in the near-wake due to the separation of boundary layers from the surface of the solid body. This is reflected in figure 4 where the non-dimensional local separation length L_s/D is plotted along the span of the quarter-ring segment. Here, L_s is defined as the streamwise distance from the rear stagnation line to where the mean streamwise velocity changes sign from negative to positive. At the top plane, the local separation length for uniform shear is twice that for uniform flow. Moreover, the shape of the recirculation region is substantially affected by the shear induced motion. It changes from being relatively constant along a major part of the span for $K = 0$ to a monotonically decreasing pattern for $K = 0.1$. The two profiles intersect around $s/D \approx 4.5$ where the separation length for the uniform flow case becomes larger than that for uniform shear. Such a behaviour, along the first part of the cylinder, has its origin in the pressure coefficient distribution shown in figure 2. Uniform shear creates longer separation length which is coupled with higher base pressure for $s/D < 4.5$.

Frequency analysis

In order to investigate the shedding frequencies and instabilities in the wake, the time evolution of the cross-stream velocity v has been evaluated within the (x, z)-plane of symmetry of the cylinder. The total simulated time was $300D/U_c$ which covers about 67 shedding cycles for $K = 0$ and 73 shedding cycles for $K = 0.1$.

Shown in figure 5 is the time evolution of the v-velocity component taken along a sampling line located at $x/D = 18$. In accordance with Miliou *et al.* (2007), the pattern in figure 5(a) clearly indicates strong alternating vortex shedding along the whole span of the cylinder. However, some distinct dislocations are observed close to the horizontal extension between $z/D = 6$ and $z/D = 8$. In the presence of shear, on the other hand, the signal is less synchronized and characterized by non-periodic occurrence of vortex dislocations or vortex splits along the span. The corresponding time-traces of the v-velocity are shown

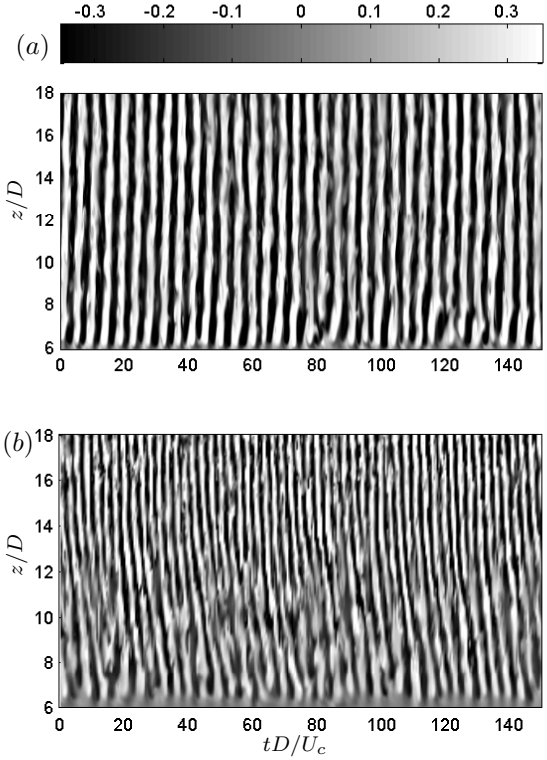

Figure 5: Time evolution of cross-stream velocity v along a sampling line taken at $x/D = 18$ in the middle (x, z)-plane. (a) Uniform flow; (b) shear flow.

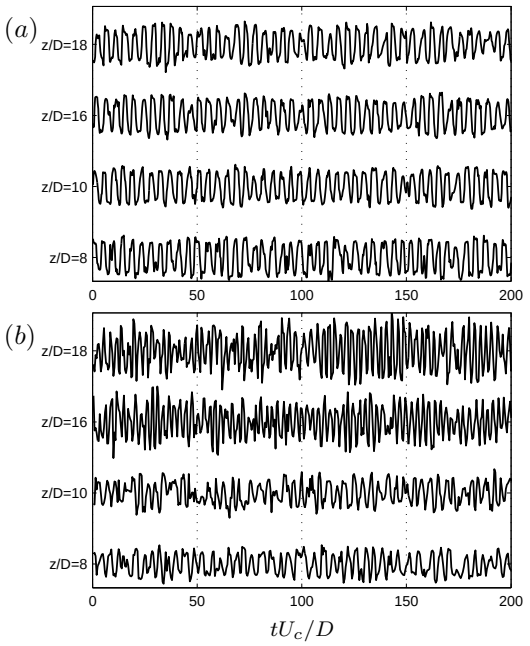

Figure 6: Time traces of cross-stream velocity v along a sampling line taken at $x/D = 18$ in the middle (x, z)-plane. (a) Uniform flow; (b) shear flow.

in figure 6 at four different vertical positions. In the case of uniform flow, the signals exhibit a fairly periodic behaviour with similar amplitudes at the different vertical positions. For uniform shear, however, noticeable differences exist in the amplitude and frequency of the time-traces between the lower positions at $z/D = 8$ and 10, and the upper positions at $z/D = 16$ and 18. Additionally, the time-traces become less periodic as compared to the uniform flow case. In both cases, the presence of interspersed distortions in the signal reveal the characteristic flow features of the transitional and turbulent regimes of the wake of a straight cylinder (Williamson, 1996; Karniadakis & Triantafyllou, 1992).

In order to identify the dominant shedding frequencies, a spectral analysis with basis on the time-domain signals of the v-velocity has been carried out. The sampling rate of the signals is $100U_c/D$, which is lower than the maximum value $1/\Delta t = 200U_c/D$ required to avoid aliasing effects (see Persillon & Braza, 1997). The v-velocity signals were taken at $x/D = 18$, and $z/D = 10$ and 18, and their spectra are shown in figure 7. The uniform flow case exhibits a wide-band spectrum with a dominant shedding frequency at $fD/U_c = 0.225$, as shown in figure 7(a). This suggests that despite the intermittent character of the flow observed in figure 6(a), the vortex street pattern prevails at one single shedding frequency along the span of the curved cylinder. On the other hand, figure 7(b) shows that for the shear flow case the peaks in the spectra of the two signals taken occur at different frequencies. At $z/D = 10$ ($Re_l = 550$) the spectrum is broadbanded and the peak occurs at $fD/U_c = 0.244$, while at $z/D = 18$ ($Re_l = 950$) it is clear that the dominant frequency is $fD/U_c = 0.367$.

The difference in the dominant frequencies revealed by figure 7 for the shear flow case indicates that the vortex shedding is arranged in a cellular pattern (see for instance the work by Narasimhamurthy *et al.*, 2009; and Mukhopadhyay *et al.*, 2002). This is evident in figure 8, where the dominant frequencies are plotted versus the local Reynolds numbers. The St-Re curve exhibits four frequency cells at $fD/U_c = 0.152$, 0.176, 0.244 and 0.367; with dislocations occurring at $Re_l = 361$, 384 and 575. The length of these cells is $0.17D$, $0.40D$, $3.71D$ and $7.35D$.

Instantaneous vortical structures

In order to explore the instantaneous vortex topology, regions of vortical motion are visualized using the λ_2 definition proposed by Jeong & Hussain (1995). Following Jeong & Hussain (1995), λ_2 identifies the region of minimum pressure due to swirling motion in an incompressible fluid based on the second largest eigenvalue of the symmetric tensor $\Omega_{ij}\Omega_{ij} + S_{ij}S_{ij}$, where S_{ij} is the symmetric and Ω_{ij} the antisymmetric part of the velocity gradient tensor.

The three-dimensional vortical structures observed in this case are displayed in figure 9. For both cases, uniform and shear flow, the isosurfaces of λ_2 reveal the

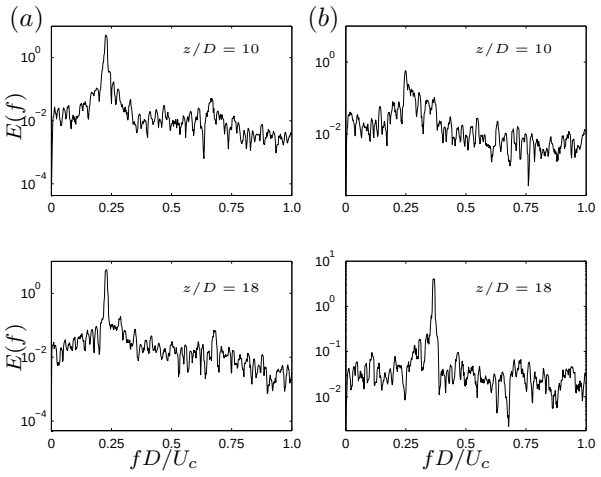

Figure 7: Power spectra of the v-velocity signal at $x/D = 18$, $z/D = 10$ and 18. (a) Uniform flow; (b) shear flow .

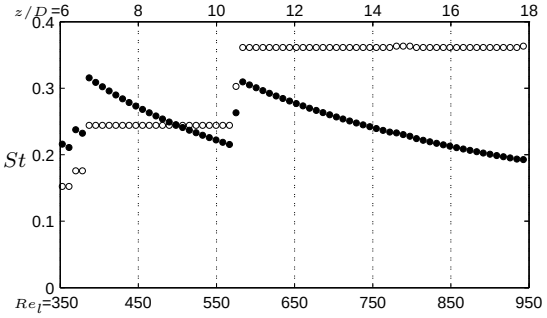

Figure 8: Strouhal frequencies along a sampling line taken at $x/D = 18$ in the middle (x, z)-plane. Shear flow case, •, St computed with the local inflow velocity U_∞; ∘, St computed with U_c.

presence of wake instabilities in the form of streamwise vortical structures. When the inflow is uniform, the topology of the vortical structures is similar to that observed by Miliou *et al.* (2007), the primary vortices are roughly aligned with the geometry of the curved cylinder and the stretching of these primary vortices gives birth to the streamwise vorticity. On the other hand, the shear flow case exhibits obliqueness of the primary vortices which increases as the primary vortices are convected downstream. Besides, due to the relatively large local Reynolds numbers in the upper portion of the domain, the vortical structures are characterized by a finer-scale relative to the uniform flow case.

According to Williamson (1992), a fundamental mechanism in the transition to turbulence in the wake of a straight cylinder is the appearance of intermittent spanwise vortex dislocations. This feature has its origin in the differences in frequency of the spanwise vortex shedding cells, producing streamwise vorticity where the spanwise vortices split. This process is

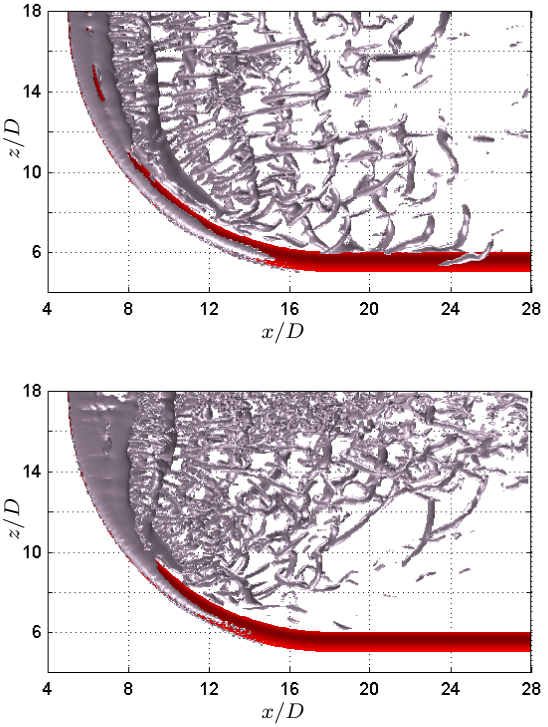

Figure 9: Side view showing isosurfaces of λ_2. (a) Uniform flow, $\lambda_2 = -1.5$; (b) shear flow, $\lambda_2 = -2.5$.

shown in figure 10(a) for the uniform flow case. The instantaneous streamwise vorticity, represented by the black isosurfaces, appears at the locations where splitting of the vertical vortices (white isosurfaces) occur. Another feature mentioned by Williamson (1992) is the helical twisting of the vortices, which is noticeable in the ω_z-isosurfaces in figure 10(a). When uniform shear is introduced to the flow, the ω_z-isosurfaces show different degrees of obliqueness and the instabilities exhibit a finer-scale relative to the uniform flow case, as seen in figure 10(b). Although the presence of streamwise vorticity is associated with three-dimensional instabilities in the flow, the shear rate at the inlet introduces a cross-stream vorticity component ω_y that is tilted when it interacts with the curved cylinder, turning ω_y into ω_x (see Woo *et al.*, 1989).

Finally, in order to study the evolution of the wake for the shear flow case, the instantaneous streamwise vorticity ω_x was plotted in three consecutive planes as depicted in figure 11. The (y, z)-plane at $x/D = 7$ reveals lower magnitudes of streamwise vorticity in the recirculation zone as compared to the planes at $z/D = 12$ and 18, where the wake has evolved. This delay in the appearance of ω_x seems surprising since this case possesses three sources of streamwise vorticity, namely the curvature of the cylinder, the wake instabilities and the shear rate.

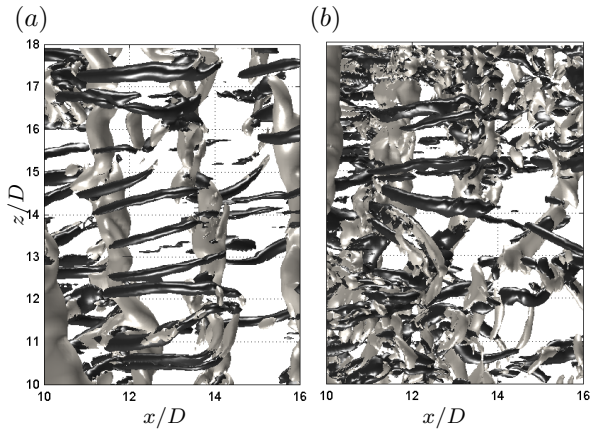

Figure 10: Detail of isosurfaces of instantaneous vorticity ω_x (black) and ω_z (white). (a) Uniform flow isosurfaces $\omega_x, \omega_z = \pm 1.8$; (b) shear flow isosurfaces at $\omega_x, \omega_z \pm 2.8$.

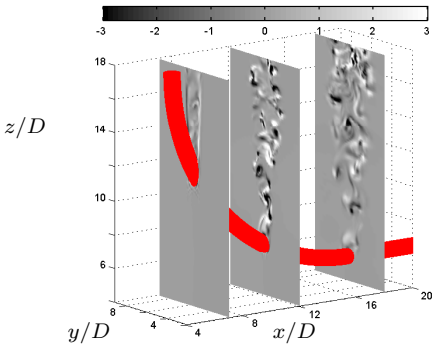

Figure 11: Cross-stream slices showing instantaneous streamwise vorticity ω_x at $x/D = 7$, 12 and 18 for the shear flow case.

4 Conclusions

In this work, DNS of the flow past a curved circular cylinder at $Re = 500$ is performed to study the influence of the curvature and different inflow conditions on the wake dynamics. In order to compare our results with the previous published studies, a uniform inflow profile was considered in an initial stage. Then the inflow condition was changed to a sheared inflow profile which varied linearly in the z-direction.

Concerning the recirculation region, the base pressure gradient for the uniform flow case was adverse along the whole span, while the shear flow case exhibited a region of favourable pressure gradient. This clearly affected the distribution of velocities in the recirculation zone and the size of the recirculation bubble. In the near wake, the time analysis for the shear flow case revealed two distinct cells of shedding frequency with values $fD/U_c = 0.244$ and 0.367. The length of these cells was $3.71D$ and $7.35D$, with a dislocation occurring at $z = 10.5D$. From the vortical structures analysis, streamwise wake instabilities were identified in both cases. However, the shear flow case was characterized by oblique vortex shedding as the wake evolved downstream.

The issues presented here appear as very promising in the context of marine structures such as catenary risers and cable lines. It is therefore intended to extend this study to similar flow configurations, contributing thus to the knowledge of the flow physics of the wake past such geometries.

Acknowledgments

This study was partially supported by the Norwegian HPC project NOTUR that granted access to its computer facilities.

References

Jeong J. and Hussain F. (1995), On the identification of a vortex, *J. Fluid Mech.*, Vol. 285, pp. 69–94.

Karniadakis G. E. and Triantafyllou G. S. (1992), Three-dimensional dynamics and transition to turbulence in the wake of bluff objects, *J. Fluid Mech.*, Vol. 238, pp. 1–30.

Manhart M. (2004), A zonal grid algorithm for DNS of turbulent boundary layers, *Comput. Fluids*, Vol. 33, pp. 435–461.

Miliou A., Sherwin S. J. and Graham J. M. R. (2003), Fluid dynamic loading on curved riser pipes, *J. Offshore Mech. Arct.*, Vol. 125, pp. 176–182.

Miliou A., De Vecchi A., Sherwin S. J. and Graham J. M. R. (2007), Wake dynamics of external flow past a curved circular cylinder with the free stream aligned with the plane of curvature, *J. Fluid Mech.*, Vol. 592, pp. 89–115.

Mukhopadhyay A., Venugopal P. and Vanka S. P. (2002), Oblique vortex shedding from a circular cylinder in linear shear flow, *Comput. Fluids*, Vol. 31, pp. 1–24.

Narasimhamurthy V. D., Andersson H. I. and Pettersen B. (2009), Cellular vortex shedding behind a tapered circular cylinder, *Phys. Fluids*, Vol. 21, pp. 1–12.

Peller N., Le Duc A., Tremblay F. and Manhart M. (2006), High-order stable interpolations for immersed boundary methods, *Int. J. Numer. Meth. Fluids*, Vol. 52, pp. 1175–1193.

Persillon H. and Braza M. (1998), Physical analysis of the transition to turbulence in the wake of a circular cylinder by three-dimensional NavierStokes simulation, *J. Fluid Mech.*, Vol. 365, pp. 23–88.

Williamson C. H. K. (1992), The natural and forced formation of spot-like vortex dislocations in the transition of a wake, *J. Fluid Mech.*, Vol. 243, pp. 393–441.

Williamson C. H. K. (1996), Three-dimensional wake transition, *J. Fluid Mech.*, Vol. 328, pp. 345–407.

Woo H. G. C., Cermak J. E. and Peterka J. A. (1989), Secondary flows and vortex formation around a circular cylinder in constant-shear flow, *J. Fluid Mech.*, Vol. 204, pp. 523–542.

Zdravkovich M. M. (1997), Flow Around Circular Cylinders, Vol. 1 Fundamentals, Oxford University Press.

Appendix B

Paper Presented at the ECCOMAS CFD 2010 Conference

This appendix contains the paper included in the proceeding of the 5^{th} *European Conference on Computational Fluid Dynamics* (ECCOMAS CFD 2010) in Lisbon, Portugal. This was additionally presented orally at the conference venue in June of 2010.

V European Conference on Computational Fluid Dynamics
ECCOMAS CFD 2010
J. C. F. Pereira and A. Sequeira (Eds)
Lisbon, Portugal,14-17 June 2010

EFFECTS OF UNIFORM SHEAR ON THE FLOW PAST A CURVED CIRCULAR CYLINDER

José P. Gallardo*, George K. El Khoury*, Bjørnar Pettersen* and Helge I. Andersson†

*Norwegian University of Science and Technology, Department of Marine Technology
NO-7491 Trondheim, Norway
e-mail: bjornar.pettersen@ntnu.no

†Norwegian University of Science and Technology, Department of Energy and Process Engineering
NO-7491 Trondheim, Norway
e-mail: helge.i.andersson@ntnu.no

Key words: Curved circular cylinder, Shear flow, DNS, Immersed Boundary Method

Abstract. *The effect of uniform shear on the flow past a curved cylinder at a Reynolds number of* 100 *has been studied by means of Direct Numerical Simulations on a staggered Cartesian grid. The non-slip condition at the solid walls was taken into account by a direct forcing Immersed Boundary Method. The geometrical configuration consisted of a quarter-of-ring segment of non-dimensional radius of curvature* 12.5*, and a horizontal extension between the end of the curved segment and the outflow plane. The flow was directed towards the convex face of the quarter-ring, and the non-dimensional shear-rate at the input was set to* $K = 0$ *and* 0.1*. One single shedding frequency prevailed along the entire span of the cylinder for uniform flow (*$K = 0$*) whereas at a non-dimensional shear-rate of* $K = 0.1$*, the shear flow gave rise to an oblique and cellular vortex shedding pattern with two dominant shedding frequencies decreasing toward the horizontal extension. The dislocations occurred periodically each five shedding cycles and at a local Reynolds number of* 167*. The mean local base pressure for uniform shear gave evidence of a region dominated by a fairly low favourable pressure gradient close to the top of the cylinder which resulted in a longer recirculation bubble in this region than for* $K = 0$*.*

1 INTRODUCTION

Flows around circular cylinders comprise a variety of complex flow phenomena which depend on the shape and orientation of the cylinder with respect to the flow direction as well as on the incoming flow conditions. The flow past a straight circular cylinder is perhaps the simplest of these configurations, and it is hardly surprising that this flow problem has been extensively investigated during the past decades by means of laboratory experiments and computer simulations. Zdravkovich,[1] for instance, has provided a comprehensive review on this topic.

In many industrial applications, however, the flow past non-uniform circular cylinders is frequently encountered. Such types of configurations give rise to different wake dynamics compared to straight cylinder flows. A ring or torus with a circular cross-section, which is obtained by bending a straight circular cylinder, represents an example of a non-uniform cylinder geometry. Although the flow around a ring has been studied previously,[2–4] most of the studies have been focused on flows with the free stream aligned normal to the plane of curvature of the ring. A variant of the ring-like geometry may be found in offshore structures and marine operations, where hanging risers, anchor lines and pipelines form catenaries whose geometries resemble that of a quarter turn of a ring with a high radius of curvature. Miliou *et al.*[5] used this geometry to investigate the flow past a riser at $Re = 100$ by means of Direct Numerical Simulations (DNS) with the free-stream coming from different directions. In a subsequent work, Miliou *et al.*[6] studied the same geometry with the free stream aligned parallel to the plane of curvature of the cylinder at Reynolds numbers of 100 and 500. In this case, the authors observed different features in the vortex shedding depending on the orientation of the cylinder with respect to the flow direction.

The other parameter affecting the wake in the flow past a circular cylinder, namely the incoming flow condition, is of particular importance to the marine industry since ocean currents interacting with waves, wind and the sea bottom have non-uniform vertical velocity profiles. The experimental[7–10] and numerical[11,12] studies of the flow past a circular cylinder in uniform shear flow have revealed the presence of secondary flows as well as oblique and cellular vortex shedding as a direct consequence of the inflow condition. Due to the shear effect, pressure gradients are generated along the front and rear stagnation lines, causing secondary flows to appear at these locations. The experimental work done by Woo *et al.*[8] estimated magnitudes for the mean velocities induced by these pressure gradients. In addition, the presence of horseshoe vortices may enhance these secondary flows on the rear stagnation line. The numerical simulations of Miliou *et al.*[6] on curved circular cylinder flows predicted the existence of pressure gradients dictated by the geometry along the front and rear stagnation lines. This induced secondary flows along the stagnation lines. It seems therefore interesting to investigate the effects of combining incoming shear flow with a non-uniform geometry like a curved cylinder.

In the present study we perform DNS of the flow past a curved circular cylinder in uniform shear flow. This will enable us to study the effect of a uniform shear-rate on the

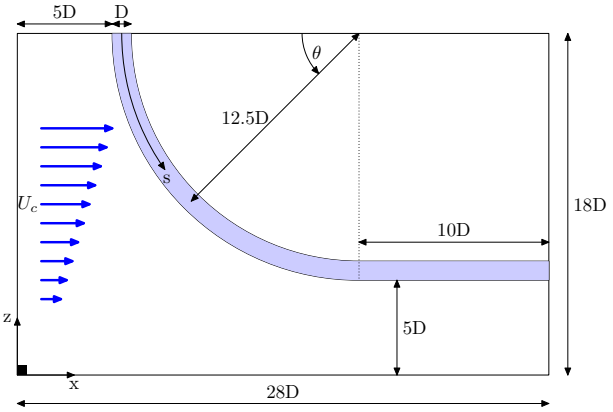

Figure 1: Computational domain size, geometry and flow configuration shown at the middle (x, z)-plane. The size of the computational domain is $28D$, $11D$ and $18D$ in the x-,y- and z-directions, respectively. The inflow velocity varies linearly in the z-direction, with an average value U_c at the mid height of the computational domain. The spanwise coordinate s is measured along the cross-sectional axis following the curvature of the cylinder from the top plane, varying between 0 and $19.6D$ at the end of the bend.

instantaneous vortex topology, recirculation region as well as on the shedding mechanisms. The previous DNSs with this geometry[5,6] were performed using a spectral/hp element Navier-Stokes solver and a boundary-fitted grid. In the present study the solution of the Navier-Stokes equations is obtained with a Cartesian grid solver, and a direct forcing Immersed Boundary Method (IBM) is used to implement the non-slip boundary condition at the solid surfaces. It is thus intended to check the overall performance of these methods for the complex geometry involved. In order to achieve this comparison, we intentionally considered a convex-shape geometry identical to that studied by Miliou *et al.*[6] with uniform inflow.

2 FORMULATION

2.1 Flow configuration

Figure 1 shows a schematic view of flow past a curved cylinder which is composed of a quarter segment of a ring and a horizontal extension. Of particular importance in curved cylinder flows is the non-dimensional radius of curvature. This dimensionless parameter is defined as the ratio of the radius of curvature of the quarter-ring R to its cross-sectional diameter D. In the present study we consider a flow configuration identical to that of Miliou *et al.*[6] This consists of a quarter-ring with curvature ratio $R/D = 12.5$ and a horizontal extension of length $10D$ between the end of the bend and the outflow plane. Throughout the present paper, the span s is defined as the arc-length of the curved cylinder measured from the top plane; i.e. $s = R\theta$ with θ the angle measured in radians from the top plane.

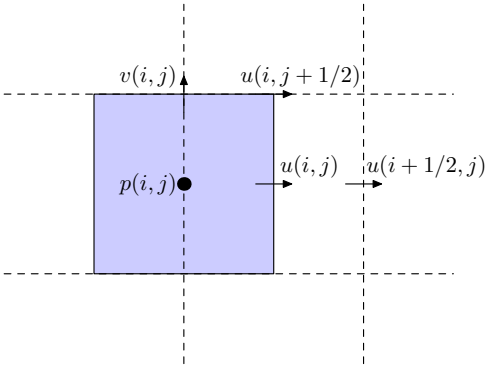

Figure 2: Control volumes for the u-velocity (dashed lines) and the pressure (gray) in the staggered grid.

2.2 Governing equations of fluid motion

The dynamics of the flow are described by the time-dependent Navier-Stokes equations for an incompressible Newtonian fluid expressed in non-dimensional form:

$$\frac{\partial u_i}{\partial x_i} = 0, \tag{1}$$

$$\frac{\partial u_i}{\partial t} + u_j \frac{\partial u_i}{\partial x_j} = -\frac{\partial p}{\partial x_i} + \frac{1}{Re}\frac{\partial^2 u_i}{\partial x_j^2}, \tag{2}$$

Here, the Reynolds number is based on the cylinder diameter and the inflow velocity at the mid height of the computational domain, $Re = U_c D/\nu$, with ν the kinematic viscosity. For the simulations presented in this work we set $Re = 100$.

2.3 Numerical method

The governing equations (1) and (2) have been directly solved with the code MGLET. In this finite-volume code, the Navier-Stokes equations for an incompressible fluid are discretised on a staggered Cartesian mesh with non-equidistant grid-spacing.[13,14] The mid-point rule[14] is employed to approximate the fluxes with the variables defined on the control cell shown in figure 2. The velocities $u(i+1/2,j)$ and $u(i,j+1/2)$ at the faces of the momentum cell for the u-velocity are obtained by linear interpolation. A central difference scheme is used to approximate the derivatives in the x- and y-directions at the positions $(i+1/2,j)$ and $(i,j+1/2)$ respectively, ensuring second order accuracy in the spatial discretization of the convective and diffusive terms.[15]

For the time advancement of the momentum equations an explicit third-order Runge-Kutta scheme is used. The pressure at the new time level $n+1$ is found by solving the Poisson equation for the pressure correction $\Delta p^{n+1} = p^{n+1} - p^n$ based on the the intermediate velocity fields $\mathbf{u}^*$ computed from the momentum equation (2). The Poisson equation is solved iteratively by the Stones strongly implicit procedure (SIP), producing intermediate pressure p^* and velocity $\mathbf{u}^*$ fields at each iteration. The divergence of the

intermediate velocity fields $\mathrm{div}(\mathbf{u}^*)$ is checked against a defined tolerance ϵ for each iteration. When $\mathrm{div}(u^*) \leq \epsilon$ the intermediate pressure and velocity fields are updated at the next time step t^{n+1}.

2.4 Immersed boundary method

At the walls, the non-slip and non-impermeability conditions are taken into account by using a *direct forcing* Immersed Boundary Method (IBM). Basically, the cells at the fluid-solid interface are transformed into internal boundary conditions on the corresponding computational domain by using higher order interpolation from the fluid cells in the vicinity of the body. This method represents a simple way to deal with complex geometries avoiding the need to generate a body fitted grid. A detailed review of the IBM method is found in the work by Mittal and Iaccarino.[16]

The general stencil configuration for the IBM method is depicted in figure 3 for the one-dimensional case. Here ϕ represents one of the velocity components, ϕ_0 is the internal Dirichlet boundary condition, ϕ_r the value at the wall; and ϕ_1, ϕ_2 and ϕ_3 the values in the fluid used for the interpolation. The internal boundary condition based on interpolation from N neighboring cells is determined by the following expression

$$\phi_0 = \left(\sum_{i=1}^{N} \alpha_i \phi_i \right) + \alpha_r \phi_r \tag{3}$$

where α_i and α_r are the interpolation coefficients for the variable ϕ at the fluid cells and the body, respectively.

As mentioned above, MGLET uses a Cartesian staggered grid, which means that the boundaries between velocity and pressure cells do not coincide, as shown in figure 2. The blocking strategy for the IBM method is pressure oriented, then the blocked cells are pressure cells that lie within the surfaces that demarcate the solid walls. According to this criterion, the blocked velocity cells are those touched by the blocked pressure cells.

The interpolation can be either carried out by Lagrange polynomials or using least squares interpolation. It was shown by Peller *et al.*[17] that the interpolation coefficients α_i and α_r depend only on the geometry, thus they can be determined in a preprocessing step. In order to account for three-dimensionality, weighting factors are estimated in the different directions to compute ϕ_0. Finally, the computational representation of the body can be done analytically or using a non-structured mesh consisting of triangles.

2.5 Simulation parameters and implementation

In the present work the dimensions of the grid in each direction are $N_x = 400$, $N_y = 150$ and $N_z = 258$, resulting in a total of 15.48×10^6 grid points. The data for a straight uniform circular cylinder presented by Zdravkovich[1] was used to interpolate the boundary layer thickness δ, obtaining $\delta \approx 0.5D$ at $Re = 100$. In order to adequately resolve the details of the boundary layer and the wake, non-uniform grid spacing is used in

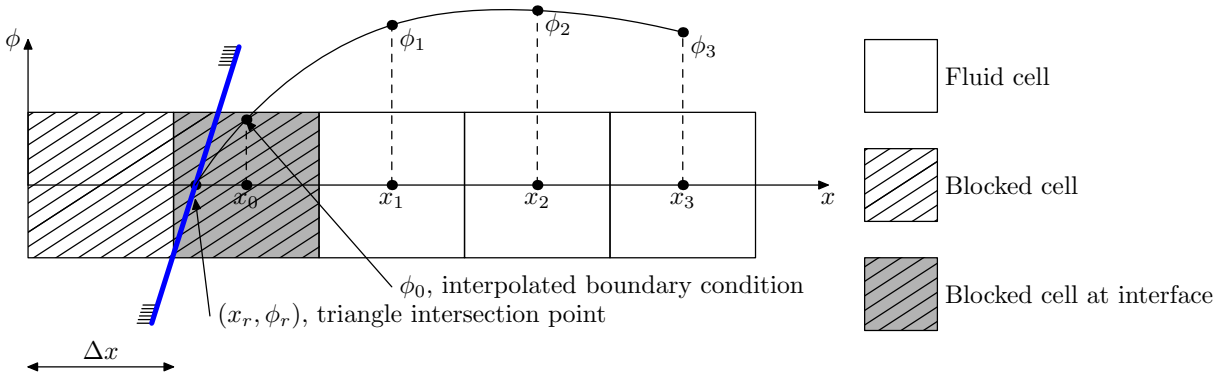

Figure 3: One-dimensional stencil for the interpolation in the x-direction using the IBM method; the body boundary corresponds to the thick blue line. Adapted from the work by Peller *et al.*[17]

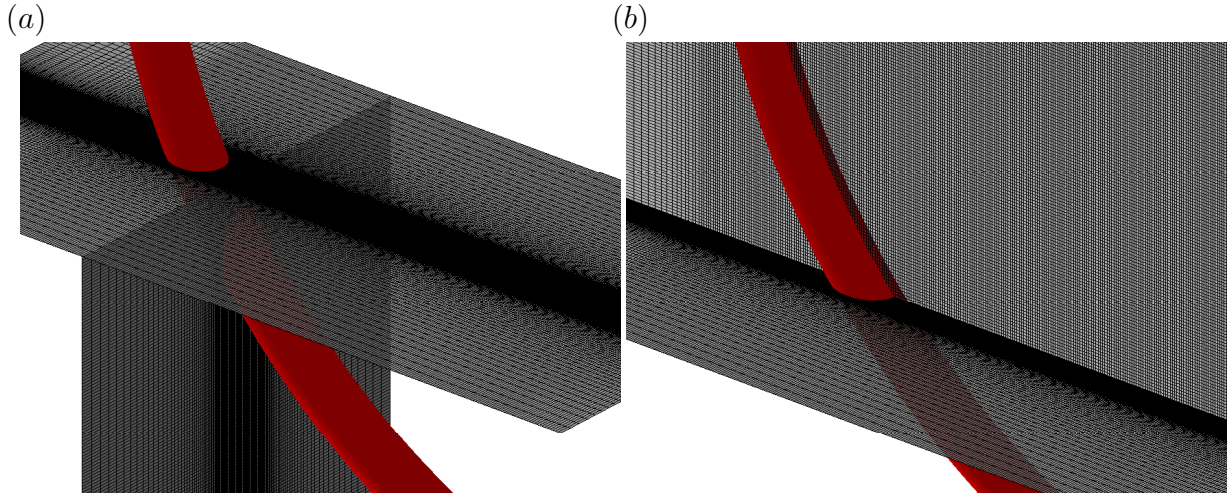

Figure 4: Detail of the $400 \times 150 \times 258$ Cartesian mesh around the curved cylinder . (a) View of the (x, y)- and (y, z)-planes; (b) (x, y)- and (x, z)-planes.

the three spatial directions. The minimum grid spacing for the uniform and shear flow cases are $\Delta x/D = 0.05$, $\Delta y/D = 0.02$ and $\Delta z/D = 0.057$ in the x-, y- and z-directions respectively. Different planes of the mesh close to the body are shown in figure 4, depicting the clustering of points in the vicinity of the body.

Figure 5 shows the blocking of the Cartesian grid by the IBM method in the (x, y)- and (y, z)-planes. The least squares method was chosen as interpolation scheme since it possesses better stability properties than the Lagrange interpolation method.[17] The body composed of a quarter-ring and a horizontal extension were represented by a structured mesh consisting of triangles. The resolution of this mesh was rather high in order to avoid errors in the representation of the curved surfaces. In addition, the following boundary conditions were imposed:

1. A free-slip condition on the horizontal top ($z = 18D$) and bottom ($z = 0$) planes as

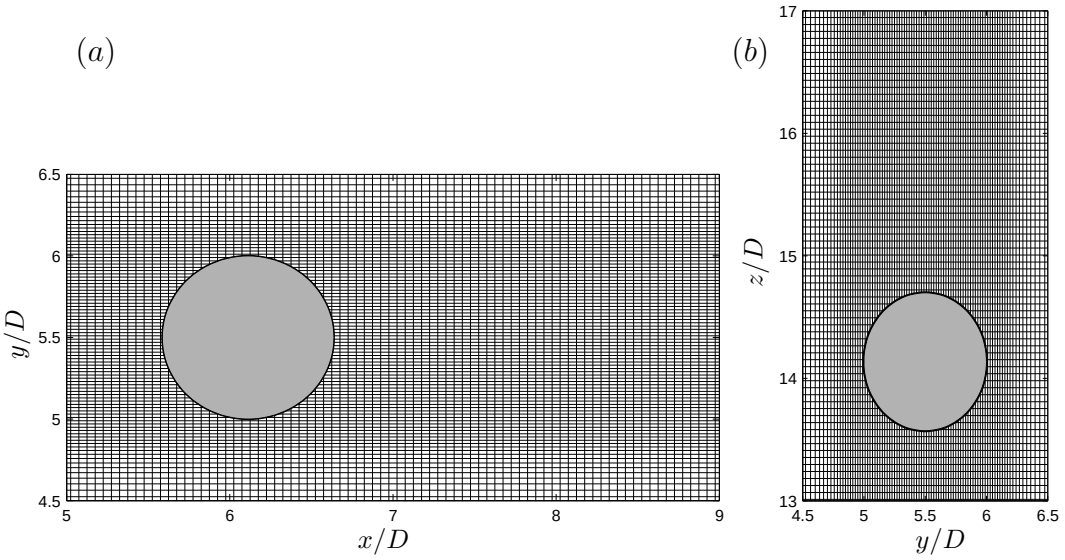

Figure 5: View of the blocking of cells in the Cartesian mesh by the IBM method. (a) View of the (x, y)-plane at $z/D = 14$; (b) (y, z)-plane at $x/D = 12$.

well as on the vertical sides ($y = 0$ and $11D$) of the computational domain.

2. A uniform shear velocity profile at the inlet,

$$\frac{U_\infty(z)}{U_c} = \frac{Kz}{D} + \frac{U_0}{U_c}, \tag{4}$$

where the non-dimensional inlet shear rate K was set to 0 and 0.1 for the two cases studied. Here, $K = (dU_\infty/dz)D/U_c$, with dU_∞/dz defined as the inflow shear rate; and U_0 is the inflow velocity at the bottom plane ($z = 0$). In this context, we also define the local Reynolds number as $Re_l(z) = U_\infty(z)D/\nu$.

3. At the outlet ($x = 28D$), a Neumann boundary condition was prescribed for the velocities, i.e. $\partial u/\partial x = 0$, $\partial v/\partial x = 0$, and $\partial w/\partial x = 0$; in addition the pressure was set to zero ($p = 0$). This gives a fully developed zero stress condition in order to avoid reflections from the outlet.

The constant time step used for the simulations was $\Delta t = 0.005D/U_c$ which ensured low values of the maximum Courant number. The flow field evolved to a quasi-periodic state at $tU_c/D \approx 100$, after which statistics were gathered for a period of $300D/U_c$.

The code was run in parallel on an *IBM p*575+ machine. A discussion on the efficiency of the parallelization in the code MGLET is found in the work by Manhart *et al.*[13] All the simulations were run on 48 processors, the domain decomposition consisted of 16 processors in the x-direction and 3-processors in the y-direction. In average, the time required to compute one time-step was 2 seconds, resulting in approximately 33 hours to run the 60000 time steps required to gather statistics.

3 RESULTS

3.1 Near wake flow

An interesting feature of the flow field is the variation of the mean pressure along the front and rear stagnation lines. This is depicted in figure 6(a) where the non-dimensional mean stagnation pressure $P_s/\rho U_0^2$ is plotted as a function of the span s. Along the front stagnation line, both the uniform ($K = 0$) and shear flow ($K = 0.1$) cases are characterized by a negative pressure gradient ($\partial p/\partial s < 0$) which leads to the development of an axial flow along the convex face of the quarter ring towards the horizontal cylindrical extension. Along the rear stagnation line the uniform flow case ($K = 0$) indicates the presence of a positive gradient along the entire span length ($\partial p/\partial s > 0$). For the shear flow case ($K = 0.1$), however, the mean pressure exhibits a weak negative pressure gradient up to $s/D \approx 4$, where a positive pressure gradient builds-up afterwards.

It is well known that the base pressure distribution (i.e. pressure along the rear stagnation line) influences, among other quantities, the size of the recirculation region which develops in the near-wake due to the separation of boundary layers from the surface of the solid body. This is reflected in figure 6(b) where the non-dimensional local separation length L_s/D is plotted along the span of the quarter-ring segment. Here, L_s is defined as the streamwise distance from the rear stagnation line to where the mean streamwise velocity changes sign from negative to positive. At the top plane, the local separation length for the uniform flow case is approximately $1.5D$; this value remains constant up to $s/D \approx 8$, then it starts decreasing monotonically, reaching zero close to the horizontal part of the cylinder, at $s/D \approx 15$. The variation of L_s for the shear flow case is fairly similar to that of the uniform flow case, but instead of being constant between the spanwise locations 0 and 8 it exhibits a local minimum at $s/D \approx 5$. Such a behaviour, along the first part of the span, has its origin in the pressure coefficient distribution shown in figure 6(a). It is noteworthy that the recirculation length for the shear flow case ($K = 0.1$) is larger than that for the uniform flow case ($K = 0$) at all the spanwise locations.

Further differences between the uniform and shear flow cases are noticeable by looking at the isocontours of mean u- and w-velocities, shown in figures 7(a) to 7(d). When the inflow is uniform ($K = 0$), the lowest mean streamwise velocities in the recirculation region occur close to the top of the cylinder, as seen in figure 7(a), while at a shear rate of 0.1 the region of lowest mean u-velocities is located downwards between $z/D = 12$ and 14 (figure 7c). The contour plot of mean w-velocity for the shear flow case displays a large region with positive vertical velocities on the upper part of the recirculation region (figure 7d); in this case the contours of negative w-velocities are located close to the horizontal extension, with the region of positive velocities above. The uniform flow case, on the other hand, exhibits only a thin region of positive mean w-velocities attached to the rear stagnation line, and negative mean w-velocities prevailing in the rest of the recirculation zone (figure 7b).

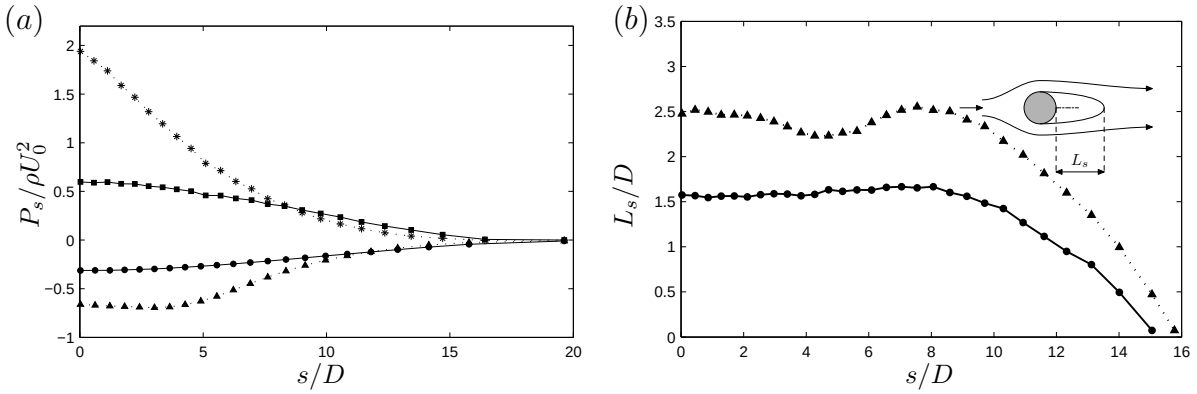

Figure 6: Near wake behaviour for the uniform and shear flow cases. (a) Pressure P_s on the front and rear stagnation lines along the span of the curved cylinder. Uniform flow at the inlet ($K = 0$): —■—, stagnation pressure coefficient; —●—, base pressure coefficient. Shear flow at the inlet ($K = 0.1$): ···∗···, stagnation pressure coefficient; ···▲···, base pressure coefficient. (b) Recirculation length L_s along the span of the curved cylinder: —●— uniform inflow ($K = 0$); —▲— shear inflow ($K = 0.1$).

3.2 Analysis of vortex shedding pattern

In the previous subsection it was discussed how the curved shape and the inflow condition affect the near wake flow. As the flow evolves downstream, the different types of instabilities created close to the body will be amplified, leading to a regular shedding of vortices commonly referred to as a Kármán vortex street. In a similar way as for the near wake flow, the frequency of the shedding and the shape of these vortices will vary according to the geometry and the incoming flow conditions. Figure 8 shows the time evolution of the cross-stream velocity v along a vertical line taken at $x/D = 18$ and the vortical structures depicted by instantaneous λ_2-isosurfaces.[18] The scalar quantity λ_2 defines a region of minimum pressure due to swirling motion in an incompressible fluid based on the second largest eigenvalue of the symmetric tensor $\Omega_{ij}\Omega_{ij} + S_{ij}S_{ij}$, where S_{ij} is the symmetric component of the velocity gradient tensor and Ω_{ij} the antisymmetric part.

$$S_{ij} = \frac{1}{2}\left(\frac{\partial u_i}{\partial x_j} + \frac{\partial u_j}{\partial x_i}\right), \tag{5}$$

$$\Omega_{ij} = \frac{1}{2}\left(\frac{\partial u_i}{\partial x_j} - \frac{\partial u_j}{\partial x_i}\right). \tag{6}$$

The v-velocity signal taken for the uniform flow case ($K = 0$) shown in figure 8(a) is periodic along the vertical line, the pattern clearly corresponds to regular laminar flow, with no distortions occurring; the vortex cores represented as isosurfaces of $\lambda_2 = -0.1$ are vertical close to the body, presenting slight distortions as they move downstream. As previously reported by Miliou *et al.*,[6] the vortex shedding pattern for $K = 0$ corresponds to that of laminar flow, no dislocations occur despite the non-uniform geometry of the cylinder. A question that remains open here is whether cellular vortex shedding will occur or not if the radius of curvature R is increased; this topic is currently under investiga-

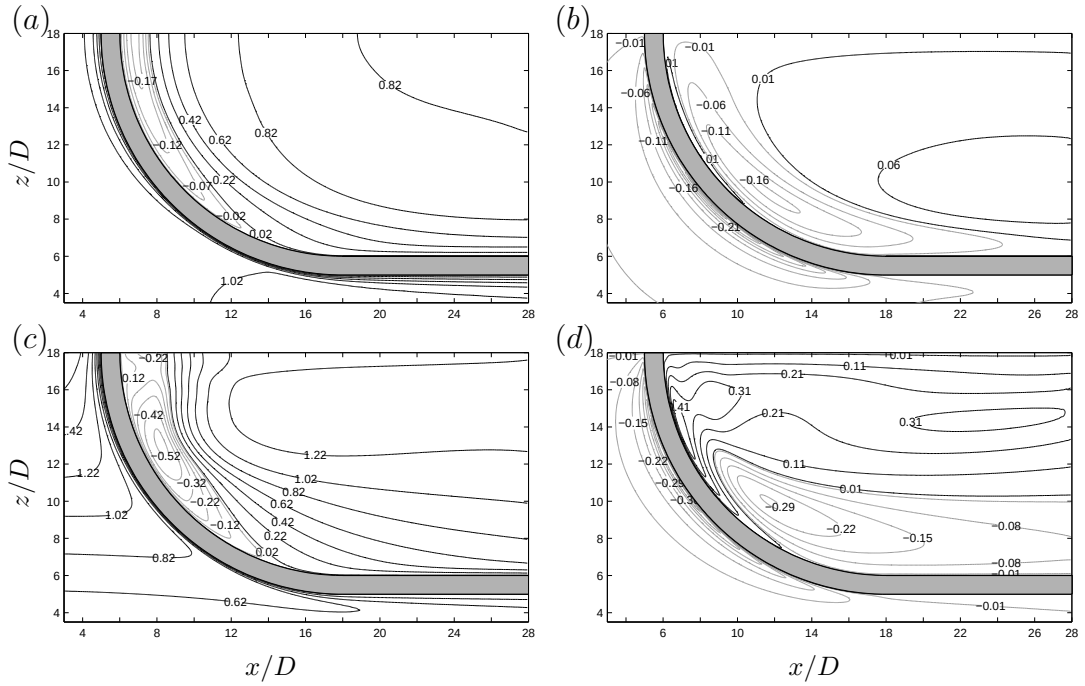

Figure 7: Isocountours of mean streamwise and vertical velocities in the (x, z)-plane. (a) Mean u-velocities for the uniform flow case; (b) mean w-velocities for the uniform flow case; (c) mean u-velocities for the shear flow case; and (d) mean w-velocities for the shear flow case.

tion. For the shear flow case ($K = 0.1$), on the other hand, periodic dislocations can be identified in the upper part of the domain in the time evolution of v, as seen in figure 8(b). These dislocations arise at a local Reynolds number of 167 ($z/D = 15.7$), close to the Reynolds number range at which the mode A instabilities described by Williamson[19] appear. Furthermore, the vortex cores represented as isosurfaces of $\lambda_2 = -0.1$ display a high degree of obliqueness relative to the vertical, also a consequence of the shear rate imposed.

The plot of the time traces of the cross-stream velocities at $x/D = 18$ and at six different positions along the z-axis shown in figure 9(a) gives a clear picture of the periodic behaviour of the uniform flow case. With the exception of the time trace at $z/D = 8$, where the vortex shedding is less energetic, all the traces plotted have almost the same amplitude. In this case the suppression of the vortex shedding occurs at $z/D \approx 7$. At an inflow shear rate of 0.1, the trace signals of the v-velocities clearly differ from those corresponding to uniform inflow. The behaviour in this case is quasi-periodic, with the suppression of vortex shedding occurring around $z/D \approx 10$. The periodic dislocations shown in figure 8(b) are due to the splitting of the Kármán vortices as they are shed from the upper segment of the curved cylinder. This splitting, for instance, can be identified in the v-velocity trace at $z/D = 16$; here the signal exhibits a low frequency modulation and the dislocations occur each five shedding cycles.

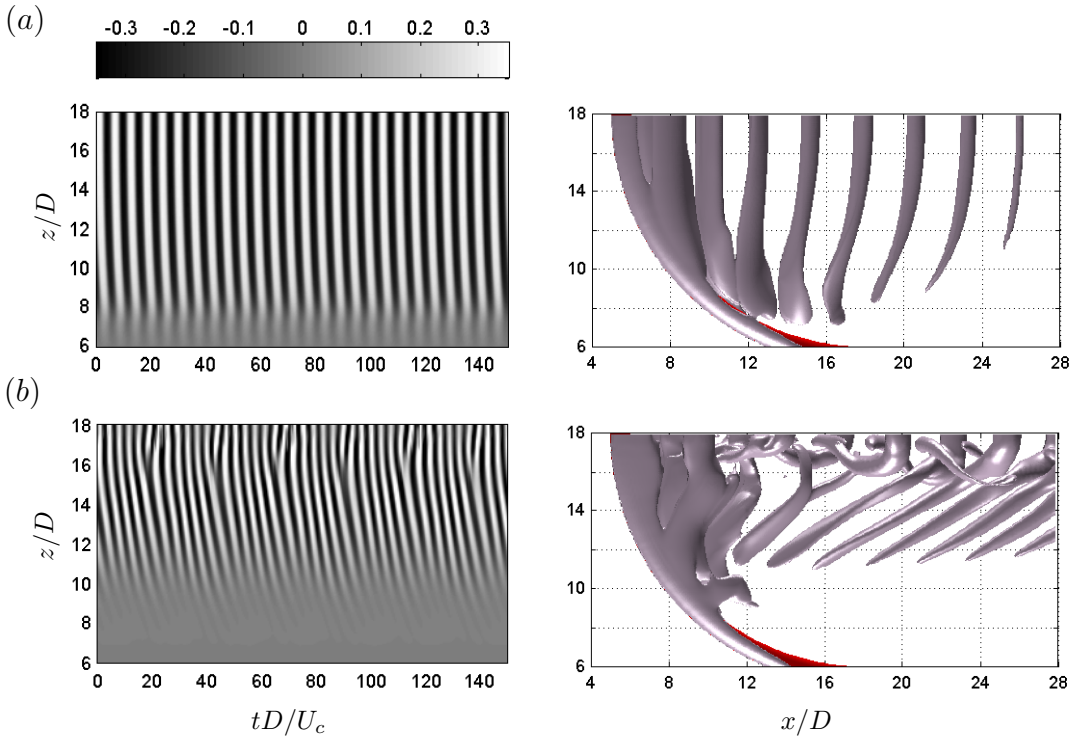

Figure 8: Time evolution of cross-stream velocity v along a sampling line taken at $x/D = 18$ in the middle (x, z)-plane ($y/D = 5.5$) to the left, and vortex cores represented as isosurfaces of $\lambda_2 = -0.1$ to the right. (a) Uniform inflow; (b) shear inflow.

In order to identify the dominant shedding frequencies, a spectral analysis with basis on the time-domain signals of the v-velocity has been carried out. The sampling rate of the signals is $100U_c/D$, which is lower than the maximum value $1/\Delta t = 200U_c/D$ required to avoid aliasing effects (see Persillon & Braza[20]). The dominant shedding frequency obtained by Fourier analysis for the uniform flow case is $fD/U_c = 0.176$, prevailing along the whole sampling line, with no cellular arrangement of the vortices. This is in good agreement with the frequency 0.1761 reported by Miliou *et al.*[6] for their convex configuration. It has been shown in previous studies of circular cylinders that when uniform shear flow is imposed as an inflow boundary condition, the vortex shedding will arrange in a cellular pattern; see for instance the work by Mukhopadhyay *et al.*[11] This is the case in figure 10(a), where the dominant frequencies are plotted versus the local Reynolds numbers. The *St-Re* curve exhibits two frequency cells at $fD/U_c = 0.240$ and 0.283, with lengths $5.63D$ and $2.37D$ respectively; here the dislocation occurs at $Re_l = 167$ ($z/D = 15.7$). Shown in figure 10(b) are the isocountours of streamwise vorticity ω_x in the middle (x, z)-plane, displaying the highest intensities close to the top of the computational domain. Close to the upper part of the body, regions of streamwise

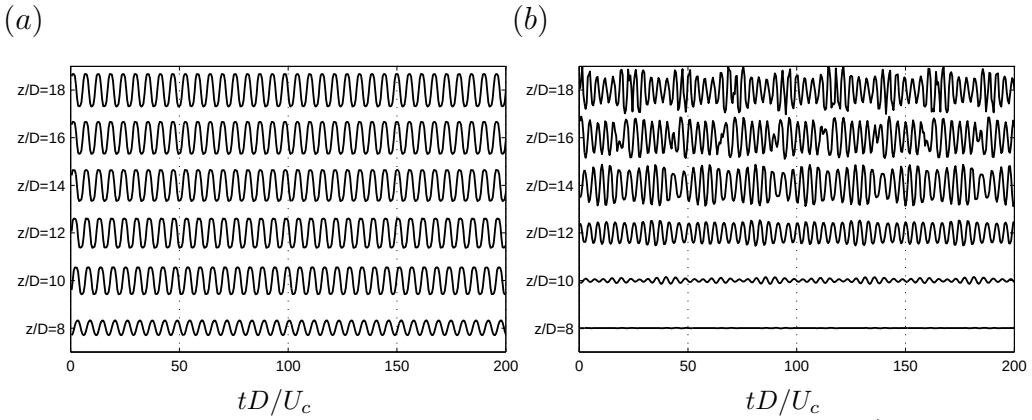

Figure 9: Time traces of cross-stream velocity v along a sampling line taken at $x/D = 18$ in the middle (x, z)-plane ($y/D = 5.5$). (a) Uniform inflow; (b) shear inflow.

vorticity with opposite sign can be identified, triggering the splitting of the main oblique vortices (Kármán vortices). This fragmentation was observed by Persillon & Braza[20] in their numerical simulations for a straight cylinder when they increased the Reynolds number beyond 190.

Further insight in the vortex shedding behaviour can be gained from the isosurfaces of instantaneous streamwise and vertical vorticity, which have been plotted in figure 11. The white isosurfaces correspond to the primary vortex cores represented by ω_z, while the black isosurfaces depict the streamwise vorticity ω_x. The shape of the primary vortex cores shown in figure 11(a) is similar to those expected for a straight circular cylinder (i.e. vertical). Furthermore, this particular geometry triggers streamwise vorticity in the lower part of the domain, affecting the vortex shedding pattern with respect to that of a straight circular cylinder. The streamwise vorticity for the shear flow case exhibits two distinct behaviours related to the presence of uniform shear at the inlet. Close to the top of the computational domain, where the highest local velocities of the free-stream occur, the presence of streamwise vorticity reveals the instabilities that lead to the splitting of the primary vortices discussed previously. Below this region, the isosurfaces of streamwise vorticity are strongly slanted and are clearly related to the oblique shedding of vortices. The cellular pattern of the vortex shedding and the obliqueness of the vortices behind a bluff body has been previously reported.[7–12] Most of these studies, however, consider a straight cylindrical geometry. Hence, further studies with different shear rates are relevant to better understand the interaction of the shear flow with this geometry. From figure 11(a), for instance, it was shown that streamwise vorticity arises as an effect of the curved geometry for the uniform flow case; the tilting of the vorticity induced by different shear rates may have either an adverse or favourable effect when interacting with the vorticity induced by geometry effects.

Finally, in order to study the evolution of the wake for the shear flow case, the instantaneous streamwise vorticities ω_x and ω_z were plotted in three consecutive planes in figure

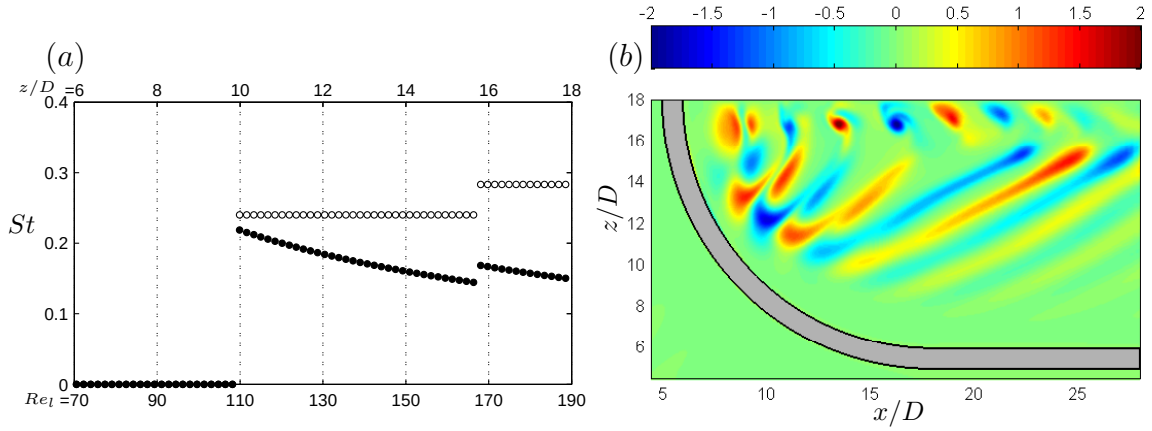

Figure 10: (a) Strouhal frequencies along a sampling line taken at $x/D = 18$ in the middle (x, z)-plane ($y/D = 5.5$). Shear flow case, •, St based in the local inflow velocity $U_\infty(z)$; ∘, St based in U_c. (b) Isocontours of instantaneous streamwise vorticity ω_x in the middle (x, z)-plane ($y/D = 5.5$).

12. The instantaneous streamwise vorticities in the (y, z)-planes shown in figure 12(a) give a clear picture of the evolution of ω_x in the x-direction. The plane at $x/D = 7$ is located within the recirculation region in the upper portion of the cylinder, here we observe two parallel layers of ω_x with opposite sign corresponding to the bended vortex filaments of ω_y induced by the shear rate.[8] The plane at $x/D = 12$ exhibits a similar pattern at the lower part of the curved cylinder, but the layers of ω_x here have different sign than those at $x/D = 7$; on the upper half of this plane negative values of ω_x prevail. At $x/D = 18$ the streamwise vorticity is split into several regions of counter rotating vorticity. In a similar way, figure 12(b) depicts the pattern for the vertical vorticity ω_z on three consecutive (x, y)-planes. Since the vortex shedding starts above $z/D = 10$, only two regions of ω_z appear at $z/D = 8$, here the flow could be regarded as locally stationary. At $z/D = 12.5$, where the local Reynolds number is 135, a clear pattern of vortex shedding is represented by the isocontours of ω_z. Close to the top of the domain at $z/D = 17.5$ the pattern of ω_z is more irregular than that at $z/D = 12.5$, the ω_z-cores are spread, covering a larger area at this vertical location; here $Re_l = 185$, i.e. within the range at which the mode A instability occurs,[19] thus the wake instabilities will be amplified as they are transported downstream.

4 CONCLUSIONS

In this work, DNS of the flow past a curved circular cylinder at $Re = 100$ is performed to study the influence of the curvature and different inflow conditions on the wake dynamics. In order to compare our results with the study by Miliou *et al.*,[6] a uniform inflow profile was considered as inflow boundary condition in an initial stage. Subsequently, the inflow

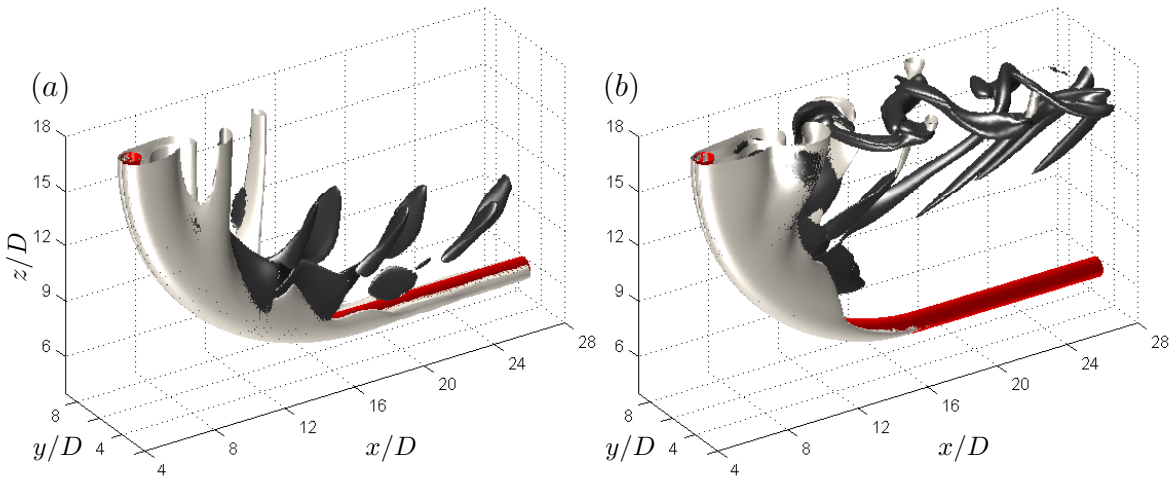

Figure 11: Detail of isosurfaces of instantaneous vorticity ω_x (black) and ω_z (white). (a) Uniform flow, isosurfaces of $\omega_x = \pm 0.3$ and $\omega_z = \pm 1.2$; (b) shear flow, isosurfaces of $\omega_x = \pm 0.7$ and $\omega_z = \pm 1.6$.

condition was changed to uniform shear with a shear rate of $K = 0.1$.

In general terms, good agreement was obtained between the present work and the results reported by Miliou *et al.*[6] for the uniform flow case. As a qualitative comparison, the vortical structures depicted in figure 8 exhibited the same shape as those reported in the mentioned study. Initially the vortex cores are vertical, then, as they travel further downstream, small distortions appear in the λ_2-isosurfaces. Additionally, the Strouhal frequency obtained for the uniform case ($fD/U_c = 0.176$) was the same as that reported by Miliou *et al.*[6]

Concerning the recirculation region, the base pressure gradient for the uniform flow case was adverse along the whole span, while the shear flow case exhibited a region of weak favourable pressure gradient. This clearly affected the distribution of velocities in the recirculation zone and the size of the recirculation bubble, which was larger than the recirculation bubble for the uniform flow case along the whole span, despite the local minimum observed in figure 6(b). Further downstream in the wake, the time analysis for the shear flow case revealed two distinct cells of different shedding frequency with values $fD/U_c = 0.240$ and 0.283. The computed length of these cells was $5.63D$ and $2.37D$, with a dislocation occurring at $z = 15.7D$. Furthermore, it was estimated that the dislocations occurred periodically each five shedding cycles. The analysis of vortical flow structures based on the instantaneous λ_2- and vorticity-isosurfaces revealed streamwise vorticity induced by the geometry for the uniform flow case, and streamwise wake instabilities for the shear flow case. Additionally, the shear flow case was characterized by oblique vortex shedding as the wake evolved downstream.

The performance of the IBM method was very promising when performing the simulations using this curved cylinder geometry embedded in a Cartesian mesh. It is therefore

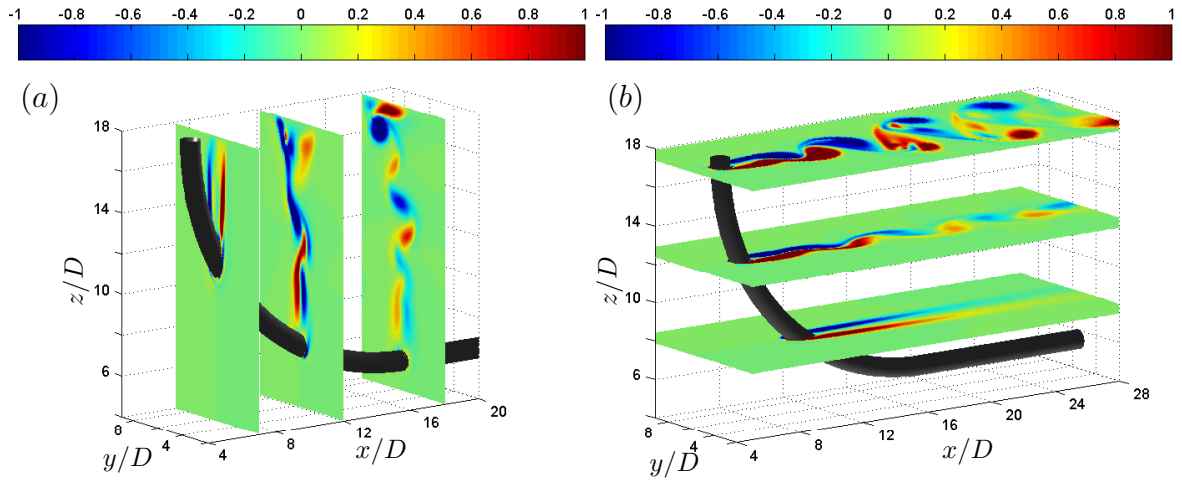

Figure 12: Instantaneous isocontours of vorticity for the shear flow case. (a) ω_x in the (y, z)-planes at $x/D = 7$, 12 and 18; (b) ω_z in the (x, y)-planes at $z/D = 8$, 12.5 and 17.5.

intended to extend this study to other shear rates and radii of curvature, contributing thus to the knowledge of the flow physics of the wake past such geometries.

ACKNOWLEDGMENTS

This study was partially supported by the Norwegian HPC project NOTUR that granted access to its computer facilities.

REFERENCES

[1] M. M. Zdravkovich, *Flow Around Circular Cylinders, Vol. 1 Fundamentals*, Oxford University Press, (1997).

[2] T. Leweke and M. Provansal, The flow behind rings: bluff body wakes without end effects, *J. Fluid Mech.*, **288**, 265–310 (1995).

[3] D. R. Monson, The effect of transverse curvature on the drag and vortex shedding of elongated bluff bodies at low Reynolds number, *J. Fluids Eng.*, **105**, 308–318 (1983).

[4] M. Takamoto and K. Izumi, Experimental observation of stable arrangement of vortex rings, *Phys. Fluids*, **24**, 1582–1583 (1981).

[5] A. Miliou, S. J. Sherwin and J. M. R. Graham, Fluid dynamic loading on curved riser pipes, *J. Offshore Mech. Arct.*, **125**, 176–182 (2003).

[6] A. Miliou, A. De Vecchi, S. J. Sherwin and J. M. R. Graham, Wake dynamics of external flow past a curved circular cylinder with the free stream aligned with the plane of curvature, *J. Fluid Mech.*, **592**, 89–115 (2007).

[7] W. A. Mair and P. K. Stansby, Vortex wakes of bluff cylinders in shear flow, *SIAM J. Appl. Math.*, **28**, 519–540 (1975).

[8] C. H. G. Woo, J. E. Cermak and J. A. Peterka, Secondary flows and vortex formation around a circular cylinder in constant-shear flow, *J. Fluid Mech.*, **204**, 523–542 (1989).

[9] D. Sumner and O. O. Akosile, On uniform planar shear flow around a circular cylinder at subcritical Reynolds number, *J. Fluids Struct.*, **18**, 441–454 (2003).

[10] M. Kappler, W. Rodi, S. Szepessy and O. Badran, Experiments on the flow past long circular cylinders in a shear flow, *Exp. Fluids*, **38**, 269–284 (2005).

[11] A. Mukhopadhyay, P. Venugopal and S. P. Vanka, Oblique vortex shedding from a circular cylinder in linear shear flow, *Comput. Fluids*, **31**, 1–24 (2002).

[12] J. H. Silvestrini and E. Lamballais, Direct numerical simulation of oblique vortex shedding from a cylinder in shear flow, *Int. J. Heat Fluid Flow*, **25**, 461–470 (2004).

[13] M. Manhart, F. Tremblay and R. Friedrich, MGLET: A parallel code for efficient DNS and LES of complex geometries, In *Parallel Computational Fluid Dynamics 2000*, Elsevier Science B.V., 449–456, (2001).

[14] M. Manhart , A zonal grid algorithm for DNS of turbulent boundary layers, *Comput. Fluids*, **33**, 435–461 (2004).

[15] J. H. Ferziger and M. Perić, Computational Methods for Fluid Dynamics, 3th Edition, *Springer: Berlin*, (2002).

[16] R. Mittal and G. Iaccarino, Immersed boundary methods, *Annu. Rev. Fluid Mech.*, **37**, 239–261 (2005).

[17] N. Peller, A. Le Duc, F. Tremblay and M. Manhart, High-order stable interpolations for immersed boundary methods, *Int. J. Numer. Meth. Fluids*, **52**, 1175–1193 (2006).

[18] J. Jeong and F. Hussain, On the identification of a vortex, *J. Fluid Mech.*, **285**, 69–94 (1995).

[19] C. H. K. Williamson, The existence of two stages in the transition to three-dimensionality of a cylinder wake, *Phys. Fluids*, **31**, 3165–3168 (1988).

[20] H. Persillon and M. Braza, Physical analysis of the transition to turbulence in the wake of a circular cylinder by three-dimensional Navier Stokes simulation, *J. Fluid Mech.*, **365**, 23–88 (1998).

Appendix C

Visualizations

Since the presentation of the results obtained from the numerical simulations imply to choose either a position in space to study time evolution, or a specific position in time to study instantaneous quantities, part of the information is somehow lost in this process. A visualization allows in some cases for a better understanding of some flow features, and it gives additionally an general idea of how the flow behaves. The following animations are included in the CD attached to this thesis.

1. $Re = 100$ with uniform flow in folder `/Re100/Re100Uniform/`.

   1.1 Animation of v-velocity in the (x, z)-plane; folder `/2D/`, file `xzV_Re100U`.

   1.2 Animation of the iso-surfaces of ω_x and ω_z (3D) in perspective view, and projections in the (x, y)- and (x, z)-planes; folder `/3D/`, files `isoOMXOMZ`, `xyOMXOMZ` and `xzOMXOMZ`.

   1.3 Animation of the square-root of enstrophy $|\boldsymbol{\omega}| = (\omega_x^2 + \omega_y^2 + \omega_z^2)^{1/2}$ (in 3D), in perspective view, and projections in the (x, y)- and (x, z)-planes; folder `/3D/`, files `iso_ens`, `xy_ens` and `xz_ens`.

2. $Re = 100$ with shear flow in folder `/Re100/Re100Shear/`.

   2.1 Animation of v-velocity in the (x, z)-plane; folder `/2D/`, file `xzV_Re100S`.

   2.2 Animation of the iso-surfaces of ω_x and ω_z (3D) in perspective view, and projections in the (x, y)- and (x, z)-planes; folder `/3D/`, files `isoOMXOMZ`, `xyOMXOMZ` and `xzOMXOMZ`.

2.3 Animation of the square-root of enstrophy $|\boldsymbol{\omega}| = (\omega_x^2 + \omega_y^2 + \omega_z^2)^{1/2}$ (in 3D); in perspective view, and projections in the (x, y)- and (x, z)-planes; folder `/3D/`, files `iso_ens`, `xy_ens` and `xz_ens`.

3. Re=500 with uniform flow in folder `/Re500/Re500Uniform/`.

   3.1 Animation of v-velocity in the (x, z)-plane; folder `/2D/`, file `xzV_Re500U`.

4. Re=500 with shear flow in folder `/Re500/Re500Shear/`.

   4.1 Animation of v-velocity in the (x, z)-plane; folder `/2D/`, file `xzV_Re500S`.

Bibliography

D. Barkley and R. D. Henderson. Three-dimensional Floquet stability analysis of the wake of a circular cylinder. *Journal of Fluid Mechanics*, 322:215, 1996. ISSN 0022-1120. doi: 10.1017/S0022112096002777. URL http://www.journals.cambridge.org/abstract_S0022112096002777.

M. V. Begak, S. I. Devnin, and L. G. Zavadovskaya. Investigation of vortex shedding from yawed and curved circular cylinders. *Fluid dynamics*, 20(5):314–315, 1985.

M. S. Bloor. The transition to turbulence in the wake of a circular cylinder. *Journal of Fluid Mechanics*, 19(02):290–304, 1968. ISSN 0022-1120. doi: 10.1017/S0022112064000726. URL http://www.journals.cambridge.org/abstract_S0022112064000726.

M. Coutanceau and R. Bouard. Experimental determination of the main features of the viscous flow in the wake of a circular cylinder in uniform translation. Part 1. Steady flow. *Journal of Fluid Mechanics*, 79(02):231–256, 2006. ISSN 0022-1120. doi: 10.1017/S0022112077000135. URL http://www.journals.cambridge.org/abstract_S0022112077000135.

A. De Vecchi, S. J. Sherwin, and J. M. R. Graham. Wake dynamics of external flow past a curved circular cylinder with the free-stream aligned to the plane of curvature. *Journal of Fluids and Structures*, 24:1262–1270, 2008. doi: 10.1016/j.jfluidstructs.2008.06.008.

A. De Vecchi, S. J. Sherwin, and J. M. R. Graham. Wake dynamics past a curved body of circular cross-section under forced cross-flow vibration. *Journal of Fluids and Structures*, 25(4):721–730, 2009. ISSN 08899746. doi: 10.1016/j.jfluidstructs.2009.01.005. URL http://linkinghub.elsevier.com/retrieve/pii/S0889974609000127.

J. H. Ferziger and M. Perîc. *Computational Methods for Fluid Dynamics*. Springer-Verlag Berlin Heidelberg New York, 2002. ISBN 3-540-42074-6.

A. R. Hanson. Vortex Shedding from Yawed Cylinders. *AIAA Journal*, 4(4):738–740, 1966.

R. D. Henderson. Details of the drag curve near the onset of vortex shedding. *Physics of Fluids*, 7(9):2102, 1995. ISSN 10706631. doi: 10.1063/1.868459. URL http://link.aip.org/link/PHFLE6/v7/i9/p2102/s1&Agg=doi.

J. Jeong and F. Hussain. On the identification of a vortex. *Journal of Fluid Mechanics*, 285:69–94, 1995.

M. Kappler, W. Rodi, S. Szepessy, and O. Badran. Experiments on the flow past long circular cylinders in a shear flow. *Experiments in Fluids*, 38(3):269–284, 2005. ISSN 0723-4864. doi: 10.1007/s00348-004-0872-5. URL http://www.springerlink.com/content/lybwjnhquramwjyw.

G. E. Karniadakis and G. S. Triantafyllou. Three-dimensional dynamics and trantision to turbulence in the wake of bluff objects. *Journal of Fluid Mechanics*, 238:1–30, 1992. ISSN 0022-1120.

D. Lucor and G. E. Karniadakis. Effects of Oblique Inflow in Vortex-Induced Vibrations. *Flow, Turbulence and Combustion (formerly Applied Scientific Research)*, 71(1-4):375–389, 2003. ISSN 1386-6184. doi: 10.1023/B:APPL.0000014929.90891.4d. URL http://www.springerlink.com/openurl.asp?id=doi:10.1023/B:APPL.0000014929.90891.4d.

W. A. Mair and P. K. Stansby. Vortex wakes of bluff cylinders in shear flow. *SIAM Journal of Applied Mathematics*, 28:519–540, 1975.

M. Manhart. A zonal grid algorithm for DNS of turbulent boundary layers. *Computer & Fluids*, 33:435–461, 2004.

M. Manhart, F. Tremblay, and R. Friedrich. *MGLET: A parallel code for efficient DNS and LES of complex geometries*. North-Holland, Amsterdam, 2001.

D. J. Maull and R. A. Young. Vortex shedding from bluff bodies in a shear flow. *Journal of Fluid Mechanics*, 60(02):401–409, 1973. ISSN 0022-1120. doi: 10.

1017/S0022112073000236. URL http://www.journals.cambridge.org/abstract_S0022112073000236.

A. Miliou, S. J. Sherwin, and J. M. R. Graham. Wake topology of curved cylinders at low Reynolds numbers. *Flow Turbulence and Combustion*, 71(1-4):147–160, 2003a. ISSN 1386-6184.

A. Miliou, S. J. Sherwin, and J. M. R. Graham. Fluid Dynamic Loading on Curved Riser Pipes. *Journal of Offshore Mechanics and Arctic Engineering*, 125(3):176, 2003b. ISSN 08927219. doi: 10.1115/1.1576817. URL http://link.aip.org/link/JMOEEX/v125/i3/p176/s1&Agg=doi.

A. Miliou, I. Mortazavi, and S. J. Sherwin. Cut-off analysis of coherent vortical structure identification in a three-dimensional external flow. *Comptes Rendus Mécanique*, 333 (3):211–217, 2005. ISSN 16310721. doi: 10.1016/j.crme.2004.09.022. URL http://linkinghub.elsevier.com/retrieve/pii/S1631072104002670.

A. Miliou, A. De Vecchi, S. J. Sherwin, and J. M. R. Graham. Wake dynamics of external flow past a curved circular cylinder with the free stream aligned with the plane of curvature. *Journal of Fluid Mechanics*, 592:89–115, 2007. doi: 10.1017/S0022112007008245.

G. D. Miller and C. H. K. Williamson. Control of three-dimensional phase dynamics in a cylinder wake. *Experiments in Fluids*, 18:26–35, 1994. ISSN 0723-4864. doi: 10.1007/BF00209358. URL http://www.springerlink.com/index/10.1007/BF00209358.

R. Mittal and G. Iaccarino. Immersed Boundary Methods. *Annual Review of Fluid Mechanics*, 37(1):239–261, 2005. ISSN 0066-4189. doi: 10.1146/annurev.fluid.37.061903.175743.

A. Mukhopadhyay, S. P. Vanka, and P. Venugopal. Numerical Study of Vortex Shedding From a Circular Cylinder in Linear Shear Flow. *Journal of Fluids Engineering*, 121 (June):460–468, 1999.

A. Mukhopadhyay, P. Venugopal, and S. P. Vanka. Oblique vortex shedding from a circular cylinder in linear shear flow. *Computers & Fluids*, 31:1–24, 2002.

C. Norberg. An experimental investigation of the flow around a circular cylinder: influence of aspect ratio. *Journal of Fluid Mechanics*, 258:287–316, 1994. ISSN 0022-1120. doi: 10.1017/S0022112094003332. URL http://www.journals.cambridge.org/abstract_S0022112094003332.

N. Peller, A. Le Duc, F. Tremblay, and M. Manhart. High-order stable interpolations for immersed boundary methods. *International Journal for Numerical Methods in Fluids*, 52:1175–1193, 2006.

H. Persillon and M. Braza. Physical analysis of the transition to turbulence in the wake of a circular cylinder by three-dimensional Navier-Stokes simulation. *Journal of Fluid Mechanics*, 365:23–88, 1998. ISSN 00221120. doi: 10.1017/S0022112098001116. URL http://www.journals.cambridge.org/abstract_S0022112098001116.

M. Provansal, C. Mathis, and L. Boyer. Bénard-von Kármán instability: transient and forced regimes. *Journal of Fluid Mechanics*, 182:1–22, 1987. ISSN 0022-1120. doi: 10.1017/S0022112087002222. URL http://www.journals.cambridge.org/abstract_S0022112087002222.

S. E. Ramberg. The effects of yaw and finite length upon the vortex wakes of stationary and vibrating circular cylinders. *Journal of Fluid Mechanics*, 128:81–107, 1983.

A. Roshko. Perspectives on bluff body aerodynamics. *Journal of Wind Engineering and Industrial Aerodynamics*, 49:79–100, 1993.

J. H. Silvestrini and E. Lamballais. Direct numerical simulation of oblique vortex shedding from a cylinder in shear flow. *International Journal of Heat and Fluid Flow*, 25: 461–470, 2004.

D. Sumner and O. O. Akosile. On uniform planar shear flow around a circular cylinder at subcritical Reynolds number. *Journal of Fluids and Structures*, 18:441–454, 2003. ISSN 08899746. doi: 10.1016/j.jfluidstructs.2003.08.004. URL http://linkinghub.elsevier.com/retrieve/pii/S0889974603001117.

C. W. Van Atta. Experiments on vortex shedding from yawed circular cylinders. *AIAA Journal*, 6(5):931–933, 1968. ISSN 0001-1452. doi: 10.2514/3.4630. URL http://doi.aiaa.org/10.2514/3.4630.

F. M. White. *Viscous fluid flow*. McGraw-Hill New York, 2006. ISBN 0070697108 0850521661.

C. H. K. Williamson. The existence of two stages in the transition to three-dimensionality of a cylinder wake. *Physics of Fluids*, 31(11):3165–3168, 1988. URL http://link.aip.org/link/?PFL/31/3165/1.

C. H. K. Williamson. The natural and forced formation of spot-like vortex dislocations in the transition of a wake. *Journal of Fluid Mechanics*, 243:393–441, 1992.

C. H. K. Williamson. Three-dimensional wake transition. *Journal of Fluid Mechanics*, 328(-1):345–407, 1996a. ISSN 0022-1120. doi: 10.1017/S0022112096008750. URL http://www.journals.cambridge.org/abstract_S0022112096008750.

C. H. K. Williamson. Vortex dynamics in the cylinder wake. *Annual Review of Fluid Mechanics*, 28:477–539, 1996b. URL www.annualreviews.org/aronline.

C. H. K.; Brown G. L. Williamson. A Series in $1/\sqrt{Re}$ to Represent the Strouhal–Reynolds Number Relationship of the Cylinder Wake. *Journal of Fluids and Structures*, 12(8):1073–1085, 1998. ISSN 08899746. doi: 10.1006/jfls.1998.0184. URL http://linkinghub.elsevier.com/retrieve/pii/S0889974698901840.

J. H. Williamson. Low-Storage Runge-Kutta Schemes. *Journal of Computational Physics*, 56:48–56, 1980.

C. H. G. Woo, J. E. Cermak, and J. A. Peterka. Secondary flows and vortex formation around a circular cylinder in constant-shear flow. *Journal of Fluid Mechanics*, 204: 523–542, 1989. ISSN 0022-1120.

M. M. Zdravkovich. *Flow Around Circular Cylinders, Vol. 1 Fundamentals*. Oxford University Press, 1997.

M. M. Zdravkovich. *Flow Around Circular Cylinders, Vol. 2 Applications*. Oxford University Press, 2003.

M. Zhao, L. Cheng, and T. Zhou. Direct numerical simulation of three-dimensional flow past a yawed circular cylinder of infinite length. *Journal of Fluids and Structures*, 25(5):831–847, 2009. ISSN 08899746. doi: 10.1016/j.jfluidstructs.2009.02.004. URL http://linkinghub.elsevier.com/retrieve/pii/S0889974609000218.

T. Zhou, H. Wang, S. F. M. Razali, Y. Zhou, and L. Cheng. Three-dimensional vorticity measurements in the wake of a yawed circular cylinder. *Physics of Fluids*, 22(1): 015108, 2010. ISSN 10706631. doi: 10.1063/1.3291072. URL http://link.aip.org/link/PHFLE6/v22/i1/p015108/s1&Agg=doi.